SEISMIC FRAGILITY ESTIMATES FOR CORRODED REINFORCED CONCRETE BRIDGE STRUCTURES WITH TWO-COLUMN BENTS

A Dissertation

by

JINQUAN ZHONG

Submitted to the Office of Graduate Studies of
Texas A&M University
in partial fulfillment of the requirements for the degree of

DOCTOR OF PHILOSOPHY

December 2008

Major Subject: Civil Engineering

SEISMIC FRAGILITY ESTIMATES FOR CORRODED REINFORCED CONCRETE BRIDGE STRUCTURES WITH TWO-COLUMN BENTS

A Dissertation

by

JINQUAN ZHONG

Submitted to the Office of Graduate Studies of
Texas A&M University
in partial fulfillment of the requirements for the degree of

DOCTOR OF PHILOSOPHY

Approved by:

Co-Chairs of Committee,	Paolo Gardoni
	David V. Rosowsky
Committee Members,	Benchun Duan
	Jose M. Roesset
Head of Department,	David V. Rosowsky

December 2008

Major Subject: Civil Engineering

ABSTRACT

Seismic Fragility Estimates for Corroded Reinforced Concrete Bridge Structures with Two-column Bents. (December 2008)

Jinquan Zhong, B.E.; M.S., Tongji University;

M.C.E., University of Delaware

Co-Chairs of Advisory Committee: Dr. Paolo Gardoni
Dr. David Rosowsky

To assess the losses associated with future earthquakes, seismic vulnerability functions are commonly used to correlate the damage or loss of a structure to the level of seismic intensity. A common procedure in seismic vulnerability assessment is to estimate the seismic fragility, which is defined as the conditional probability that a structure fails to meet the specific performance level for given level of seismic intensity.

This dissertation proposes a methodology to estimate the fragility of corroded reinforced concrete (RC) bridges with two-column bents subject to seismic excitation. Seismic fragility functions are first developed for the RC bridges with two-column bents. All available information from science/engineering laws, numerical analysis, laboratory experiments, and field measurements has been used to construct the proper form of the fragility functions. The fragility functions are formulated, at the individual column, bent, and bridge levels, in terms of the spectral acceleration and the ratio between the peak ground velocity and the peak ground acceleration. The developed fragility functions properly account for the prevailing uncertainties in fragility estimation. The

probabilistic capacity and demand models are then combined with the probabilistic models for chloride-induced corrosion and the time-dependent corrosion rate. The fragility estimates for corroded RC bridges incorporates the uncertainties in the parameters of capacity and demand models, and the inexactness (or model error) in modeling the material deterioration, structural capacity, and seismic demands. The proposed methodology is illustrated by developing the fragility functions for an example RC bridge with 11 two-column bents representing current construction in California.

The developed fragility functions provide valuable information to allocate and spend available funds for the design, maintenance, and retrofitting of structures and networks. This study regarding the vulnerability of corroding RC bridges will be of direct value to those making decisions about the condition assessment, residual life, and the ability of lifeline structures to withstand future seismic demands.

DEDICATION

To my family and my girlfriend

ACKNOWLEDGEMENTS

I would like to thank the co-chairs of my advisory committee, Dr. Paolo Gardoni and Dr. David Rosowsky. It was their patience, guidance, and support that made possible this study all the way through from ground zero to completion over the past three years. It has been my great honor to work with them on the front line of structural reliability. Learning this profession has been a long process. However, it turns out to be a great gift for me and will be beneficial to my future.

Great gratitude is given to my committee members, Dr. Jose Roesset and Dr. Benchun Duan, for their inspiration and guidance throughout the course of this research. Special appreciation is also expressed to Dr. Joseph Bracci at the Department of Civil Engineering. It was his encouragement that made my experience at Texas A&M a unique one.

My gratitude also goes to my friends who have helped the growth of my Aggie Spirit, and to the colleagues and the department faculty and staff for making my study at Texas A&M a great one. I also want to extend my gratitude to the National Highway Institute, which provided the partial financial support through a fellowship under Award No. DDEGRD-06-X-00457. Opinions and findings presented are those of the researcher and do not necessary reflect the views of the National Highway Institute.

Finally, thanks to my mother and father for giving me this wonderful life along with their encouragement.

TABLE OF CONTENTS

CHAPTER Page

LIST OF FIGURES

FIGURE Page

FIGURE Page

LIST OF TABLES

CHAPTER I

INTRODUCTION

BACKGROUND

Earthquakes experienced in California, Japan, Mexico, and Central and South America over the last 20 years have caused the failure of a substantial number of bridges, which either collapsed or suffered severe damage and had to be closed to traffic. Many of these bridges had been designed before the seismic requirements of the codes were upgraded in the 1980's. The dramatic collapse of the Hanshin Expressway Route 43 in three locations between Kobe and Nishinomiya, Japan in January 1995 had been one of the most graphic images for seismic damage. Ten spans of the Hanshin Expressway were knocked over, resulting in the interruption for 20 months of a link that carried forty percent of the Osaka-Kobe road traffic.

Damage to bridges during earthquakes, or their complete collapse, not only can cause loss of lives, but also represents a serious disruption to emergency operations, and can entail substantial economic losses due to the interruption of transportation services. For these reasons, the assessment of the seismic vulnerability of existing bridges, and of the bridges under design, has become a subject of considerable interest and research.

This dissertation follows the style of *Journal of Engineering Mechanics*, ASCE.

To assess the losses associated with future earthquakes, seismic vulnerability functions are commonly used to correlate the damage or loss of a structure to the level of seismic intensity (Chen and Sawthorn 2003). Several methodologies have been developed to assess the seismic vulnerability of structures. The common procedure in seismic vulnerability assessment is to develop fragility functions. Seismic fragility is defined as the conditional probability that a structure fails to meet a specific performance level for given level of seismic demands. One of the challenges in developing seismic fragility functions is to express the specific performance level in terms of structural capacities and responses that engineers can evaluate with the available tools (Rosowsky 2007). Developing seismic fragility functions also provides valuable information for allocating and spending available funds for the design, maintenance and retrofitting of bridge structures and networks. Three approaches have been broadly applied to develop the seismic fragility functions: the empirical, analytical, and Bayesian approaches, which will be described briefly later.

In bridge structures, reinforced concrete (RC) columns are designed as load paths transferring the inertia force from the superstructure to the foundation. They are usually designed to deform well beyond their elastic limits prior to the superstructure or the bent cap reaching its expected nominal strength (Caltrans 2006). The RC bents in bridge structures can be categorized into two configurations: single-column and multi-column bents. While the first configuration can shorten the construction time and reduce the land use for the bridge substructures, the second one is preferred over the former one. This is mainly because a multiple-column configuration has a redundant load path and

has often the advantage of reducing the cost of the substructure (Sritheran et al. 2001). For instance, the redundancy and clearance that a two-column configuration can provide, for instance, for urban interchanges are the main reasons to prefer two-column bents over single-column bents. However, most of previous studies on seismic fragility for bridges have been focusing on single-column bents (e.g., Karim and Yamazaki 2001, 2003, 2007; Gardoni et al. 2002, 2003; Monti and Nistico 2002; Kim and Feng 2003; Kim and Shinozuka 2003; Lu et al. 2005; Oller and Barbat 2006; Lupoi et al. 2006; Choi et al. 2006; Banerjee and Shinozuka 2007; Jeong and Elnashai 2007). Limited effort (e.g., Shinozuka et al. 2000; Kunnath 2007) has been made to develop the fragility functions for RC bridge structures with multicolumn bents.

Furthermore, most bridges have been subjected to corrosion at the time of occurrence of a seismic event. Due to the onset of corrosion, the capacity reduction in RC columns has raised a major concern in the vulnerability of corroded RC bridges. Therefore, there is also a need to account for the deterioration of the column capacities and the changes in the seismic demands when assessing the fragility of a bridge during its service life.

RESEARCH OBJECTIVES

The current study focuses on the RC bridges with two-column bents. The dissertation includes the following three objectives:

Objective 1: Develop probabilistic models to predict the deformation and shear demands on RC bridges with two-column bents subject to seismic excitation. All available information from science/engineering laws, numerical analysis, laboratory

experiments, and field measurements should be used to construct the proper forms of the probabilistic demand models and to assess them accounting for the prevailing uncertainties.

Objective 2: Propose a simplified formulation to estimate the seismic fragility of RC bridges with two-column bents. A simplified fragility formulation is to develop not to rely on complex reliability analysis and reliability software and still capture the dominant uncertainty in seismic fragility estimation.

Objective 3: Obtain the seismic fragility estimates for corroded RC bridges with two-column bents. The objective is to consider the effects of corrosion-induced deterioration on the bridge component stiffness and (deformation and shear) capacities and on the seismic demands during a bridge service life.

STRUCTURE OF THE DISSERTATION

This dissertation includes six chapters. Chapter II introduces the development of the probabilistic seismic models to predict the deformation and shear demands in RC bridges with two-column bents. Chapter III proposes a simplified formulation to estimate the fragility of RC bridge structures with two-column bents. To model the physical process from corrosion initiation to the cracking of concrete cover, Chapter IV proposes a new model for the time to cracking of concrete cover and the corresponding stiffness degradation in cover concrete caused by corrosion-induced cracking using the energy principle. Chapter V incorporates the effects of corrosion on the fragility estimation for RC bridges with two-column bents. Finally, the conclusions, limitations, and the suggestions for future research are included in Chapter VI.

CHAPTER II

PROBABILISTIC SEISMIC DEMAND MODELS FOR DEFORMATION AND SHEAR IN RC BRIDGES WITH TWO-COLUMN BENTS*

The dominating uncertainties in estimating seismic fragility for bridges come from the structural capacity and demands due to the seismic excitation. This chapter introduces the development of the probabilistic models for deformation and shear demands on RC bridges with two-column bents. Experimental data from laboratory and numerical simulations are used in the model development. Seismic fragility is then formulated in terms of the developed probabilistic demand models and the probabilistic capacity models previously developed. As the application, seismic fragility are estimated on the column, bent and bridge levels for an example RC bridge with 11 two-column bents.

INTRODUCTION

Bridges with multiple two-column RC bents are commonly built in California and other seismic regions. Consequently, ensuring the seismic performance of two-column RC bents is vital for bridge safety. Although some small-scale tests of two-column RC bents have been conducted (Moore 2000; Nada 2003; Moustafa 2004), a complete study of the

*Part of this Chapter is reprinted with permission from "Probabilistic Seismic Demand Models and Fragility Estimates for Reinforced Concrete Bridges with Two-Column Bents." by Jinquan Zhong, Paolo Gardoni, David Rosowsky, and Terje Haukaas, 2008, *Journal of Engineering Mechanics*, ASCE, 134(6), 495-504, Copyright [2008] by the American Society of Civil Engineers.

seismic demands on two-column RC bents is still missing. Furthermore, since RC bents are integrated into bridge systems along with other bridge elements, there is a lack of knowledge on the reliability of entire bridge systems with two-column RC bents subject to seismic excitation. This shortcoming is bolstered by the fact that entire bridge systems cannot be tested in the laboratory.

Gardoni et al. (2003) developed a Bayesian methodology to construct probabilistic seismic demand models for the components of a structural system subject to seismic excitation. The approach used a combination of deterministic demand models and observed data. While the formulation was general, Gardoni et al. (2003) presented demand models and fragility estimates for RC bridges with single-column bents only. Fragility is herein defined as the conditional probability of attaining or exceeding a specified damage state for a given set of demand variables.

This chapter presents the development of probabilistic models for RC bridges with two-column RC bents (Zhong et al. 2008a,b). Probabilistic models for deformation and shear demands of two-column RC bents are developed using a Bayesian approach. The probabilistic models are constructed based on deterministic demand models and procedures commonly used in practice. Correction terms are added to the deterministic models to explicitly describe the inherent systematic and random errors. Terms that contribute to correct the bias in the existing demand models are identified by means of a set of "explanatory" functions. A step-wise deletion process is used to construct parsimonoius models by identifying which explanatory functions, from a set of candidate functions, are more informative and which ones can be removed from the

model without significant loss of information and accuracy. These explanatory functions provide insight into the underlying behavioral phenomena and can be used to identify ground motion parameters that are most relevant to the seismic demands. The probabilistic models are constructed using data from laboratory experiments on two-column RC bents under the ground motions with ramped peak ground acceleration (PGA), and simulated dynamic responses (virtual data). The selection of initial (candidate) explanatory functions for the demand models is based on engineering understanding of the structural response of bridges subject to seismic excitation.

In this chapter, fragility estimates are developed for an example RC bridge with 11 two-column bents, designed according to the current specifications for California; Caltrans' Bridge Design Specification and Seismic Design Criteria (Caltrans 1999). Fragility estimates are computed at the individual column, bent, and bridge system levels, as a function of the spectral acceleration (S_a) and the ratio between the peak ground velocity (PGV) and PGA, PGV/PGA.

This chapter has five sections. Following this introduction, we describe the development of unbiased probabilistic demand models. Next, the development of fragility estimates for bridge components (columns), sub-systems (bents), and the complete system (bridge) is outlined. Finally, we provide a practical demonstration of the proposed methodology by estimating the component, sub-system, and system fragilities for an example bridge and the summary.

DEVELOPMENT OF PROBABILISTIC DEMAND MODELS

Deformation capacity and shear strength are common concerns in seismic design of bridges. The lateral deformed shape of a bridge is mainly determined by the plastic deformation in the columns. This is because in seismic zones the cap beam and superstructure usually are designed to remain in the elastic range while the columns are allowed to exhibit inelastic response to dissipate the seismic energy (Caltrans 2006).

In this section, we first review the deterministic models that are currently available to estimate deformation and shear demands. Then, we discuss the data sets used to develop the probabilistic demand models. Finally, we develop probabilistic models for deformation and shear demands.

Deterministic demand models

An ideal deterministic model for predicting the seismic demands on the components of a structural system should be simple, avoiding cumbersome nonlinear time history analyses, and accurate, accounting for the interaction between the components that constitute the structural system.

In this chapter, we develop unbiased probabilistic models starting from deterministic demand models and procedures commonly used in practice. In particular, we consider the method proposed by Chopra and Goel (1999). The method is an improvement of the capacity-demand diagram method presented in ATC-40 (ATC 1996) and FEMA-274 (FEMA 1997), which uses the well-known constant-ductility spectrum for the demand diagram.

In the utilized method, a nonlinear pushover analysis for the structure is first conducted. The distribution of the lateral forces for the pushover follows the assumed deformed shape, weighted by the tributary masses. Then, an equivalent single-degree-of-freedom (SDF) system is derived from the bilinear approximation of the pushover curve. The seismic deformation demand imposed on the equivalent SDF system is estimated by response spectrum analysis using inelastic spectra. Finally, the local seismic demands are determined by pushing the original structure to the maximum displacement determined for the equivalent SDF system. Since the original work by Chopra and Goel (1999) focuses on buildings, the pushover curve simply represents the base shear force versus the roof displacement.

Fajfar et al. (1997) developed a similar methodology (the N2 Method) for bridges (Fajfar and Fischinger 1987, 1988; Fajfar 2000). In the case of bridges, the properties of the equivalent SDF system are determined based on a characteristic force-displacement relation of the bridge system in the transverse direction. The force is the sum of all the lateral forces and the displacement is monitored at a "characteristic point" at the deck level, where the largest displacement is expected.

In this chapter, we follow the modification of Fajfar's approach proposed in Gardoni et al. (2003), where the force in the pushover is taken as the sum of all the transverse shear forces in the columns, excluding the forces taken by the abutments. Gardoni et al. (2003) showed that this approach provides more accurate estimates of the deformation and shear demands on the bridge columns.

Data used to construct the probabilistic demand models

Three data sets are used to develop the probabilistic demand models: (1) shake table experiments on two-column RC bents, (2) simulated dynamic responses (virtual data) for a two-column 11-bent RC-bent bridge modeled in OpenSees (http://opensees.berkeley.edu), and (3) shake table tests on a three-bent system.

The laboratory test results are for hinged RC bents with circular cross-section columns. Moustafa (2004) tested three two-column RC bents with bent heights 0.89 m, 1.6 m, and 2.36 m and column diameters 0.71 m. Nada (2003) tested three architecture-flared two-column RC bents, two with bent heights 1.63 m and one with bent height 0.99 m. The diameter of all columns was 0.61 m. Moore (2000) tested one two-column RC bent with height 2.36 m and column diameter 0.61 m. The ground motions used in the laboratory experiments were scaled versions of a record from the 1994 Northridge Earthquake. The PGA the scaled ground motions varied from 0.1 g to 3.25 g.

The laboratory data provide useful information to assess the unbiased probabilistic demand models. However, there are two limitations inherent in these data. First, they do not account for the overall bridge system behavior. Second, frequency similarity exists in scaled ground motions since they are all generated from the same earthquake. To overcome these limitations in the development of probabilistic models, we also consider virtual data obtained from nonlinear dynamic analysis performed on a modified model of an interior segment of the I-880 viaduct located in Oakland, CA. The structure, built in 1998, is the 5th and 6th St. Viaduct (CL Line and EU Ramp, Caltrans Bridge No. 33-0616L), and is a prestressed concrete, multi-span box-girder structure,

1138 m long, 21.8 m wide, and 2 m high. The interior segment of the I-880 viaduct, considered here, includes 11 two-column RC bents with a confined circular core for each column. Columns in Bents 1 to 8 have the same cross sections. Smaller cross sections are used for columns in Bents 9 to 11. The bent heights decrease from Bent 1 to Bent 11.

A finite element model of the I-880 viaduct segment was implemented in OpenSees by Kunnath (2007). Each bent is linked to the foundation with springs to account for the soil-structure interaction effect (Kunnath 2007). To account for the effect of abutments, the original model of the interior segment of the I-880 viaduct is modified by adding an extra span to each end that approaches the corresponding abutment added at the end of the viaduct. The abutments are modeled following current California specifications (Caltrans 2006). Fig. 1*a* shows the elevation view of the modified I-880 viaduct. Fig. 1*b* shows the details of two typical cross sections, Sections1-1 and 2-2, for the RC columns. The dimension of 2.59×2.43 m (8.5×8 ft) (for Section 1-1) was used for the columns in Bents 1 to 8, while the dimension of 2.29×2.03 m (7.51×6.67 ft) (for Section 2-2) was used for Bents 9 to 11. In the following chapters, we refer the example bridge structure as the modified I-880.

Ten site-specific ground motions are generated for three different hazard levels (50%, 10% and 2% probability in 50 years), thus yielding a total of 30 ground motions. The original unscaled ground motions are available at http://www.peertestbeds.net/i-880.htm. The method of scaling the ground motions is provided in Kunnath et al.

(2006). In these two data sets, S_a ranges between 0.090 g and 15.7 g, and PGV/PGA ranges between 0.036 sec. and 1.9 sec.

This dataset overcame the two limitations of the first dataset. However, it was obtained using numerical simulations and not actual experimental or field data. Therefore, it was affected by potential errors and inaccuracies in the finite element model, here called model error.

The third dataset compiles the results from shake table tests on a three-bent system conducted at the University of Nevada, Reno (Johnson, 2006). The bridge system consists of three bents, with two columns per bent, and a prestressed concrete superstructure with each span length of 9.14 m. The clear heights of the three bents are 1.83 m, 2.44 m, and1.52 m, with the tallest bent in the middle. The diameter of each column is 0.305 m. The prestressed concrete superstructure is composed of a solid slab 0.36 *m* thick with two-way prestressing. Abutments are not included in the system during the laboratory tests.

Eleven input motions in the transverse direction are generated based on the 1994 Northridge Earthquake recorded at the ground station Century City County Club North (Johnson, 2006). The PGA of the input motions varies from 0.075 to 1.66 g. The ratio PGV/PGA ranges from 0.445 to 0.764 sec. The effects on the seismic demands of the incoherency among the achieved motions at each bent location are accounted for by locating each bent on a separate shake table. In the laboratory tests, deformation responses on the top of each bent are measured using displacement transducers. This dataset, however, did not include the shear demands on each bent.

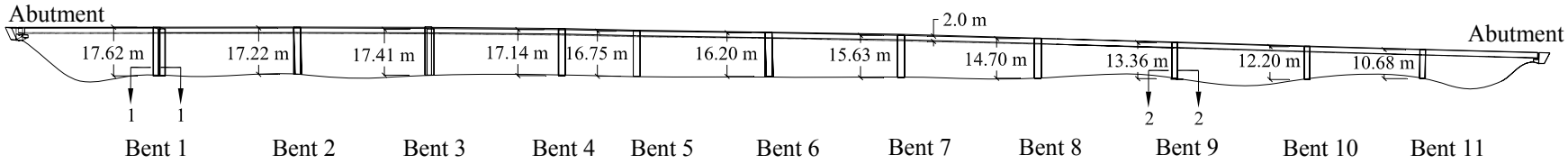

(*a*). Elevation view of the example bridge structure

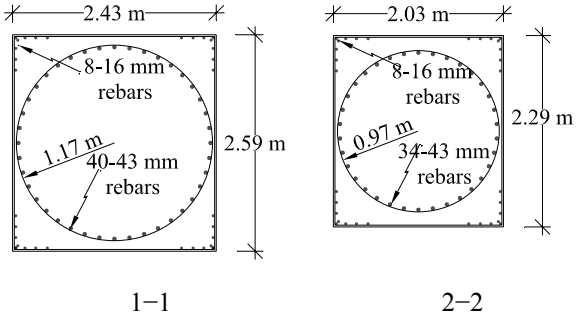

(*b*). Details for typical column cross-sections: Section 11 for columns in Bents 1 to 8; Section 22 for columns in Bents 9 to 11.

Fig. 1. Modified I-880 and typical column sections (*a*) Elevation view of modified I-880; (*b*). Details for typical column cross-sections

It is noted that the Bayesian methodology that is utilized requires no distinction between the experimental and virtual data. All the data are integrated in the Bayesian analysis described here to obtain the posterior statistics of unknown parameters in the models.

Probabilistic demand models

A generic form for the probabilistic demand models are developed according to the formulation proposed by Gardoni et al. (2002, 2003). Accordingly, the demand models for a structural system consisting of s components each with q demands are written as follows:

$$D_{ki}\left(\mathbf{x},\boldsymbol{\theta}_{Dk},\varepsilon_{Dki}\right)=\hat{d}_{ki}(\mathbf{x})+\gamma_{Dk}(\mathbf{x},\boldsymbol{\theta}_{Dk})+\sigma_{Dk}\varepsilon_{Dki},\quad i=1,..,s\quad k=1,..,q \tag{1}$$

where D_{ki} denotes the demand quantity of interest, $\mathbf{x}=(\mathbf{x}_1,\mathbf{x}_2,\cdots,\mathbf{x}_s)$ is a set of basic deterministic or random variables associated with the structure (e.g., material properties and geometry), $\boldsymbol{\theta}_{Dk}$ denotes the vector of unknown parameters associated with demand k, ε_{Dki} is a standard normal random variable, $\hat{d}_{ki}(\mathbf{x})$ denotes the deterministic prediction, $\gamma_{Dk}(\mathbf{x}_i,\boldsymbol{\theta}_{Dk})$ denotes the correction term for the bias in $\hat{d}_{ki}(\mathbf{x})$, σ_{Dk} represents the standard deviation of the model error, and. The covariance matrix of the random variables $\sigma_{Dk}\varepsilon_{Dki}$ is indicated as $\boldsymbol{\Sigma}_{Dk}$.

In formulating the model, Gardoni et al. (2003) employed a suitable transformation of the demand quantities to justify the following assumptions: (1) the

model variances σ_{Dk} are independent of $\mathbf{x} = (\mathbf{x}_1, \mathbf{x}_2, \cdots)$ (homoskedasticity assumption), and (2) ε_{Dki} is normally distributed (normality assumption).

In order to explore the sources of bias, the term $\gamma_{Dk}(\mathbf{x}, \boldsymbol{\theta}_{Dk})$ is expressed as a complete second order polynomial of p_k selected explanatory functions $h_{kj}(\mathbf{x})$ as

$$\gamma_{Dk}(\mathbf{x}, \boldsymbol{\theta}_{Dk}) = \sum_{j=1}^{p_k} \theta_{Dkj} h_{Dkj}(\mathbf{x}) + \sum_{j,r=1}^{p_k} \theta_{Dkjr} h_{Dkj}(\mathbf{x}) h_{Dkr}(\mathbf{x}), \qquad i = 1,...,s \quad k = 1,...,q \tag{2}$$

By examining the posterior statistics of the unknown parameters θ_{Dkj} and θ_{Dkjr}, we are able to identify those explanatory functions that are significant in describing the bias in the deterministic model.

Practically, the explanatory functions are selected based on the underlying physics of the engineering problem, e.g., the factors affecting the dynamic behavior of the structure. The following explanatory functions are selected for the development of the demand models: To capture a possible constant bias that is independent of the variables $\mathbf{x}_i$ in the model, we select $h_{Dk1}(\mathbf{x}) = 1$. To capture a possible systematic under- or over-estimation by the deterministic model, we select $h_{Dk2}(\mathbf{x}) = \hat{d}_{Dki}(\mathbf{x})$. To explore the influence of the amplitude and frequency content of the ground motion and of the geometry difference between the two columns in the same bent, we select $h_{Dk3}(\mathbf{x}) = S_a \cdot (H_I / H_i)$, where H_I is the average height of the two columns in Bent I, and H_i is the height of Column i in Bent I. In the case of a bent with columns of equal height, $h_{Dk3}(\mathbf{x}) = S_a$. To examine the effect of the frequency content in the ground

motion, we select $h_{Dk4}(\mathbf{x}) = 2\pi \cdot (\text{PGV}/\text{PGA}/T_I) \cdot (H_I/H_i)$, where T_I is the fundamental vibration period of Bent I obtained using the force and displacement at Bent I from the pushover analysis of the bridge. To investigate effects of the distribution of stiffness and tributary masses of all bents in the bridge, we select $h_{Dk5}(\mathbf{x}) = T_I/T_n$, where T_n is the fundamental vibration period of the equivalent SDF system in the deterministic demand model. Finally, to gauge the effect of the number of load reversals, which is related to the duration of an earthquake and T_n, we select $h_{Dk6}(\mathbf{x}) = t_D/T_n$, where t_D is the ground motion duration computed according to Trifunac and Brady (1975) as the interval between the times with 5% and 95% of the total energy released. Note that the selected explanatory functions are all dimensionless. As a result, the parameters θ_{Dkj} and θ_{Dkjr} also are dimensionless.

The term $\boldsymbol{\Sigma}_{Dk}$ accounts for the possible correlation among the errors of the demand models of various components and modes of failure. Gardoni et al. (2003) showed that under mild assumptions, $\boldsymbol{\Sigma}_{Dk}$ includes q unknown variances, σ_{Dk}^2, and $s \times q \times (s + s \times q + q - 3)/4$ correlation coefficients, $\rho_{kl}(\mathbf{x}_i, \mathbf{x}_j)$, which describes the linear dependency between the errors for response k in component i and response l in component j. The set of all unknown parameters in Eq. (1) is then given by $\boldsymbol{\Theta}_D = (\boldsymbol{\theta}_D, \boldsymbol{\sigma}_D, \boldsymbol{\Sigma}_D)$, where $\boldsymbol{\theta}_D = (\boldsymbol{\theta}_{D1}, \cdots, \boldsymbol{\theta}_{Dq})$, $\boldsymbol{\sigma}_D = (\sigma_{D1}, \cdots, \sigma_{Dq})$ and $\boldsymbol{\Sigma}_D = (\boldsymbol{\Sigma}_{D1}, \cdots, \boldsymbol{\Sigma}_{Dq})$.

To explore the sources of correlation among the error terms, following Gardoni et al. (2003), we select a suitable set of p_R explanatory functions $h_{Rw}(\mathbf{x}_i, \mathbf{x}_j)$, $w = 1, \cdots, p_R$ and $i, j = 1, \cdots, s$ and express the correlation coefficient between ε_{Dki} and ε_{Dlj} as

$$\rho_{kl}\left(\mathbf{x}_i, \mathbf{x}_j\right) = \frac{\sum_{w=1}^{p_R} \theta_{klw} h_{Rw}(\mathbf{x}_i, \mathbf{x}_j)}{1 + \left| \sum_{w=1}^{p_R} \theta_{klw} h_{Rw}(\mathbf{x}_i, \mathbf{x}_j) \right|}, \quad i, j = 1, \cdots, s \quad k, l = 1, ..., q \tag{3}$$

In the above formulation, different θ_{klw} are defined for the following three cases based on the selection of Column i in Bent I and Column j in Bent J: (1) $i = j$ (the same column); (2) $i \neq j$ and $I = J$ (two columns in the same bent); and (3) $i \neq j$ and $I \neq J$ (two columns in two different bents). In order to capture a potential correlation that is independent of the variables $\mathbf{x}_i$, we select $h_{R1}(\mathbf{x}_i) = 1$. To detect the dependence of the correlation on S_a and on the difference of column height, we select $h_{R2}(\mathbf{x}_i) = S_a \cdot (H_I / H_i) \cdot (H_J / H_j)$. To explore the dependence of the correlation on the different in heights among all columns in the bridge, we select $h_{R3}(\mathbf{x}_i) = \Delta H_{avg} / \Delta H(i, j)$, where ΔH_{avg} is the average height difference among all columns in the bridge, $\Delta H(i, j)$ is the height difference between columns i and j. To capture a potential dependence on the distance between two bents, we select $h_{R4}(\mathbf{x}_i) = \Delta S_{avg} / \Delta S(I, J)$, where ΔS_{avg} is the average distance between any two bents, and $\Delta S(I, J)$ is the distance between Bents I and J. The first two explanatory

functions are considered for the case $i = j$. The first three explanatory functions are considered for $i \neq j$ and $I = J$. All four explanatory functions are used for the case of $i \neq j$ and $I \neq J$. As for the explanatory functions $h_{Dkj}(\mathbf{x}_i)$ in γ_{Dk}, the $h_{Rw}(\mathbf{x}_i, \mathbf{x}_j)$ are dimensionless and, hence, θ_{klw} also are dimensionless.

Model assessment

Through the step-wise deletion process, Zhong et al. (2008a) developed the following probabilistic model for the seismic deformation demands ($k = \delta$) for the RC columns in a general bridge structure with two-column RC bents as

$$D_{\delta i}\left(\mathbf{r}, \boldsymbol{\Theta}_{D\delta}, \varepsilon_{D\delta i} \middle| \mathbf{s}\right) = \theta_{D\delta 1} + \theta_{D\delta 2}\hat{d}_{D\delta i} + \theta_{D\delta 3}\ln\left(S_a \cdot \frac{H_I}{H_i}\right) + \theta_{D\delta 4}\ln\left(2\pi \cdot \frac{\mathrm{PGV}}{\mathrm{PGA} \cdot T_I} \cdot \frac{H_I}{H_i}\right) + \theta_{D\delta 5}\ln\left(\frac{T_I}{T_n}\right) + \sigma_{D\delta}\varepsilon_{D\delta i} \qquad i = 1,..,s \tag{4}$$

In Eq. (4), $D_{\delta i}$ is the natural logarithm of the deformation demand, δ_i, $\boldsymbol{\Theta}_{D\delta} = \{\boldsymbol{\theta}_{D\delta}, \sigma_{D\delta}, \boldsymbol{\Sigma}_{D\delta}\}$, $\boldsymbol{\theta}_{D\delta} = \{\theta_{D\delta 1}, \ldots, \theta_{D\delta 5}\}$ refers to the unknown parameters in the correction term. The vector of random variables, $\mathbf{x}$, has been partitioned into a vector of material and geometry variables, $\mathbf{r}$, and a vector of demand variables, $\mathbf{s} = (S_a, \mathrm{PGV/PGA})$. The term $\hat{d}_{\delta i}$ is the natural logarithm of the deterministic prediction based on Gardoni et al. (2003).

The seismic shear demands ($k = v$) is

$$D_{vi}\left(\mathbf{r},\boldsymbol{\Theta}_{Dv},\varepsilon_{Dvi}\middle|\mathbf{s}\right)=\theta_{Dv1}+\theta_{Dv2}\hat{d}_{Dvi}+\theta_{Dv3}\hat{d}_{D\delta i}+\theta_{Dv4}\ln\left(S_a\cdot\frac{H_I}{H_i}\right)$$
$$+\theta_{Dv5}\ln\left(2\pi\cdot\frac{\mathrm{PGV}}{\mathrm{PGA}\cdot T_I}\cdot\frac{H_I}{H_i}\right)+\theta_{Dv6}\ln\left(\frac{T_I}{T_n}\right)+\sigma_{Dv}\varepsilon_{Dvi} \quad (5)$$

Similarly, we $\boldsymbol{\Theta}_{Dv}=\{\boldsymbol{\theta}_{Dv},\sigma_{Dv},\boldsymbol{\Sigma}_{Dv}\}$, $\boldsymbol{\theta}_{Dv}=\{\theta_{Dv1},\ldots,\theta_{Dv6}\}$, The additional explanatory function $\hat{d}_{D\delta i}$ is included in the probabilistic model. We note that all the second order terms and the explanatory function t_D/T_n are removed through the model selection process. Further, we define the row vector $\boldsymbol{\varepsilon}_{Dki}=\{\varepsilon_{D\delta i},\varepsilon_{Dvi}\}$

The marginal posterior distribution of the model parameters $\boldsymbol{\theta}_{Dk}$ $(k=\delta,v)$ is the multivariate t distribution (Box and Tiao 1992). Table 1 and Table 2 list the posterior statistics of $\boldsymbol{\theta}_{Dk}$ for $k=\delta$ and $k=v$, respectively. The marginal posterior distribution of σ_{Dk}^2 $(k=\delta,v)$ is the inverse chi-square distribution, $\eta\cdot(stdev)^2\cdot\chi_\eta^{-2}$, where $\eta=n-p_k$ n is the number of data points and $stdev$ is the sample standard deviation of

Table 1. Posterior statistics in the updated deformation demand model

$\boldsymbol{\theta}_{D\delta}$	Mean	Standard Deviation	Correlation Coefficient				
			$\theta_{D\delta1}$	$\theta_{D\delta2}$	$\theta_{D\delta3}$	$\theta_{D\delta4}$	$\theta_{D\delta5}$
$\theta_{D\delta1}$	–4.20	0.209	1.0				
$\theta_{D\delta2}$	0.145	0.049	0.99	1.0			
$\theta_{D\delta3}$	0.774	0.045	–0.93	–0.93	1.0		
$\theta_{D\delta4}$	0.264	0.009	0.36	0.38	–0.26	1.0	
$\theta_{D\delta5}$	0.348	0.037	0.48	0.45	–0.38	0.03	1.0

Table 2. Posterior statistics for the shear demand model

Parameter	Mean	Standard Deviation	Correlation Coefficient					
			θ_{Dv1}	θ_{Dv2}	θ_{Dv3}	θ_{Dv4}	θ_{Dv5}	θ_{Dv6}
θ_{Dv1}	8.36	0.461	1.0					
θ_{Dv2}	0.229	0.035	–0.96	1.0				
θ_{Dv3}	–0.213	0.031	0.54	–0.29	1.0			
θ_{Dv4}	0.467	0.027	–0.13	–0.13	–0.84	1.0		
θ_{Dv5}	0.112	0.009	0.76	–0.72	0.47	–0.08	1.0	
θ_{Dv6}	–0.793	0.035	0.30	–0.17	0.48	–0.39	0.11	1.0

the residuals, i.e., the difference between the measured data and the predictions from the probabilistic demand models. The mean and standard deviation of $\sigma_{D\delta}$ are 0.369 and 0.0823, respectively. The mean and standard deviation of σ_{Dv} are 0.206 and 0.047, respectively.

The correlation coefficients $\rho_{kl}(\mathbf{x}_i, \mathbf{x}_j)$ are estimated using Eq. (3). After removing the terms that are not statistically significant, the correlation matrix, $\mathbf{R} = [\rho_{kl}]$ takes the structure shown in Table 3.

Table 4 shows the values of the estimated correlation coefficients. The following observations are made in regard to the correlation coefficients listed in Table 4:

- As expected, the deformation demands of two columns in the same bent are highly correlated, $\rho_{\delta\delta}(i = j) = 0.99$. The same observation is made for the shear demands, $\rho_{vv}(i = j) = 0.99$;

Table 3. Structure of the correlation matrix $\mathbf{R} = [\rho_{kl}]$ $(k, l = \delta, v)$

	Bent 1	Bent I	Bent N
Bent 1	$\rho_{kl}(i=j)$ $\rho_{kl}(i\neq j; I=J)$ $\rho_{kl}(i=j)$		$\rho_{kl}(i\neq j; I\neq J)$
Bent I		$\ddots$ $\ddots$	
Bent N	Symmetric		$\rho_{kl}(i=j)$ $\rho_{kl}(i\neq j; I=J)$ $\rho_{kl}(i=j)$

Note: $\rho_{kl}(i=j)$ is the correlation coefficient for the same column;
$\rho_{kl}(i\neq j; I=J)$ is the correlation coefficient for two different columns in the same bent;
$\rho_{kl}(i\neq j; I\neq J)$ is the correlation coefficient for any two columns in different bents.

Table 4. Correlation coefficients for the demand models

	$\rho_{kl}(i=j)$	$\rho_{kl}(i\neq j; I=J)$	$\rho_{kl}(i\neq j; I\neq J)$
$k=\delta$, $l=\delta$	1.0	0.99	0.35
$k=\delta$, $l=v$	–0.84	–0.85	–0.37
$k=v$, $l=v$	1.0	0.99	0.56

- The deformation demands on any two columns in different bents are moderately correlated, $\rho_{\delta\delta}(i\neq j; I\neq J) = 0.35$. The same observation is made for the shear demands, $\rho_{vv}(i\neq j; I\neq J) = 0.56$;
- The random errors in deformation and shear demands of the same column are negatively correlated. This indicates that when the random errors in deformation demands increase, the random errors in shear demand tend to decrease and vice versa.

Fig. 2 shows a comparison between the measured and predicted values of the deformation demands based on the deterministic (left chart) and the updated probabilistic (right chart) models. For the probabilistic model the median predictions are shown. For a perfect model, the data should line up along the 1:1 lines. The deterministic model is biased on the conservative side for the data from the modified I-880 (denoted by ▷) and on the unconservative side for most of the data from the single bents (denoted by •). The data from three-bent system (denoted by ○) scatter around the 1:1 line Furthermore, the model presents an overall large scatter. The probabilistic model corrects the bias in the deterministic model and reduces the overall scatter. The dashed lines in the bottom chart delimit the region within one standard deviation of the 1:1 line. We note that, as per construction, the majority of data points from the three datasets fall within the one standard region.

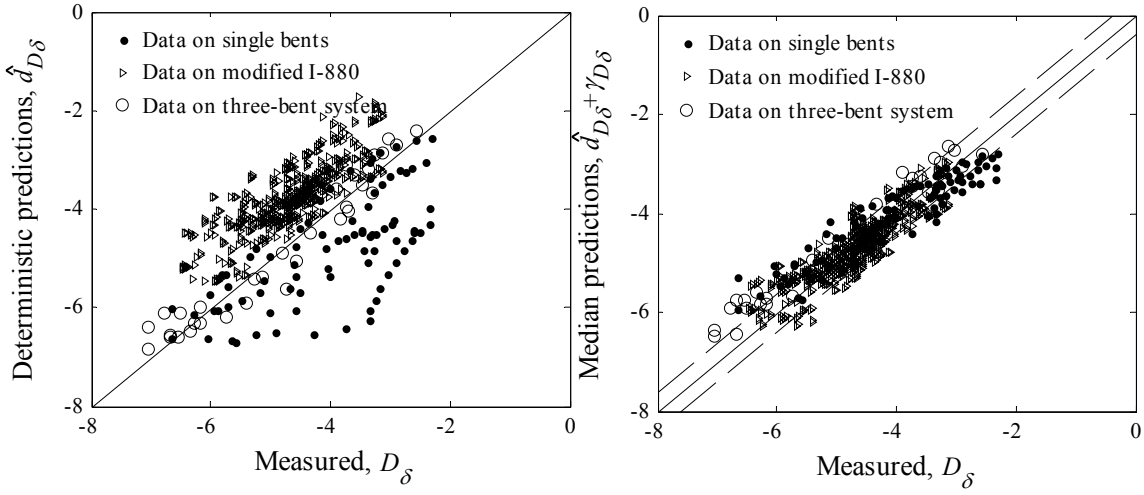

Fig. 2. Comparison between measured and predicted deformation demands based on deterministic (left) and probabilistic (right) models

Fig. 3 shows a comparison between the measured and predicted values of the shear demands correspondingly. The left plots show the predicted demands based on the deterministic model only. The right plots show the mean demands predicted based on the probabilistic models that account for the model correction terms γ_{Dv}. The solid dots (•) represent the laboratory data and the right triangles (▷) represent the simulated data.

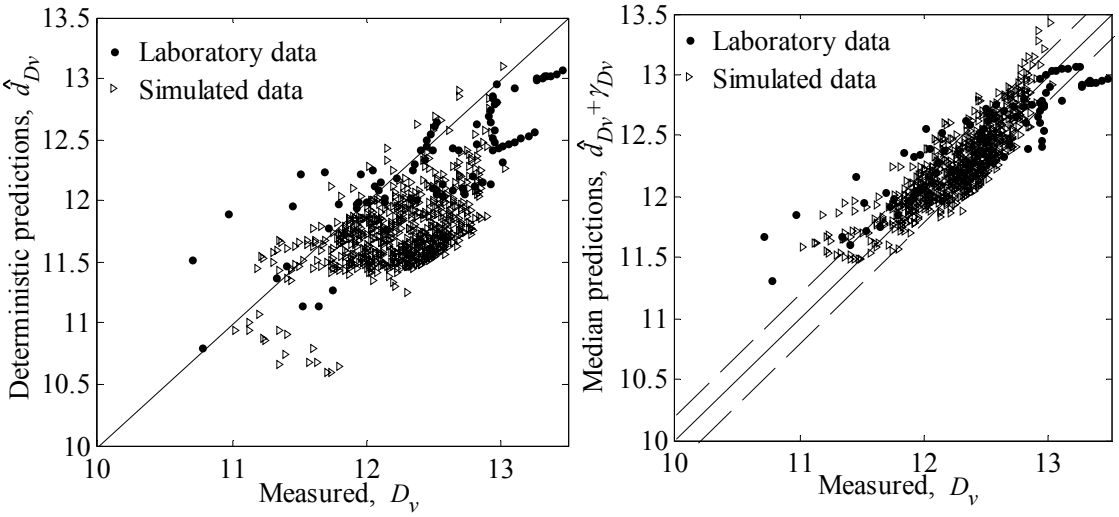

Fig. 3. Comparison between measured and predicted shear demands based on deterministic (left) and probabilistic (right) models

It is also observed that the probabilistic models are unbiased and reduce the scatter present in the corresponding deterministic models.

As an aside note, it is mentioned that the quality of the presented results depends on the quality of the data. If the data are unbiased then the resulting models are also unbiased. However, if the data are biased and have a systematic error, then the resulting

models are also biased. Before the fragility estimation, the probabilistic capacity models used in the fragility formulation are first introduced in the next.

Probabilistic capacity models

For the column capacities, we use the probabilistic models for Column i developed by Gardoni et al. (2002) and later updated in Choe et al. (2007). The deformation capacity model, $C_{\delta i}$, is written as

$$C_{\delta i} = \hat{c}_{\delta i} + \theta_{C\delta 1} + \theta_{C\delta 7} \cdot \frac{4V_I}{\pi D_g^2 f_t'} + (-6.035 - 1.034\theta_{C\delta 11}) \cdot \frac{\rho_s f_{yh} D_c}{f_c' \cdot D_g} + \theta_{C\delta 11}\varepsilon_{cu} + \sigma_{C\delta}\varepsilon_{C\delta i} \qquad (6)$$

and the shear capacity, C_{vi}, as

$$C_{vi} = \hat{c}_{vi} + \theta_{Cv2}\rho_l + \theta_{Cv4}\frac{A_v f_{yh} D_g}{A_g f_t' S} + \sigma_{Cv}\varepsilon_{Cvi} \qquad (7)$$

In Eq. (6), $C_{\delta i}$ is the natural logarithm of the drift ratio capacity, $\ln[\Delta / H]$, where Δ is the deformation capacity, and $\hat{c}_{\delta i}$ is the natural logarithm of the drift ratio capacity of Column i (or a suitable transformation thereof) predicted by a selected deterministic capacity model. The term $4V_I/(\pi D_g^2 f_t')$ captures the effects of the idealized elastic-perfectly plastic shear force in the column, V_I, where D_g is the gross diameter of the column, and $f_t' = 0.5\sqrt{f_c'}$ is the tensile strength of concrete. The term $\rho_s(f_{yh}/f_c')(D_c/D_g)$ captures the influences of the confining transverse reinforcement and core size, where ρ_s is the ratio of the volumetric confining reinforcements, f_{yh} is the yielding stress of confining reinforcement, D_c is the column-core diameter, f_c' is the

compressive strength of the concrete. Finally, ε_{cu} captures the effect of the ultimate strain of the confined concrete. In Eq. (6) $\theta_{C\delta 1}$, $\theta_{C\delta 7}$, and $\theta_{C\delta 11}$ are the model parameters that are assessed using experimental data. We define the row vector $\boldsymbol{\theta}_{C\delta} = \{\theta_{C\delta 1}, \theta_{C\delta 7}, \theta_{C\delta 11}\}$. The letter "*C*" in the subscripts denotes that they are for the capacity model. Finally, $\sigma_{C\delta}\varepsilon_{C\delta i}$ represents the model error, where $\varepsilon_{C\delta i}$ is a standard random variable, and $\sigma_{C\delta}$ represents the standard deviation of the model error.

Similarly, in Eq. (7), $C_{\delta i}$ is the natural logarithm of the normalized shear capacity, $\ln[V/(A_g f_t')]$, where $V/(A_g f_t')$ is the normalized shear capacity, V is the shear capacity, and A_g is the gross area of column cross-section. The term $\hat{c}_{vi}$ is the natural logarithm of the normalized shear capacity predicted by the selected deterministic capacity model for Column i. Two explanatory functions are used to correct for the bias inherent in $\hat{c}_{vi}$. The first function, ρ_l, corrects for the contribution of the longitudinal steel, where ρ_l is the ratio of longitudinal reinforcements in the column. The second function, $A_v f_{yh} D_g/(A_g f_t' S)$, corrects for the contribution of the transverse steel, where A_v is the total area in a layer of the confining reinforcement in the direction of shear force in the column, and S is the spacing of confining reinforcement. As for the deformation model, $\boldsymbol{\theta}_{Cv} = \{\theta_{Cv2}, \theta_{Cv4}\}$ is the row vector of the model parameters assessed using experimental data. Finally, $\sigma_{Cv}\varepsilon_{Cvi}$ represents the model error, where each term is defined as for the deformation model. We define the row vector $\boldsymbol{\varepsilon}_{Cki} = \{\varepsilon_{C\delta i}, \varepsilon_{Cvi}\}$. Similarly to the demand models, we can define $\boldsymbol{\Theta}_C = (\boldsymbol{\theta}_C, \boldsymbol{\sigma}_C, \boldsymbol{\Sigma}_C)$,

where $\boldsymbol{\theta}_C = (\boldsymbol{\theta}_{C\delta}, \boldsymbol{\theta}_{Cv})$, $\boldsymbol{\sigma}_C = (\sigma_{C\delta}, \sigma_{Cv})$ and $\boldsymbol{\Sigma}_C = (\boldsymbol{\Sigma}_{C\delta}, \boldsymbol{\Sigma}_{Cv})$ for deformation and shear capacity models. Table 5 and Table 6 list the posterior statistics of $\boldsymbol{\Theta}_{C\delta} = \{\boldsymbol{\theta}_{C\delta}, \sigma_{C\delta}, \boldsymbol{\Sigma}_{C\delta}\}$ and $\boldsymbol{\Theta}_{Cv} = \{\boldsymbol{\theta}_{Cv}, \sigma_{Cv}, \boldsymbol{\Sigma}_{Cv}\}$, respectively.

For capacity $C_{ki}(\mathbf{r}, \boldsymbol{\Theta}_{Ck}, \varepsilon_{Cki})$ in Eq. (9) We use the probabilistic deformation and shear capacity models developed by Gardoni et al. (2002) and Choe et al. (2007). However, Choe et al. (2007) developed probabilistic capacity models for single-column bents. In this section, we explore the relation between the deformation and shear capacities of a single-column bent and the same quantities for a column in a two-column Bent.

Table 5. Posterior statistics of the parameters in the deformation capacity model (Choe et al. 2007)

$\boldsymbol{\Theta}_{C\delta}$	Mean	Standard Deviation	Correlation coefficient			
			$\theta_{C\delta 1}$	$\theta_{C\delta 7}$	$\theta_{C\delta 11}$	$\sigma_{C\delta}$
$\theta_{C\delta 1}$	0.675	0.105	1			
$\theta_{C\delta 7}$	0.631	0.133	–0.27	1		
$\theta_{C\delta 11}$	–57.5	10.1	–0.65	–0.39	1	
$\sigma_{C\delta}$	0.400	0.045	0.39	–0.06	–0.13	1

Table 6. Posterior statistics of the parameters in the shear capacity model (Choe et al. 2007)

$\boldsymbol{\Theta}_{Cv}$	Mean	Standard Deviation	Correlation coefficient		
			θ_{Cv2}	θ_{Cv4}	σ_{Cv}
θ_{Cv2}	18.3	1.45	1		
θ_{Cv4}	–0.470	0.078	–0.87	1	
σ_{Cv}	0.185	0.018	–0.04	–0.02	1

The deformation capacity for a single-column bent with height L is defined as $C_\delta = Z/L$, where Z is the relative displacement capacity between the top and bottom of the column (Fig. 4). The deformation capacity of a column in a two-column bent is computed herein as $C_\delta = z/(L/2) = 2z/L$, where z is the relative displacement capacity of a single column bent of height $L/2$. As shown in Fig. 4, the deformation capacity of a column in a two-column bent generally is smaller than the capacity of in a single-column bent of the same height. The shear capacity for a column in a two-column bent is the same as that in a single-column bent.

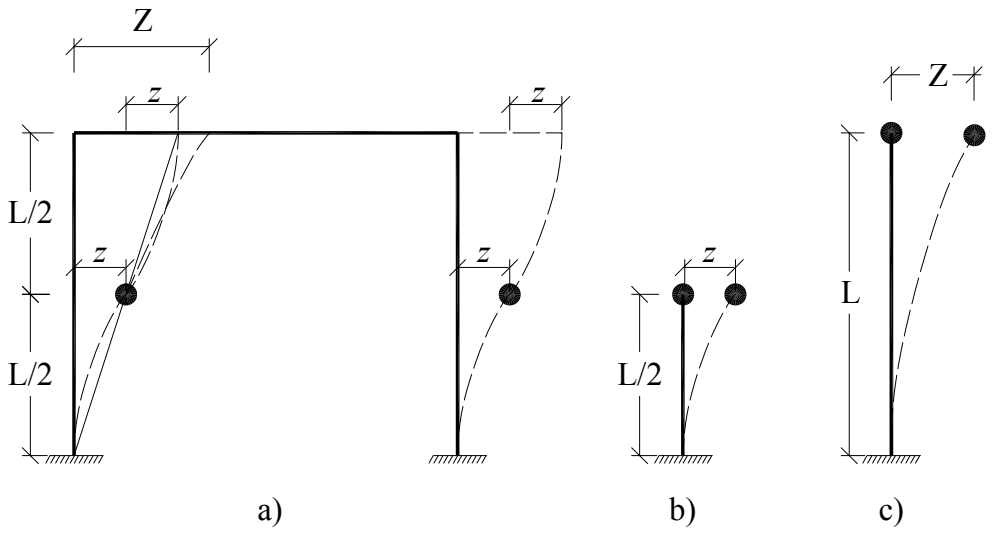

Fig. 4. Deformation capacities for the columns in two-column bent

FRAGILITY ESTIMATES FOR RC BRIDGES WITH TWO-COLUMN BENTS

The fragility of a bridge consisting of s structural components for given seismic intensity $\mathbf{s}$ is written as

$$F(\mathbf{s},\boldsymbol{\Theta}) = P\left[\bigcup_{i=1,..,s}\ \bigcup_{k=\delta,v}\left\{g_{ki}\left(\mathbf{r},\boldsymbol{\Theta}_k,\boldsymbol{\varepsilon}_{ki}\middle|\mathbf{s}\right)\le 0\right\}\right] \tag{8}$$

where $\boldsymbol{\Theta} = (\boldsymbol{\Theta}_C, \boldsymbol{\Theta}_D)$, $\boldsymbol{\Theta}_k = (\boldsymbol{\Theta}_{Ck}, \boldsymbol{\Theta}_{Dk})$, $\boldsymbol{\varepsilon}_{ki} = (\varepsilon_{Cki}, \varepsilon_{Dki})$ and $g_{ki}(t,\mathbf{r},\boldsymbol{\Theta},\boldsymbol{\varepsilon}_{ki}\,|\,\mathbf{s})$ is the limit state function for Column i, expressed as

$$g_{ki}\left(\mathbf{r},\boldsymbol{\Theta}_k,\boldsymbol{\varepsilon}_{ki}\middle|\mathbf{s}\right) = C_{ki}\left(\mathbf{r},\boldsymbol{\Theta}_{Ck},\varepsilon_{Cki}\right) - D_{ki}\left(\mathbf{r},\boldsymbol{\Theta}_{Dk},\varepsilon_{Dki}\middle|\mathbf{s}\right)\le 0,\quad i=1,..,s;\quad k=\delta,v \tag{9}$$

A predictive estimate of Eq. (8) is obtained as the mean of $F(\mathbf{s},\boldsymbol{\Theta})$ by integrating over the distribution of $\boldsymbol{\Theta}$ as

$$\tilde{F}(\mathbf{s}) = \int_{\boldsymbol{\Theta}} F\left(t,\mathbf{s},\boldsymbol{\Theta}\right) f_{\boldsymbol{\Theta}}\left(\boldsymbol{\theta}\right) d\boldsymbol{\theta} \tag{10}$$

A point estimate of Eq. (8) at time t is obtained by ignoring the epistemic uncertainties in the model parameters, $\boldsymbol{\Theta}$, and using a point estimate, $\hat{\boldsymbol{\Theta}}$ (e.g., the mean of $\boldsymbol{\Theta}$), instead of $\boldsymbol{\Theta}$. Then the point estimate of seismic fragility for the bridge can be written as

$$\hat{F}(\mathbf{s}) = F\left(\mathbf{s},\hat{\boldsymbol{\Theta}}\right) \tag{11}$$

In the special cases where vector $\mathbf{r}$ are known for a given bridge, $\hat{F}(\mathbf{s})$ can be computed in terms of multinormal probability distribution function of $\boldsymbol{\varepsilon}_{ki}$ depending on the number of limit state functions under consideration. In the following, the point estimates of

fragility are presented considering one-, two-, and multiple- limit states functions for column, bent, and bridge levels, respectively.

When only one limit state is considered, we have the following approximated closed-form solution for the fragility of Column i in mode k of failure

$$\begin{aligned}\hat{F}(\mathbf{s}) &= P\left[g_{ki}\left(\hat{\mathbf{r}}, \hat{\boldsymbol{\Theta}}_k, \boldsymbol{\varepsilon}_{ki} \middle| \mathbf{s}\right) \le 0 \right] \\ &= P\left[C_{ki}\left(\mathbf{r}, \boldsymbol{\Theta}_{Ck}, \varepsilon_{Cki}\right) - D_{ki}\left(\mathbf{r}, \boldsymbol{\Theta}_{Dk}, \varepsilon_{Dki} \middle| \mathbf{s}\right) \le 0 \right] \\ &= 1 - \Phi\left(u_{ki}\right)\end{aligned} \tag{12}$$

where $\Phi(\cdot)$ is the cumulative density function (CDF) of the univariate standard normal random variable, and $u_{ki} = -\hat{\mu}_{g_{ki}} / \hat{\sigma}_{g_{ki}}$, where $\hat{\mu}_{g_{ki}}$ and $\hat{\sigma}_{g_{ki}}$ are the point estimates of the mean and the standard deviation of $g_{ki}(\cdot)$ defined in Eq. (9).

When two limit state functions are considered for the following three cases: (1) the fragility of a single RC column in either deformation or shear mode of failure (2) the fragility of a bent in deformation mode of failure, and (3) the fragility of a bent in shear mode of failure, we have the fragility function, e.g., for the first case, expressed as

$$\begin{aligned}P\left[\bigcup_{k=\delta,v} g_{ki}\left(\mathbf{r}, \boldsymbol{\Theta}_k, \boldsymbol{\varepsilon}_{ki} \middle| \mathbf{s}\right) \le 0 \right] &= 1 - P\left[\bigcap_{k=\delta,v} g_{ki}\left(\mathbf{r}, \boldsymbol{\Theta}_k, \boldsymbol{\varepsilon}_{ki} \middle| \mathbf{s}\right) > 0 \right] \\ &= 1 - P\left[\bigcap_{k=\delta,v} \left\{ D_{ki}\left(\mathbf{r}, \hat{\boldsymbol{\Theta}}_{Dk}, \varepsilon_{Dki} \middle| \mathbf{s}\right) - C_{ki}\left(\mathbf{r}, \hat{\boldsymbol{\Theta}}_{Ck}, \varepsilon_{Cki}\right) < 0 \right\} \right] \\ &= 1 - \Phi_2\left(-u_{\delta i}, -u_{vi}; \hat{\rho}_{\delta_i, v_i}\right)\end{aligned} \tag{13}$$

where $\Phi_2(\cdot)$ is the CDF of bivariate standard normal random variables, $\hat{\rho}_{\delta_i,v_i}$ is the point estimate of the correlation coefficient between $u_{\delta i}$ and u_{vi}. To evaluate $\Phi_2(-u_{\delta i},-u_{vi};\hat{\rho}_{\delta_i,v_i})$, we can use the following single integral expression:

$$\Phi_2\left(-u_{\delta i},-u_{vi};\hat{\rho}_{\delta_i,v_i}\right)=\Phi\left(-u_{\delta i}\right)\Phi\left(-u_{vi}\right)+\int_0^{\hat{\rho}_{\delta_i,v_i}}\varphi_2\left(-u_{\delta i},-u_{vi};\hat{\rho}\right)d\hat{\rho}, \tag{14}$$

where $\varphi_2(\cdot)$ is the bivariate probability density function (PDF). For the second and third cases, similar formulations are applicable.

Further, when more than two limit states are considered in fragility estimation, the point estimate for Eq. (8) can be formulated as

$$\begin{aligned}\hat{F}\left(\mathbf{s}\right)&=P\left[\bigcup_{i=1,..,s}\bigcup_{k=\delta,v}\left\{g_{ki}\left(\mathbf{r},\hat{\boldsymbol{\Theta}}_k,\boldsymbol{\varepsilon}_{ki}\middle|\mathbf{s}\right)\le 0\right\}\right]\\&=1-P\left[\bigcap_{i=1,..,s}\bigcap_{k=\delta,v}\left\{g_{ki}\left(\mathbf{r},\hat{\boldsymbol{\Theta}}_k,\boldsymbol{\varepsilon}_{ki}\middle|\mathbf{s}\right)>0\right\}\right]\\&=1-\Phi_{2s}\left(-\mathbf{u};\hat{\boldsymbol{\rho}}\right)\end{aligned} \tag{15}$$

where $\Phi_{2s}(\cdot)$ is the CDF of multivariate standard normal random variables of dimension $2s$, $\mathbf{u}=(u_{k1},u_{k2},...,u_{ks})$, $\hat{\boldsymbol{\rho}}=(\hat{\rho}_{k_i,l_j})$ is the matrix of correlation coefficients estimated for random vector $\mathbf{u}$.

NUMERICAL EXAMPLES

As an application of the proposed approach, this section develops fragility estimates for the modified I-880 viaduct described previously. In particular, we consider (1) the fragility of a single column considering both deformation and shear modes of failure, (2)

the fragility of a two-column bent in deformation, (3) the fragility of a two-column bent in shear, and (4) the fragility of the entire bridge considering both deformation and shear modes of failure.

Fig. 5 shows the contour lines of the deformation and the shear fragility estimates of the northern column in Bent 8. The dashed lines represent the point estimates and the solid lines represent the predictive estimates. Each contour line connects pairs of values of the demands S_a and PGV/PGA that are associated with a given level of fragility in the range of 0.1–0.9 and two additional values 10^{-4} and 10^{-2}. It is observed that there is only a small difference between the point and predictive estimates for both deformation and shear fragilities. In the two extreme cases, i.e., small values of S_a and PGV/PGA and large values S_a and PGV/PGA, the difference between these two fragility estimates is, as expected, marginally more pronounced. The difference arises because the predictive estimates incorporate more uncertainties making the fragility surface flatter. However, for practical purposes, point estimates are sufficiently accurate to predict the fragility. In the following analysis, we use point estimates to compute individual column, bent, and bridge system fragilities.

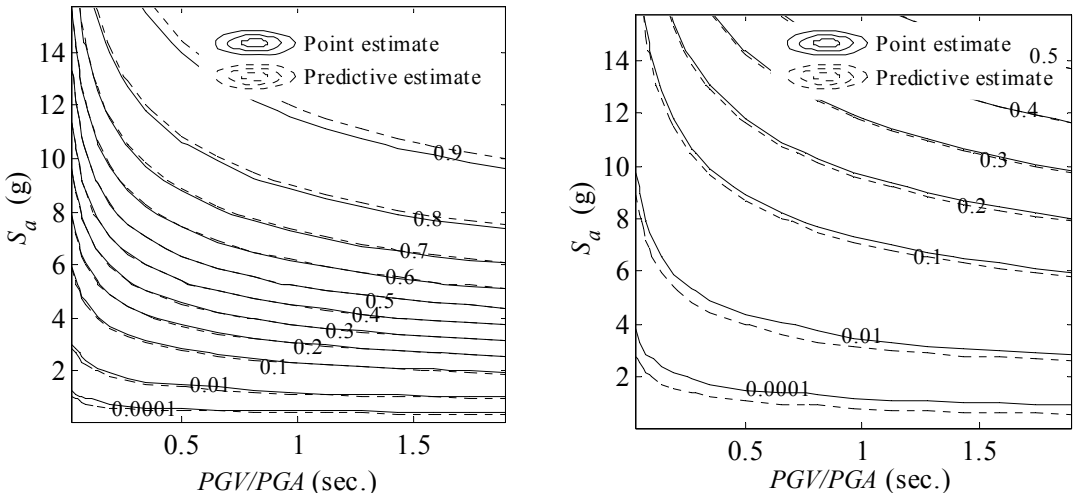

Fig. 5. Point and predictive estimates of the fragility of the northern column in Bent 8 based on deformation (left) and shear (right) modes

Fig. 6 shows the contour lines for the fragility estimates for the northern column in Bent 8 as per the orientation shown in Kunnath (2007). The average bent height of Bent 8 is 14.7 m with column cross sections of 2.59×2.43 m. The dashed lines show the deformation fragility, the dashed-dotted lines show the shear fragility, and the solid lines show the conditional probability that the column fails in either deformation or shear mode. It can be seen that the deformation failure mode dominates the column fragility. This is consistent with the displacement-based capacity design approach used by Caltrans (Caltrans 2006). Similar fragility surfaces can be obtained for all columns in Bents 1-8.

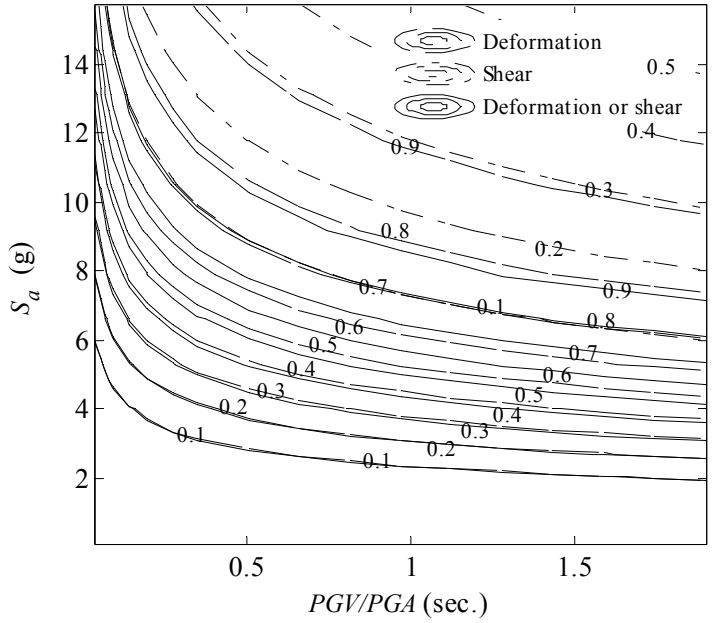

Fig. 6. Point estimates of the fragility of the northern column in Bent 8

Fig. 7 shows the contour lines for the fragility estimates for the northern column in Bent 11. The average bent height of Bent 11 is 10.7 m with column cross sections of 2.29×2.03 m. We observe that the shear fragility is now more prominent. This is because of the reduced shear capacity of the northern column in Bent 11 due to its smaller cross-section. Similar fragility surfaces can be obtained for all columns in Bents 9-11.

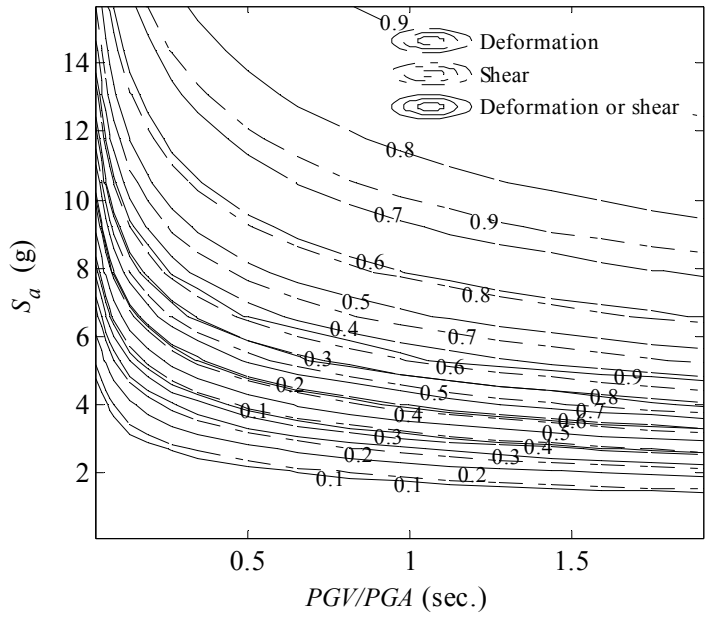

Fig. 7. Point estimates of the fragility of the northern column in Bent 11

Fig. 8 shows the contour lines for fragility estimates for Bents 8 (left chart) and 11 (right chart). It is seen that the deformation fragility and the shear fragility of Bent 8 are similar to the deformation fragility and the shear fragility for the individual column shown in Fig. 6. Similar observations can be made for Bent 11. This is to be expected given the high correlation between the deformation (and shear) demands of the northern and southern columns. Similarly we can obtain the fragility surface for each bent in the bridge system.

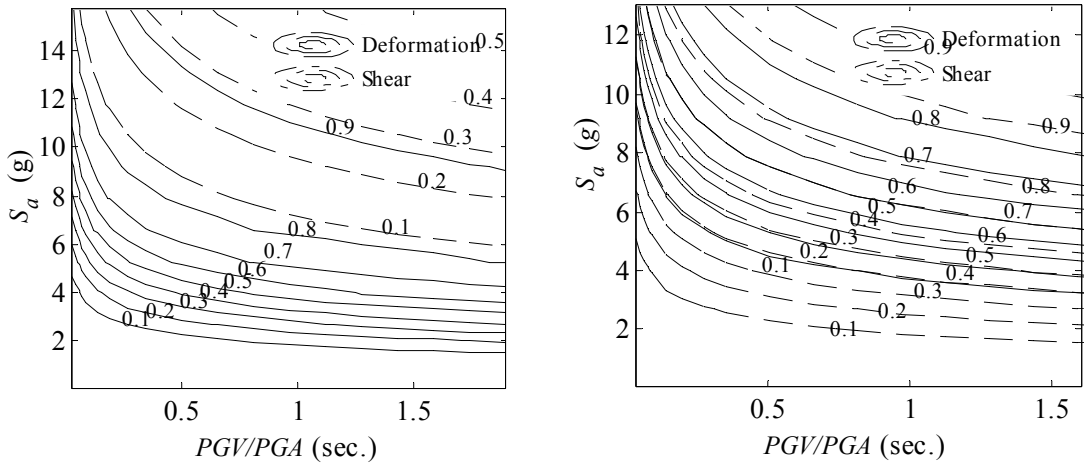

Fig. 8. Point estimates of fragility of Bents 8 (left) and 11 (right)

The fragility of the entire bridge is estimated using the Monte Carlo sampling capabilities in OpenSees. One percent coefficient of variation of the probability result is used as analysis termination criterion. The estimates of the bridge fragility are shown in Fig. 9. The left chart shows the fragility estimates for deformation (dashed lines) and shear (bold dashed-dotted lines) modes of failure. The right chart shows the conditional probability of failure in either deformation or shear mode (bold solid lines). It is seen that, because of the limited shear capacity in the columns in Bents 9 to 11 already observed in Fig. 7. The shear failure mode controls the failure of this bridge system in low failure probabilities, while it is comparable to deformation mode of failure in high failure probabilities. As a general comment, it is observed that the fragility contours are more sensitive to a change in S_a than in PGV/PGA.

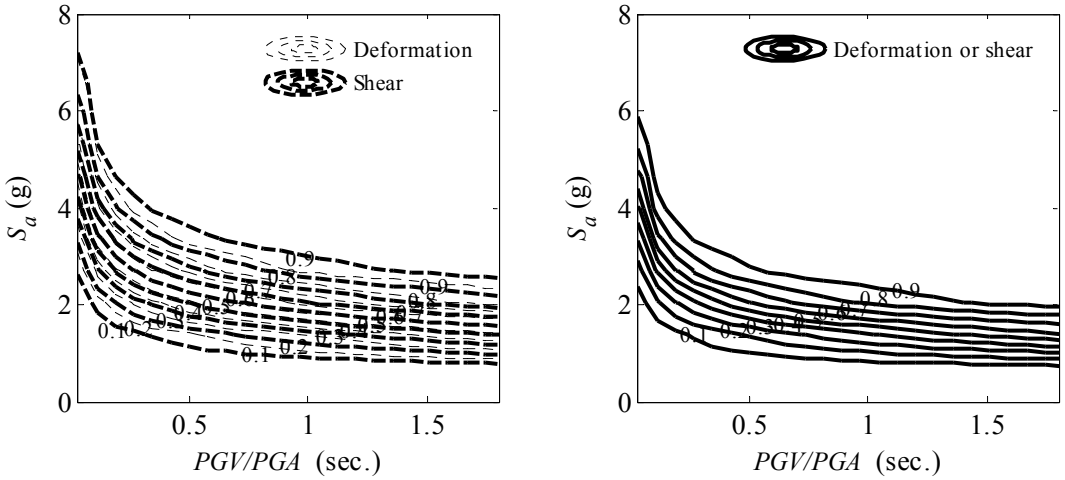

Fig. 9. Point estimates of the fragility of the modified I-880 viaduct based on deformation and shear modes (left) and based on deformation or shear mode (right)

SUMMARY

The development of probabilistic models for the deformation and shear demands of RC columns in two-column bents subject to seismic excitation are presented in this Chapter. The models are developed based on an accepted deterministic procedure. A correction term is developed to capture the inherent systematic and random errors. A set of explanatory functions is used to correct for the bias and to gain insight into the underlying behavioral phenomena. The developed probabilistic models account for the information gained from both laboratory experimental data and nonlinear time-history analyses. Correlation coefficients among deformation and shear demands are estimated to capture the dependency among the demand quantities.

The following comments are made with regard to the probabilistic demand models:

- The spectral acceleration at the natural period of the structure and ratio between the peak ground velocity and the peak ground acceleration are selected as the most relevant ground motion parameters for seismic demands;
- The deformation (and shear) demands of two columns in the same bent are highly correlated;
- The random errors in deformation and shear demands of any two columns are shown to be negatively correlated. This means that when the random errors in deformation demand are increasing, the random errors in shear demands are likely to decrease, and vice versa.

Fragility estimates are next computed at the individual column, bent, and bridge system levels for an example bridge designed according to current specifications for California (Caltrans 1999). The following conclusions are made with regard to the fragility estimates:

- For practical purposes, point estimates provide accurate estimates of the fragility surfaces. Neglecting the epistemic uncertainty in the model parameters leads only to a marginal difference in the tails of the fragility surfaces.
- The fragility estimates of a bent are similar to the fragility estimates of an individual column in that bent since the deformation and shear demands in both columns of the same bent are highly correlated.
- The deformation failure mode dominates the failure of most columns in the example bridge considered. This is consistent with the displacement-based capacity design approach used by Caltrans. However, a change in the stiffness

and cross-sectional properties of a column can make the shear failure mode more prominent.

- The fragility contours are more sensitive to changes in S_a than in PGV / PGA.

CHAPTER III

SIMPLIFIED FORMULATION TO ESTIMATE THE FRAGILITY OF RC BRIDGE STRUCTURES WITH TWO-COLUMN BENTS

To facilitate the application of the developed probabilistic capacity and demand models, this chapter proposes a simplified formulation to estimate the seismic fragility based on the importance measures of all parameters included in the probabilistic models for capacity and seismic demands. Seismic fragility estimated using the proposed formulation is only marginally different from the fragility estimated using accurate methods.

INTRODUCTION

Ensuring acceptable seismic performance of RC columns is crucial in maintaining the functionality of bridges built in seismic regions. The vulnerability of a RC column can be expressed as the conditional probability (or fragility) that the RC column does not perform adequately (considering relevant demands, e.g., in deformation or shear) during a seismic excitation. However, an analytical solution is not available for the fragility estimation of a RC column, since the analytical form of limit state function and the failure domain are not always explicitly available. In this chapter, important uncertainties are selected by considering the importance measures of the random variables in the fragility estimation. A simplified solution for fragility estimates is then developed incorporating only the important uncertainties in the fragility estimation.

Based on functional or geographical reasons, a multiple-column, including two-column, bent structure is preferred over single-column configuration (Sritharan et al. 2001). This is mainly because a multiple-column configuration has the advantage of reducing the cost of the substructure by having a pin connection between the column and the footing instead of a fixed connection as per single-column bents (Sritharan et al. 2001).

For the seismic behavior of RC columns, much work has been done in the laboratory (Kunnath et al. 1997; Hachem 1999; Laplace et al. 1999, 2001; Saiidi et al. 2000; Nelson 2000; Stapleton et al. 2005). Further, fragility curves have been developed for bridges with single-column bents(e.g., Karim and Yamazaki 2001, 2003, 2007; Gardoni et al. 2002, 2003; Monti and Nistico 2002; Kim and Feng 2003; Kim and Shinozuka 2003; Lu et al. 2005; Oller and Barbat 2006; Lupoi et al. 2006; Choi et al. 2006; Banerjee and Shinozuka 2007; and Jeong and Elnashai 2007). Among these studies, Gardoni et al. (2002, 2003) developed fragility curves for single-column bents and bridge systems with single-column bents using probabilistic capacity and demand models developed using a Bayesian methodology. The capacity and demand models are unbiased and properly account for all the predominant uncertainties, including model errors (arising from an inaccurate model form or missing variables), measurement errors, and statistical uncertainty. The models takes into account information gained from scientific/engineering laws, observational data from laboratory experiments, and data from simulated dynamic responses.

In contrast, very little work has been done to assess the seismic vulnerability of bridge structures with two-column bents, although some experimental work has been reported both in the field (Pantelides et al. 1999) and in the laboratory (Gulkan et al 1971; MacRae et al. 1994; Terayama et al. 1996; Sexsmith et al. 1997; Moore 2000; Sritharan et al. 2001; Nada 2003; Sureshkumar 2004; Moustafa 2004; and Pulido et al. 2004, Johnson 2006). Among these studies, Johnson (2006) conducted a quarter-scale full bridge test on a shake table with ramped 1994 Northridge Earthquakes excited along the transverse direction of the bridge. Limited work has been done, however, to develop the fragility estimates for bridge structure with two-column bents. For example, Shinozuka et al. (2000) used the capacity spectrum method to construct the fragility curves for bridge structures with two-column bents. Kunnath et al. (2006) evaluated the probability of closure of the I-880 viaduct with 11 two-column RC bents by applying a performance-based methodology. Zhong et al. (2008a) estimated the fragility surfaces at the component (column of two-column bent), subsystem (bent), and system (bridge structure) levels using newly developed probabilistic demand models for RC columns in two-column bents.

In this chapter, we develop (1) an approximate closed-form solution for the fragility estimation of RC columns in two-column bents, and (a) a simplified point estimate of the fragility for bridge systems (Zhong et al. 2008c). As an illustration, the closed-form fragility estimates of two typical RC columns subject to deformation and shear failures are compared with the predictive fragility estimates developed in Zhong et al. (2008a). The fragility formulation of the RC column is developed based on the

probabilistic capacity models proposed by Gardoni et al. (2002) and Choe et al. (2007) and the corresponding seismic demand models developed by Zhong et al. (2008a). The seismic intensity is expressed in terms of S_a of the equivalent SDF system of the bridge structure and PGV/PGA. Sensitivity and importance measures are computed for the variables defined in the capacity and demand models of the RC columns. The sensitivity measures suggest that the vulnerability of RC columns in two-column bents can effectively be improved by using high strength reinforcement for column confinement, reducing the spacing between confining reinforcement, and limiting the use of high strength concrete. The importance measures suggest that the random errors in the probabilistic capacity and demand models are the primary uncertainties. Thus, a closed-form fragility estimate can be obtained by considering only the uncertainties captured by the random errors. For the two example columns, only marginal difference exists between the closed-form fragility estimates and the corresponding predictive fragility estimates that include all uncertainties.

Next we introduce the fragility formulation and define the predictive fragility estimates for a column, considering both deformation and shear failure modes. This is followed by a description of the sensitivity analysis and importance measures. Closed-form fragility estimates are then proposed and compared with the corresponding predictive fragility estimates. The modified I-880 is selected as the example bridge for illustration purpose.

SENSITIVITY ANALYSIS AND IMPORTANCE MEASURES

In this section, we first conduct the sensitivity analysis for the parameters in two example RC columns. We then present the importance measures of all random variables defined in the capacity and demand models of the two example columns. In the next section, an approximate closed-form is proposed for the estimation of the fragility of RC columns. The proposed closed-form fragility simplifies the reliability analysis in engineering practice.

Sensitivity analysis

Sensitivity analysis is used to determine to which parameter(s) the reliability of a structural component is most susceptible. Let $f(\mathbf{r},\boldsymbol{\Theta}_f)$ be the joint PDF of the basic random variables in $\mathbf{r}$, where $\boldsymbol{\Theta}_f$ is a set of distribution parameters (e.g. means, standard deviations, correlation coefficients, or other parameters defining the distributions of basic random variables in $\mathbf{r}$). The solution of the reliability problem in Eq. (9) also depends on the value of $\boldsymbol{\Theta}_f$. In this application, the mean values of the basic random variables are considered as the parameters for the sensitivity analysis. The sensitivity measure for each parameter is given by computing the gradient of the reliability index, β of a RC column with respect to each parameter.

Following Hohenbichler and Rackwitz (1986), the sensitivity of β to each parameter of interest in $\boldsymbol{\Theta}_f$ is given as

$$\nabla_{\boldsymbol{\Theta}_f}\beta = \boldsymbol{\alpha}^T \cdot \mathbf{J}_{\mathbf{u}^*,\boldsymbol{\Theta}_f} \tag{16}$$

where the vector $\boldsymbol{\alpha}$ is defined as (Madsen et al. 1986)

$$\boldsymbol{\alpha} = \frac{\nabla G_{ki}}{\left\| \nabla G_{ki} \right\|}, \quad \nabla G_{ki} = \left\{ \frac{\partial G_{ki}}{\partial u_1}, \frac{\partial G_{ki}}{\partial u_2}, \cdots, \frac{\partial G_{ki}}{\partial u_m} \right\}^T \tag{17}$$

where $\nabla(\cdot)$ is the gradient function, $\|\cdot\|$ is the Euclidian norm of the given function, m is the total number of random variables in $\mathbf{z}$, here $\mathbf{z} = (\mathbf{r}, \boldsymbol{\Theta}, \boldsymbol{\varepsilon}_i)$, G_{ki} is the limit state function for mode k of failure in the $\mathbf{u}$-space defined as $G_{ki} = G_{ki}(\mathbf{u}_\mathbf{z} \,|\, \mathbf{s})$ $= G_{ki}(\mathbf{u}_\mathbf{r}, \mathbf{u}_{\boldsymbol{\Theta}} \,|\, \mathbf{s}) = g_{ki}(\mathbf{r}, \boldsymbol{\Theta}, \boldsymbol{\varepsilon}_i \,|\, \mathbf{s}) \;\; = g_{ki}(\mathbf{z} \,|\, \mathbf{s})$. Here $\mathbf{u}_\mathbf{r}$ is the standard normal random vector that corresponds to $\mathbf{r}$, $\mathbf{u}_{\boldsymbol{\Theta}}$ is the standard normal random vector that corresponds to $\boldsymbol{\Theta}$, and $\mathbf{u}_\mathbf{z} = (\mathbf{u}_\mathbf{r}, \mathbf{u}_{\boldsymbol{\Theta}})$. The last term in Eq. (16), $\mathbf{J}_{\mathbf{u}^*, \boldsymbol{\Theta}_f}$, is the Jacobian of the probability transformation from the original space $\mathbf{x}$ to the standard normal space $\mathbf{u}$ with respect to the parameters $\boldsymbol{\Theta}_f$ and computed at the most likely failure point (design point), $\mathbf{u}^*$.

In order to compare the sensitivity measures of all parameters, we define the vector, $\boldsymbol{\delta}$, as follows

$$\boldsymbol{\delta} = \boldsymbol{\sigma} \cdot \nabla_{\boldsymbol{\Theta}_f} \beta \tag{18}$$

where $\boldsymbol{\sigma}$ is the diagonal matrix with diagonal elements given by the standard deviation of each random variable in $\mathbf{r}$. Multiplying the sensitivity vector $\nabla_{\boldsymbol{\Theta}_f} \beta$ by $\boldsymbol{\sigma}$ makes each term in $\boldsymbol{\delta}$ dimensionless and makes the parameter variations proportional to the corresponding standard deviations, which are measures of the underlying uncertainties.

Column 3 in Table 7 lists the sensitivity measures for the deformation fragility to the design parameters of the northern column in Bent 8. Column 4 in Table 7 lists the

sensitivity measures for the shear fragility. The maximum positive values and the minimum negative values are in bold fonts in these two columns. In Column 3 of Table 7, it is seen that the deformation fragility is most sensitive to the means $\mathrm{E}(f_{yh})$ and $\mathrm{E}(f_c')$, where $\mathrm{E}(\cdot)$ indicates the mean of the random variable. The positive sign of the sensitivity measure for $\mathrm{E}(f_{yh})$ indicates that the random variable f_{yh} serves as a "resistance" (capacity) variable. The negative sign of the sensitivity measure of $\mathrm{E}(f_c')$ means that the random variable f_c' acts as a "load" (demand) variable. Thus, with respect to the deformation failure mode, it is desirable to design a column with confining reinforcement with high strength and limit the use of high strength concrete. From Column 4 of Table 7, random variable f_{yh} still serves as the "resistance" (capacity) variable. However, the random variable S now becomes the most important "load" (demand) variable. Thus, when designing a column for shear, it is suggested to use high strength confining reinforcement and reduce the spacing of the confining reinforcement. Similar conclusions can be made from the sensitivity measures listed in Table 8 for the northern column of Bent 11.

Fig. 10 shows the contour plots for the sensitive measure of $\mathrm{E}(f_{yh})$ for the northern columns in Bents 8 and 11. Charts (a) and (b) show the sensitivity measures for the column in Bent 8 for the deformation and shear fragility, respectively. Charts (c) and (d) show similar sensitivity measures for the column in Bent 11. From this figure, we

Table 7. Sensitivity measures for the mean of each random variable for the deformation and shear fragility estimates of the northern column in Bent 8

Parameter $\boldsymbol{\Theta}_f$	Symbol	$\boldsymbol{\sigma} \cdot \nabla_{\boldsymbol{\Theta}_f} \beta^{\dagger}$	
		Deformation	Shear
Yield stress of confining reinforcement	$E(f_{yh})$	**0.044**	**0.090**
Yield stress of longitudinal reinforcement	$E(f_y)$	0.004	–0.033
Spacing of transverse reinforcement	$E(S)$	–0.019	**–0.055**
Compressive strength of concrete	$E(f_c')$	**–0.042**	–0.020
Diameter of longitudinal reinforcement	$E(d_b)$	0.003	0.020
Gross height of column cross section††	$E(H_g)$	–0.006	–0.020
Gross width of column cross section††	$E(B_g)$	–0.013	0.003
Cover thickness of concrete	$E(Cover)$	0.000	0.000
Strength of stirrup reinforcement	$E(f_{su})$	0.000	0.000

† Sensitivity for deformation and shear fragility estimates are computed for $S_a = 1.39$ g and $PGV / PGA = 0.50$ sec.

†† The height of the column cross section is along the longitudinal direction of the bridge, the width of the columns cross section is along the transverse direction of the bridge.

Table 8. Sensitivity measures for the mean of each random variable for the deformation and shear fragility estimates of the northern column in Bent 11

Parameter $\boldsymbol{\Theta}_f$	Symbol	$\boldsymbol{\sigma} \cdot \nabla_{\boldsymbol{\Theta}_f} \beta^{\dagger}$	
		Deformation	Shear
Yield stress of confining reinforcement	$E(f_{yh})$	**0.051**	**0.107**
Yield stress of longitudinal reinforcement	$E(f_y)$	0.006	–0.043
Spacing of transverse reinforcement	$E(S)$	–0.023	**–0.063**
Compressive strength of concrete	$E(f_c')$	**–0.052**	–0.023
Diameter of longitudinal reinforcement	$E(d_b)$	0.004	0.026
Gross height of column cross section††	$E(H_g)$	–0.007	–0.024
Gross width of column cross section††	$E(B_g)$	–0.016	0.002
Cover thickness of concrete	$E(cover)$	0.000	0.000
Strength of stirrup reinforcement	$E(f_{su})$	0.000	0.000

† Sensitivity for deformation and shear fragility estimates are computed for $S_a = 1.39$ g and $PGV / PGA = 0.50$ sec.

†† The height of the column cross section is along the longitudinal direction of the bridge, the width of the columns cross section is along the transverse direction of the bridge.

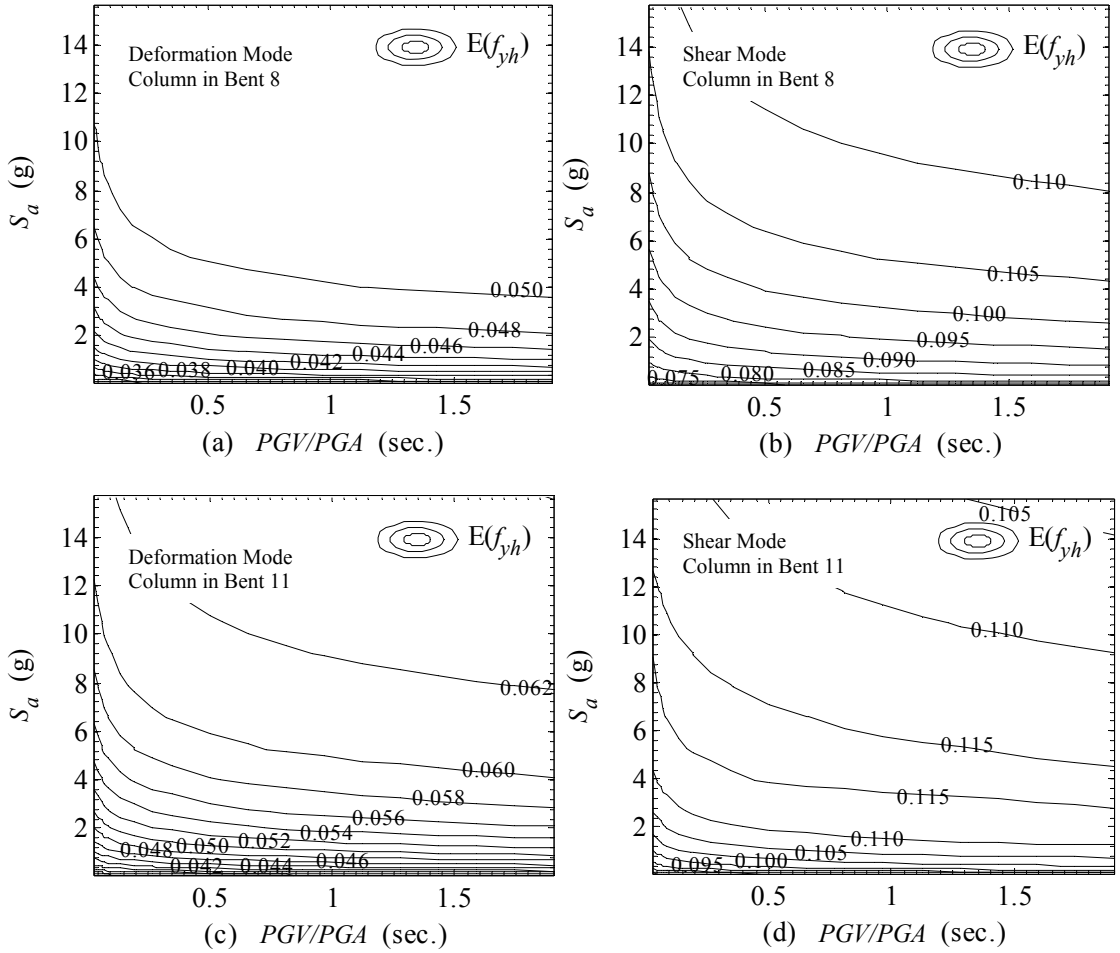

Fig. 10. Sensitivity contours for $E(f_{yh})$ for deformation fragility and shear fragility for the northern columns in Bent 8 and in Bent 11

can see the sensitivity measure of $E(f_{yh})$ varies with S_a and PGV/PGA. This function is more susceptible to the changes in S_a than to the changes in PGV/PGA.

Fig. 11 shows sensitivity measures as a function of S_a or PGV/PGA. Chart (a) shows the sensitivity curves of parameters in the deformation limit state for the column

in Bent 8. Each curve is a function of S_a given PGV/PGA =0.50 sec. Chart (b) shows the corresponding sensitivity curves for parameters in the shear limit state. Chart (c) shows the sensitivity curves of parameters for the deformation limit state for the same column

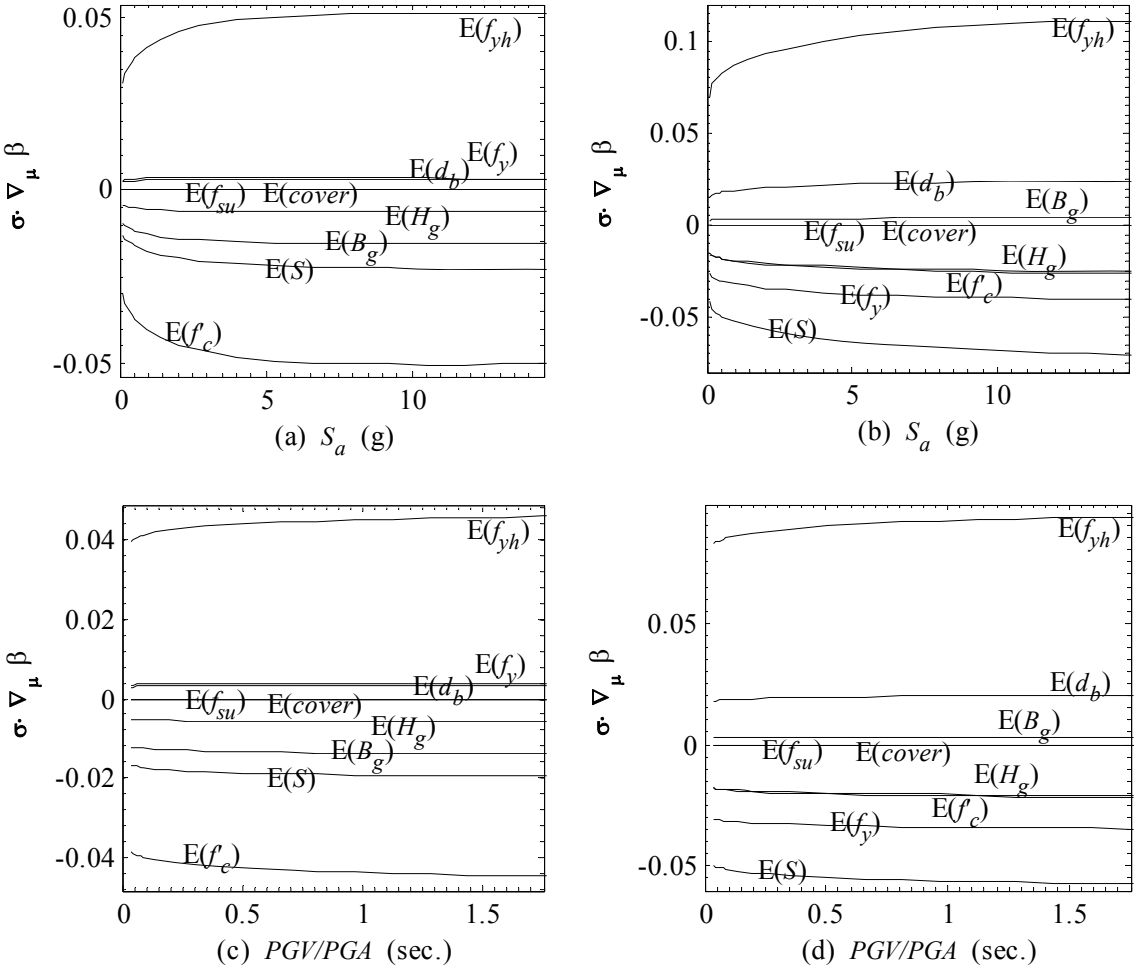

Fig. 11. Sensitivity curves for deformation fragility estimates in charts (a) and (c) and shear fragility estimates in charts (b) and (d) for northern column in Bent 8. Charts (a) and (b) are plotted at PGV/PGA =0.50 sec.; charts (b) and (d) are plotted at S_a=1.39 g

as a function of PGV/PGA given S_a=1.39 g. Chart (d) shows the corresponding sensitivity curves for parameters in the shear limit state.

Importance measures

According to Eq. (9), the limit state function is defined by the probabilistic capacity and demand models of the column. Each random variable has a different contribution to the variability of the limit state function. Important random variables have a larger effect on the variability of the limit state function than less important random variables. By considering only the uncertainties from the important random variables, the reliability problem can be simplified for engineering practice.

Following FORM, the first order approximation of the limit state function $g_{ki}(\mathbf{z}\,|\,\mathbf{s})$ at the design point $\mathbf{z}^*$ is

$$g_{ki}\left(\mathbf{z}\,|\,\mathbf{s}\right) \approx g_{ki}\left(\mathbf{z}^*|\,\mathbf{s}\right) + \nabla g_{ki}\left(\mathbf{z}^*|\,\mathbf{s}\right)\left(\mathbf{z}-\mathbf{z}^*\right) \tag{19}$$

where $g_{ki}(\mathbf{z}^*|\,\mathbf{s})$ is the value of the limit state function evaluated at $\mathbf{z}^*$, $\mathbf{z}^*$ is the design point in the original space, $\nabla g_{ki}(\mathbf{z}^*|\,\mathbf{s})$ is the gradient of $g_{ki}(\mathbf{z}\,|\,\mathbf{s})$ evaluated at $\mathbf{z}^*$. By denoting $\mathbf{z} = \{z_1, z_2, ..., z_m\}^T$, the variance of $g_{ki}(\mathbf{z})$ at $\mathbf{z}^*$ is given as

$$\begin{aligned} \mathrm{Var}\left[\, g_{ki}\left(\mathbf{z}\,|\,\mathbf{s}\right)\right]\Big|_{\mathbf{z}=\mathbf{z}^*} &\approx \nabla g_{ki}\left(\mathbf{z}^*|\,\mathbf{s}\right)\cdot\Sigma_{\mathbf{zz}}\cdot\left[\nabla g_{ki}\left(\mathbf{z}^*|\,\mathbf{s}\right)\right]^T \\ &= \sum_{j=1}^{m}\left(\sigma_j\cdot\left.\frac{\partial g_{ki}}{\partial z_j}\right|_{\mathbf{z}=\mathbf{z}^*}\right)^2 + \sum_{j=1}^{m}\sum_{\substack{l=1\\ l\neq j}}^{m}\left(\left.\frac{\partial g_{ki}}{\partial z_j}\right|_{\mathbf{z}=\mathbf{z}^*}\cdot\left.\frac{\partial g_{ki}}{\partial z_l}\right|_{\mathbf{z}=\mathbf{z}^*}\cdot\sigma_j\cdot\sigma_l\cdot\rho_{jl}\right) \end{aligned} \tag{20}$$

where $\Sigma_{\mathbf{zz}}$ is the covariance matrix of all random variables in $\mathbf{z}$, σ_j and σ_l ($j,l=1,2,\cdots,m$) are the standard deviations of the j^{th} and l^{th} random variable in $\mathbf{z}$ with correlation coefficient ρ_{jl}. From the first summation term in Eq. (20), we can see that different random variables have different contributions on the variance of the limit state function, $\mathrm{Var}[g_{ki}(\mathbf{z}\,|\,\mathbf{s})]$. Thus, they are not of equal importance. Following Der Kiureghian and Ke (1995), a measure of importance $\boldsymbol{\gamma}$ can be defined as

$$\boldsymbol{\gamma}^T = \frac{\boldsymbol{\alpha}^T \cdot \mathbf{J}_{\mathbf{u}^*,\mathbf{z}^*} \cdot \mathbf{SD}'}{\left\| \boldsymbol{\alpha}^T \cdot \mathbf{J}_{\mathbf{u}^*,\mathbf{z}^*} \cdot \mathbf{SD}' \right\|} \tag{21}$$

where $\mathbf{SD}'$ is the standard deviation diagonal matrix of equivalent normal variables $\mathbf{z}'$, defined by the linearized inverse transformation $\mathbf{z}' = \mathbf{z}^* + \mathbf{J}_{\mathbf{z}^*,\mathbf{u}^*} \cdot (\mathbf{u} - \mathbf{u}^*)$ at the design point. Each element in $\mathbf{SD}'$ is the square root of the corresponding diagonal element of the covariance matrix $\boldsymbol{\Sigma}' = \mathbf{J}_{\mathbf{z}^*,\mathbf{u}^*} \cdot \mathbf{J}^{\mathbf{T}}_{\mathbf{z}^*,\mathbf{u}^*}$ of the variables in $\mathbf{z}'$.

In Table 9, Column 3 lists the importance measures of the random variables for the deformation fragility of the northern column in Bent 8. We can see that the random errors $\varepsilon_{C\delta}$ and $\varepsilon_{D\delta}$ are the most important variables. Column 5 lists the importance measures of the random variables for shear fragility. In this case, random variables θ_{Dv1} and θ_{Dv2} have the highest importance measures. Similar conclusions are valid for the importance measures for the northern column of Bent 11 (Table 10).

For both the deformation and shear mode of failure, the random variables in the $\mathbf{u}$-space that correspond to ε_{Ck} and ε_{Dk} ($k=\delta,v$) are the most important. The correla-

Table 9. The importance measures for each random variable for the deformation and shear fragility estimates of the northern column in Bent 8

Random variables	γ †			
	Symbol	Deformation	Symbol	Shear
Random error for capacity model	$\varepsilon_{C\delta}$	**–0.622**	ε_{Cv}	–0.274
Random error for demand model	$\varepsilon_{D\delta}$	**0.596**	ε_{Dv}	0.368
Parameters in the capacity model	$\theta_{C\delta 1}$	–0.160	θ_{Cv2}	–0.020
	$\theta_{C\delta 7}$	–0.053	θ_{Cv4}	–0.053
	$\theta_{C\delta 11}$	0.042		
Parameters in the demand model	$\theta_{D\delta 1}$	0.318	θ_{Dv1}	**0.642**
	$\theta_{D\delta 2}$	–0.274	θ_{Dv2}	**0.560**
	$\theta_{D\delta 3}$	0.022	θ_{Dv3}	–0.155
	$\theta_{D\delta 4}$	–0.015	θ_{Dv4}	0.012
	$\theta_{D\delta 5}$	0.021	θ_{Dv5}	–0.009
			θ_{Dv6}	0.015
Mean capacity model error	$\sigma_{C\delta}$	0.111	σ_{Cv}	0.053
Mean demand model error	$\sigma_{D\delta}$	0.190	σ_{Dv}	0.171
Yield stress of confining reinforcement	f_{yh}	–0.039	f_{yh}	–0.044
Yield stress of longitudinal reinforcement	f_y	–0.003	f_y	0.017
Spacing of transverse reinforcement	S	0.017	s	0.027
Compressive strength of concrete	f_c'	0.038	f_c'	0.010
Diameter of longitudinal reinforcement	d_b	–0.003	d_b	–0.010
Gross height of column cross section††	H_g	0.005	H_g	0.010
Gross width of column cross section††	B_g	0.012	B_g	–0.002
Cover thickness of concrete	Cover	0.000	Cover	0.000
Strength of stirrup reinforcement	f_{su}	0.000	f_{su}	0.000

† Importance for deformation and shear fragility estimates are computed for $S_a = 1.39$ g and PGV/PGA $= 0.50$ sec.

†† The height of the column cross section is along the longitudinal direction of the bridge, the width of the columns cross section is along the transverse direction of the bridge.

Table 10. The importance measures for each random variable for the deformation and shear fragility estimates of the northern column in Bent 11

Random variables	$\boldsymbol{\gamma}$ †			
	Symbol	Deformation	Symbol	Shear
Random error for capacity model	$\varepsilon_{C\delta}$	**–0.615**	ε_{Cv}	–0.272
Random error for demand model	$\varepsilon_{D\delta}$	**0.602**	ε_{Dv}	0.321
Parameters in the capacity model	$\theta_{C\delta 1}$	–0.157	θ_{Cv2}	–0.023
	$\theta_{C\delta 7}$	–0.066	θ_{Cv4}	–0.061
	$\theta_{C\delta 11}$	0.021		
Parameters in the demand model	$\theta_{D\delta 1}$	0.312	θ_{Dv1}	**0.655**
	$\theta_{D\delta 2}$	–0.248	θ_{Dv2}	**0.594**
	$\theta_{D\delta 3}$	0.022	θ_{Dv3}	–0.145
	$\theta_{D\delta 4}$	–0.063	θ_{Dv4}	0.012
	$\theta_{D\delta 5}$	0.031	θ_{Dv5}	–0.037
			θ_{Dv6}	0.024
Mean capacity model error	$\sigma_{C\delta}$	0.123	σ_{Cv}	0.033
Mean demand model error	$\sigma_{D\delta}$	0.215	σ_{Dv}	0.094
Yielding stress of confining reinforcement	f_{yh}	–0.045	f_{yh}	–0.047
Yielding stress of longitudinal reinforcement	f_y	–0.005	f_y	0.019
Spacing of transverse reinforcement	S	0.021	s	0.028
Compressive strength of concrete	f_c'	0.047	f_c'	0.010
Diameter of longitudinal reinforcement	d_b	–0.004	d_b	–0.011
Gross height of column cross section††	H_g	0.006	H_g	0.011
Gross width of column cross section††	B_g	0.015	B_g	–0.001
Cover thickness of concrete	Cover	0.000	Cover	–0.000
Strength of stirrup reinforcement	f_{su}	0.000	f_{su}	0.000

† Importance for deformation and shear fragility estimates are computed for $S_a = 1.39$ g and PGV/PGA $= 0.50$ sec.

†† The height of the column cross section is along the longitudinal direction of the bridge, the width of the columns cross section is along the transverse direction of the bridge.

tion structure between the random variables in the deformation limit state does not change the importance of $\varepsilon_{C\delta}$ and $\varepsilon_{D\delta}$ in the original space. However, the correlation

structure between the random variables in the shear limit state changes the importance of ε_{Cv} and ε_{Dv}. As a result, θ_{Dv1} and θ_{Dv2} turn out to be the two most important random variables in the original space. The next two most important random variables for the shear mode of failure are again ε_{Cv} and ε_{Dv}.

Fig. 12 shows the contour plots of the importance of $\varepsilon_{C\delta}$, $\varepsilon_{D\delta}$, ε_{Cv}, ε_{Dv}, θ_{Dv1}, and θ_{Dv2}. From this figure, one can see that the importance measures are also a function of S_a and PGV/PGA. As for the sensitivity measures, the importance measures of random variables are more susceptible to the changes in S_a than in PGV/PGA.

Fig. 13 shows the curves of the importance measures of all random variables for the northern column in Bent 8. Each curve in this figure is a function of S_a given PGV/PGA =0.50 sec. Chart (a) shows the importance measures for the deformation fragility. Chart (b) shows them for the shear fragility. The plots on the right show zoomed-in plots for smaller values of γ. One interesting observation in chart (a) is that the importance measures of $\sigma_{C\delta}$ vary from positive values to negative values as the values of S_a increases. Therefore, there is a value of S_a for which the contribution of $\sigma_{C\delta}$ to $\mathrm{Var}[g_{ki}(\mathbf{z}\,|\,\mathbf{s})]$ is zero. The same considerations can be made for $\sigma_{D\delta}$.

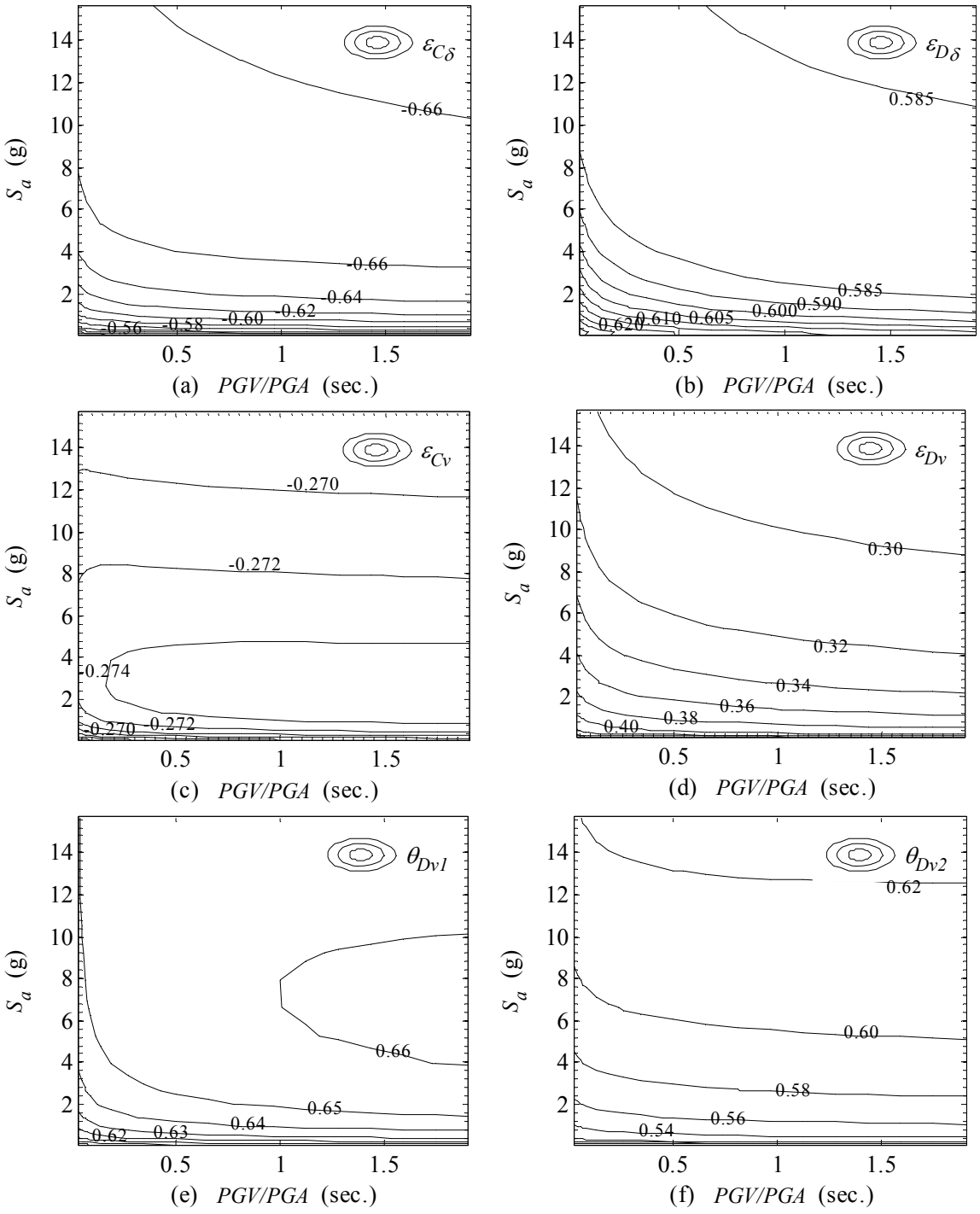

Fig. 12. Contour plots of the importance of selected random variables for the deformation (a and b) and shear fragility (c-f) for the northern column in Bent 8

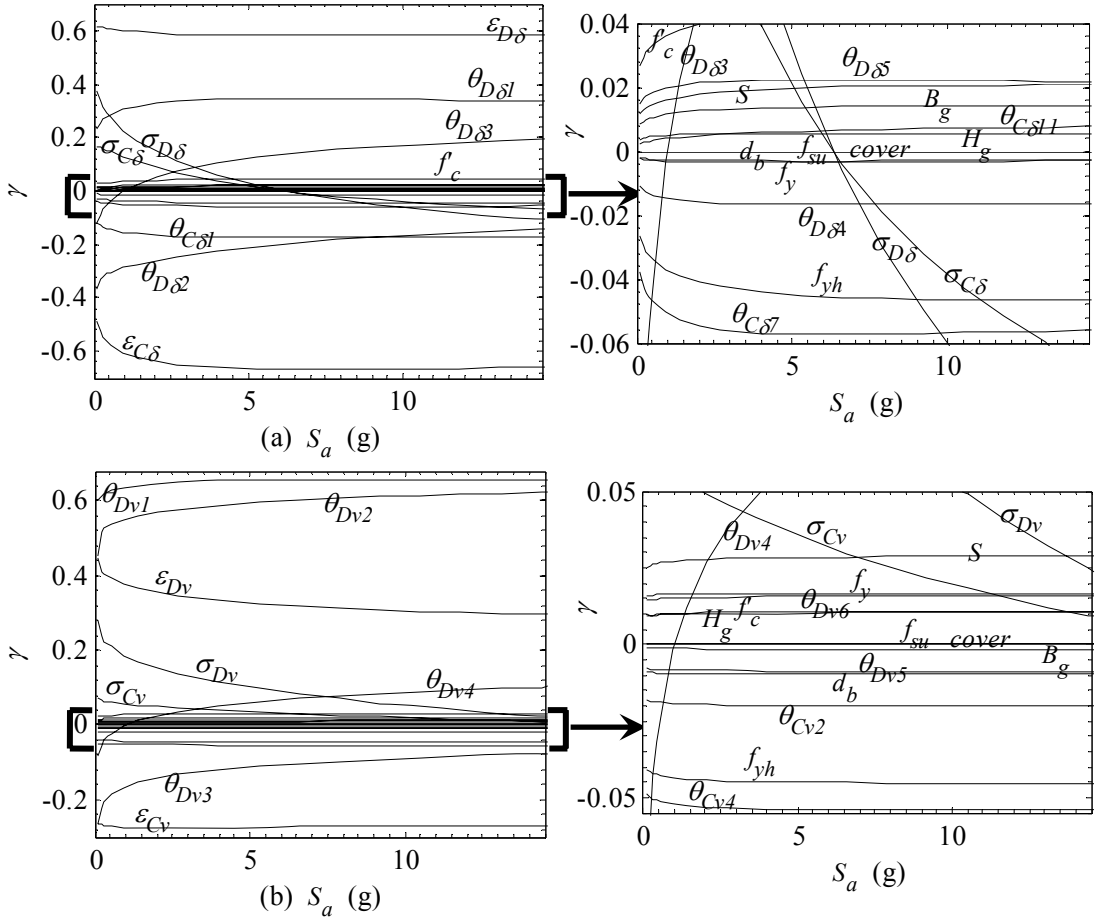

Fig. 13. Importance measure curves for (a) deformation and (b) shear fragility estimates for the northern column in Bent 8 for PGV/PGA =0.50 sec.

Fig. 14 shows the importance measures as a function of PGV/PGA for the northern column in Bent 8 given S_a=1.39 g. The changes in the importance measures indicate that the contribution from each random variable varies also with PGV/PGA. However, similar to what was observed based on the contour plots, the dependency on PGV/PGA is less pronounced than for S_a.

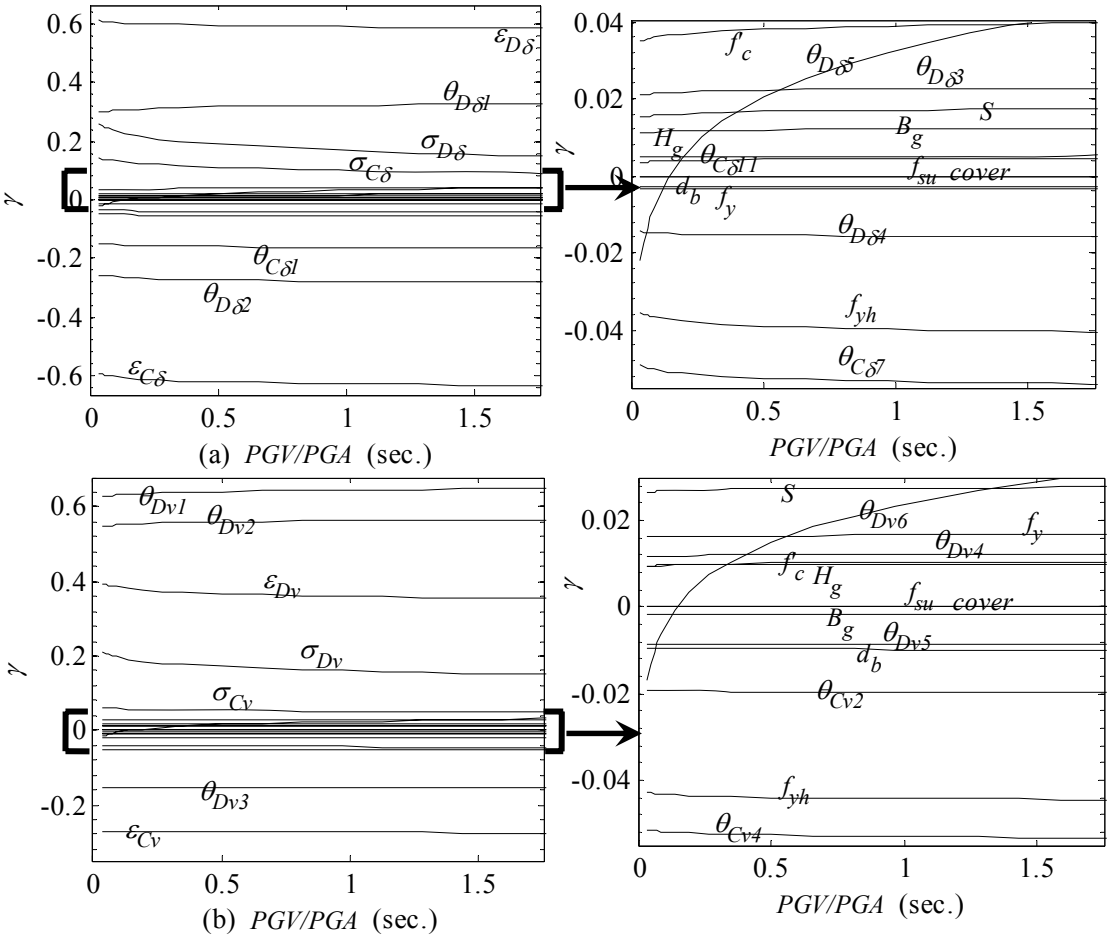

Fig. 14. Importance measure curves for (a) deformation and (b) shear fragility estimates for the northern column in Bent 8 for S_a=1.39 g

APPROXIMATE CLOSED-FORM FRAGILITY ESTIMATES

In this section, we suggest an approximate closed-form solution for the fragility of a RC column that does not require any specialized reliability software and has no significant loss of accuracy. The closed-form solution is obtained by considering only the uncertainties from the important random variables and disregarding the uncertainties in

the less important ones.

For the deformation models, only $\varepsilon_{C\delta}$ and $\varepsilon_{D\delta}$ are considered as random. For the shear models, while θ_{Dv1} and θ_{Dv2} are the most important random variables, they only represent statistical uncertainties in the seismic demand. So, in this case we select the next two most important random variables for the shear mode of failure that are ε_{Cv} and ε_{Dv}, which capture the overall model uncertainties. An approximate closed-form estimate of Eq. (11) is obtained by ignoring the uncertainties in $\boldsymbol{\Theta}$ and $\mathbf{r}$, and using a point estimate $\hat{\boldsymbol{\Theta}}$ and $\hat{\mathbf{r}}$ (e.g., the posterior means). The corresponding point estimate of the fragility in Eq. (11) is written as

$$\begin{aligned}\hat{F}(\mathbf{s}) &= \mathrm{P}\left[g_{ki}\left(\hat{\mathbf{r}}, \hat{\boldsymbol{\Theta}}, \boldsymbol{\varepsilon}_i \middle| \mathbf{s}\right) \le 0 \right] \\ &= \mathrm{P}\left[C_{ki}\left(\hat{\mathbf{r}}, \hat{\boldsymbol{\Theta}}_C, \boldsymbol{\varepsilon}_{Ci}\right) - D_{ki}\left(\hat{\mathbf{r}}, \hat{\boldsymbol{\Theta}}_D, \boldsymbol{\varepsilon}_{Di} \middle| \mathbf{s}\right) \le 0 \right] \\ &= \Phi\left(-\frac{\mu_{C_{ki}} - \mu_{D_{ki}}}{\sqrt{\hat{\sigma}_{Cki} + \hat{\sigma}_{Dki}}} \right) = 1 - \Phi\left(\frac{\mu_{C_{ki}} - \mu_{D_{ki}}}{\sqrt{\hat{\sigma}_{Cki} + \hat{\sigma}_{Dki}}} \right) \qquad i = 1,..,s;\ k = \delta, v\end{aligned} \tag{22}$$

The approximate-closed form solution in Eq. (22) can also be used to compute the fragility for the series system problem defined in Eq. (15). In this case, $\hat{F}(\mathbf{s})$ can be computed in terms of the joint normal probability distribution of $\boldsymbol{\varepsilon}_i$ ($i = 1,..,2s$).

Fig. 15 (a) shows the contours of the deformation fragility estimates for the northern column in Bent 8; chart (b) shows the contours of the shear fragility estimates for the same column. The solid lines denote the closed-form fragility estimates from Eq. (22) and the dotted-lines denote the predictive fragility estimates from Eq. (10). Here

FORM is used for the predictive fragility estimation. From this figure, we can see that only a marginal difference exists between the closed-form and the corresponding predictive fragility. This is true for both deformation and shear fragility estimates. Similar conclusions can be made for the northern column in Bent 11 (Fig. 16), which is more susceptible to shear failure than the column in Bent 8 due to the different slenderness ratio of the column. We can also see from the shear fragility plots in Fig. 15 or Fig. 16 that, although we considered ε_{Cv} and ε_{Dv} instead of θ_{Dv1} and θ_{Dv2} as random, the closed-form shear fragility estimates are still only marginally different from the predictive estimates of the fragility.

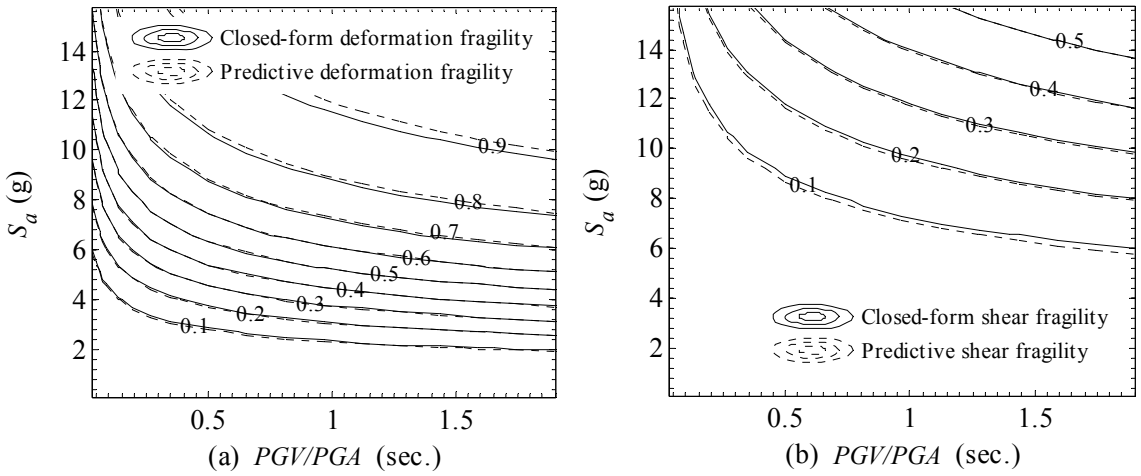

Fig. 15. Contour plots of predictive and closed-form deformation fragility estimates (a) and shear fragility estimates (b) for the northern column in Bent 8

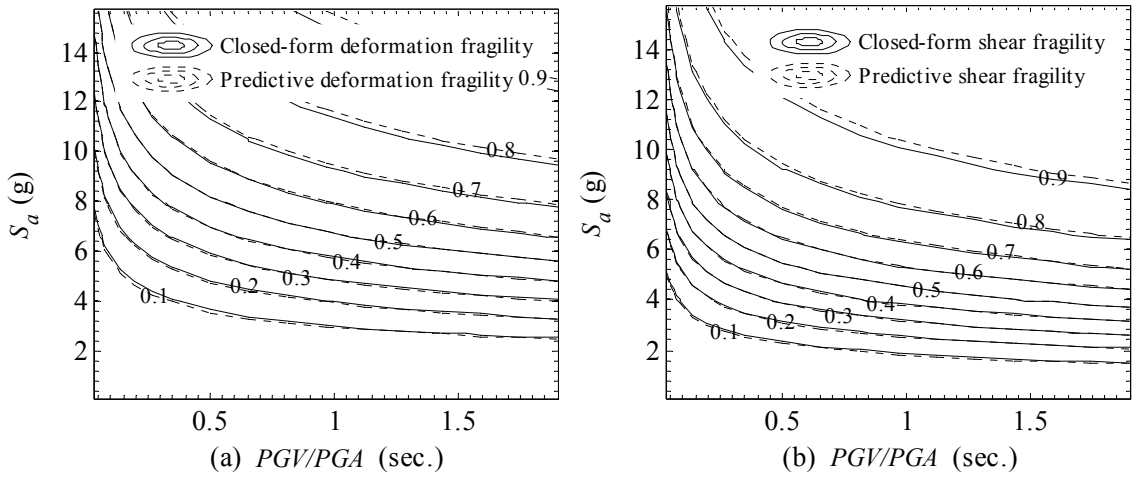

Fig. 16. Contour plots of predictive and closed-form deformation fragility estimates (a) and shear fragility estimates (b) for the northern column in Bent 11

SUMMARY

A closed-form solution is developed for the shear and deformation fragility of RC columns in bridges with two-column bents. The closed-form solution is constructed using probabilistic capacity and demand models and incorporates the dominant uncertainties.

A sensitivity analysis is conducted for the parameters in the limit state function of the RC columns. The sensitivity measures suggest that the vulnerability of RC columns in two-column bents can effectively be improved by using high strength reinforcement for the column confinement. It is also suggested to avoid using high strength concrete and large spacing between confining reinforcement.

Importance measures are also computed for the random variables in the fragility estimation. Importance measures serve as a guide to identify the most relevant sources of uncertainties. By incorporating only the uncertainties from the important random variables, the computation of the fragility of a RC column is simplified, leading to a closed-form solution that does not require any reliability software, and hence, is more easily implementable in engineering practice and design. The proposed closed-form fragility estimates closely approximate the corresponding predictive estimates of the fragility. Hence, they can be used with no significant loss of accuracy.

CHAPTER IV

STIFFNESS DEGRADATION AND TIME TO CRACKING OF COVER CONCRETE IN RC STRUCTURES SUBJECT TO CORROSION

Due to the ingression of corrosive agents, the corrosion process will be initiated when sufficient amount of corrosive agents accumulate on the surface of reinforcing steel. The concrete cover for corroded reinforcing steel is subject to corrosion pressure resulted from the rust product and will crack shortly after the corrosion initiation. This Chapter proposes a stiffness degradation factor to model the stiffness degradation and the time to cracking of concrete cover since corrosion initiation. The corrosion effects from the degraded concrete covers and the loss of reinforcing steel on the fragility estimation will be considered in the next Chapter.

INTRODUCTION

Corrosion in reinforcing steel is as an important deterioration mechanism that reduces the service life of RC structures exposed to corrosive environments. This deterioration in RC structures is due to the loss of reinforcing steel and the corrosion-induced cracks in concrete cover. The deterioration process of reinforcing steel in RC structures can be divided into three phases (Cady and Weyers 1983): 1) the diffusion of corrosive agents onto the surface of reinforcing steel before corrosion initiates; 2) the corrosion-induced cracking process in the concrete cover before the crack front reaches the surface of the RC structure; and 3) the continued deterioration of the cross-section of the RC structure

before repair or rehabilitation procedures are carried out. During the last two phases, the corroded structures are usually subject to stiffness degradation because of the cracking process.

The degradation of the stiffness of corroded RC structures is closely related to the loss of reinforcing steel associated to corrosion (Torres-Acosta et al. 2004; Tastani and Pantazopoulou 2005; Vidal et al. 2007; Choe et al. 2008a, b; Cairns et al. 2008; Capozucca 2008). A number of methodologies have been proposed to model the stiffness degradation based on the bond stress-slip mechanism (e.g., Floegl and Mang 1982; Wu et al. 1992; Tastani and Pantazopoulou 2005). Some effort has been made to model the tension-stiffening of the flexural concrete between cracks (e.g., Scanlon 1975; Bažant and Oh 1984; Torres et al. 2004). However, limited attention has been paid to the cracking progress itself and the corresponding stiffness degradation. In particular, the effects of the corrosion-induced cracks in concrete cover on the stiffness of corroded RC structures have not been properly considered.

Another physical quantity of interest is the time to cracking of the concrete cover, which is defined as the time elapsed from the corrosion initiation to the instant the crack front reaches the surface of the concrete cover. The time to cracking is valuable to estimate the service life of a RC structure. Among the existing studies (e.g. Liu and Weyers 1998; Pantazopoulou and Popaouli 2001; Bhargava et al. 2006; Li et al. 2006), the smeared crack model has been commonly applied to the concrete cover to predict the time to cracking by assuming the cracks grow axis-symmetrically. However, applications of the smeared crack model in RC structures require relatively strict

assumptions that might not be actually satisfied in a typical cross section of RC structures. In fact, it is more likely that in the actual RC structures subject to corrosion individual cracks in the concrete cover propagate in different ways.

This chapter presents the models for the cracking process and the corresponding stiffness degradation in the cracked concrete due to the corrosion in the reinforcement steel using the energy principle (Zhong et al. 2008d). In particular, a cohesive crack model is applied to simulate the cracking process in the concrete cover. The total complimentary energy of a cracked structure consists of the complimentary strain energy of the cracked structure and the complimentary surface energy of the cohesive cracks modeled in the cracked structure (Bažant and Li 1995). By applying the variation principle to the total complimentary energy, the crack depth, the cohesive stress, and the corrosion pressure are found simultaneously, provided a displacement of the rust front resulted from the density difference between the rust product and the depleted steel. The degraded stiffness of the cover concrete can be represented as the secant stiffness (Bažant and Planas 1998) of the cracked concrete. A stiffness degradation factor, defined as the ratio between the secant and the initial stiffness, is then proposed to represent the stiffness degradation caused by the cracking process in the concrete cover. The time to cracking of the concrete cover is found by determining the time needed by the crack front to reach the surface of concrete cover starting from the time to corrosion initiation.

This chapter includes four sections. First, we introduce the process of corrosion-induced cracking in RC structure. Second, we briefly review the available models for

the corrosion-induced cracking and the time to cracking and the pertinent limitations. Then, based on the energy principle, we propose a new method to assess the stiffness degradation of a cracked concrete cover and to determine the time to cracking. Finally, two examples are used to illustrate the computation of the stiffness degradation of a cracked concrete cover and the time to cracking for two specimens for which test results are available.

CRACK PROPAGATION IN RC STRUCTURES DUE TO CORROSION

The concrete cover is used in RC structures to protect reinforcing steel against corrosive agents, such as chlorides, moisture, seawater, deicing salts, oxygen, carbon dioxide, sulfates, acids, etc. High quality concrete with appropriate mixture proportion, compacting, and curing condition provides good protection for the reinforcing steel. Such protection results from the physical barrier of the concrete cover and the chemical barrier of the alkaline pore solution existing in the cover concrete. Due to the presence of a highly alkaline pore solution, the initial corrosion product creates a layer of passive film on the surface of the reinforcing steel (Liu 1996).

However, due to the capillary of the concrete, in an aggressive environment, the water-soluble corrosive agents can breach onto the surface of the reinforcing steel through the concrete cover. The diffusion process also plays an important role for the ingression of corrosive agents (Liu 1996). The chloride ions, if available in sufficient quantity, can break the passive film and initiate corrosion (mainly pitting corrosion). Once initiated, the chloride ions act as a catalyst for the corrosion propagation. In addition, carbonate from the atmosphere diffuses towards the steel surface and reduces

the pH value of the concrete pore solution around the surface of the reinforcing steel. This results in the breaking of the passive film and the initiation and propagation of corrosion (mainly general corrosion).

The corrosion in reinforcing steel results in cracking of the concrete cover. This is due to the increased volume of the rust product compared to that of the depleted steel. The cracking mouth opening displacement (CMOD) of the propagating crack increases as the tensile stress in the cracked concrete decreases along the softening branch of the stress-strain curve of the concrete (Bažant and Planas 1998), as shown in Fig. 17. The left chart shows the stress-strain curve for concrete subject to tensile stress. Here, $\phi(\cdot)$ is

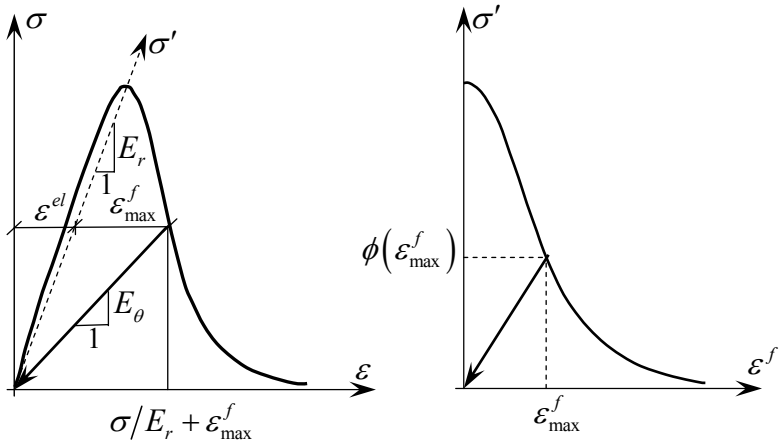

Fig. 17. Typical stress-strain softening curve for concrete subject to tensile stress

the function for the softening stress-strain curve, E_r is the initial stiffness of the intact concrete, E_θ is the secant stiffness of cracked concrete and decreases with the cracking

process, ε^{el} is the elastic strain, and $\varepsilon^{f}_{\max}$ is the maximum cracking strain before unloading. The right chart shows the softening curve extracted from the right branch of the stress-strain curve shown in the left chart. Note the abscissa is now the strain from the cracking opening, ε^{f}, which is the actual cracking stain during unloading. The ordinate is the corresponding stress σ' on the softening curve. As a result, the corrosion-induced cracking process weakens the stiffness of the cover concrete. To represent the deterioration in stiffness, a stiffness degradation factor, η, is defined as the ratio between the secant stiffness and the initial stiffness, i.e., $\eta = E_{\theta} / E_{r}$. Ultimately, the cracks reach the surface of corroded RC structure and excessively wide cracks indicate that the serviceability limit state of the RC structure has been reached.

CURRENT MODELS FOR CORROSION-INDUCED CRACKING

Many approaches have been proposed to model the corrosion-induced cracking in concrete cover. These include analytical models (e.g., Bažant 1979a,b; Melchers 2003), empirical approaches (e.g., Morinaga 1988; Liu and Weyers 1998; Torres-Acosta 1999; Vu et al. 2005), and numerical solutions (e.g., Pantazopoulou and Papoulia 2001; Leung 2001; Tastani and Pantazopoulou 2005; Li et al. 2006; Bhargava et al. 2006; Maaddawy and Soudki 2007). In particular, for the numerical solutions, a smeared crack model has been combined with the finite element method (FEM) to model the cracking process (e.g., Molina et al. 1993; Padovan and Jae 1997; Ahmed et al. 2007) and linear elastic fracture mechanics have also been combined with various numerical methods to predict the crack propagation (e.g., Padovan and Jae 1997; Noghabai 1999; Ohtsu and Yosimura 1997; Uddin et al. 2004).

In the current literature, the method used to model the corrosion-induced cracking is closely related to the geometry of the concrete cover subject to the volumetric expansion of the rust product. The geometry of the concrete considered in the literature can be classified into three categories: 1) an infinite medium with a circular hole, 2) the actual geometry used in the cross section of a RC structure, and 3) a concrete cylinder concentric with the corroding reinforcing steel.

In case of the infinite medium, the corrosion pressure generates cracks that emanate radially from the hole occupied by the reinforcing steel. Therefore, models can be derived based on fracture mechanics. For example, considering the constraining effect of the surface of the reinforcing steel on the crack opening, Leung (1997, 2001) correlated the crack depth with the corrosion pressure through a compliance function and developed a stress intensity factor (SIF) for the bonded interface between the reinforcing steel and the concrete. However, although this method is theoretically appealing, modeling the concrete cover as an infinite medium is not physically appropriate at least for most civil engineering applications.

For the case in which the actual complex geometry of the RC structure is modeled, the boundary element method (BEM) has been combined with fracture mechanics to find the displacement and stress fields of the cracked concrete (e.g., Ohtsu and Yosimura 1997; Aliabadi 1997; Aliabadi and Saleh 2002; Uddin et al. 2004.). The main advantage of BEM is its ability to reduce the dimension of the problem in modeling the cracking process (Aliabadi 1997). FEM has also been applied to the complex geometry and the changing boundary conditions due to crack propagation (e.g.,

Ingraffea et al. 1984; Rots 1988; Molina et al. 1993; Klisinski et al. 1991; Padovan and Guo 1994; Guo and Padovan 1994; Ahmed et al. 2007). While BEM or FEM have the flexibility required to model complex shapes, a significant effort is required for their numerical implementation.

Finally, a concrete cylinder has been commonly used because a cylindrical geometry has well-defined strain and stress analytical solutions for given boundary conditions (Noghabai 1999). Therefore, many studies of the corrosion effect prefer using the cylindrical geometry to model the concrete cover (e.g., Liu and Weyers 1998; Noghabai 1999; Pantazopoulou and Papoulia 2001; Tastani and Pantazopoulou 2005; Li et al. 2006; Zhao and Jin 2006; Bhargava et al. 2006). However, a concrete cylinder concentric with the reinforcing steel does not fully represent the actual boundary conditions in the structures subject to corrosion (Vu et al. 2005).

A simplified solution that can capture the major effects of corrosion on the concrete and can provide insights into the underlying physics of the complex phenomena is needed. In the next section we propose a new method to assess the stiffness degradation of a cracked concrete cover and to determine the time to cracking. In the following of this section, we review some details of the current models that are needed for the proposed model.

Based on the experiments in a five-year test study, Liu and Weyers (1998) presented an empirical formula for the time to cracking defined as a function of the critical amount of corrosion products and the rate of rust production, which is closely related to the corrosion rate. The critical amount of corrosion products depends on the

diameter of the corroding rebar, the density of the rust product, and the content of the rust product. While this empirical formula is developed based only on data from a limited number of specimens and therefore cannot claim a general validity, the experimental values from Liu and Weyers (1998) are used here to validate the proposed formulation.

Pantazopoulou and Papoulia (2001) and Li et al. (2006) suggested using partial differential equations (PDE) to model the displacement and stress fields in the concrete cover. In their model, the concrete cover is partitioned into two concentric cylinders: an inner cracked cylinder and an outer intact cylinder, where the smeared crack model is used for the cracked concrete. The displacement boundary condition adopted by Pantazopoulou and Papoulia (2001) for the inner wall of the cracked cylinder is

$$u\left(r_{inner},t\right)=d\left(t\right)-\left[r_{inner}-R_{rb}\left(t\right)\right] \tag{23}$$

while Li et al. (2006) used

$$u\left(r_{inner},t\right)=d\left(t\right) \tag{24}$$

where $u(r,t)$ is the radial displacement of the cylinder at a radius r measured from the center of the cylinders at time t, r_{inner} is the original radius of the reinforcing steel, $d(t)$ is the thickness of the rust product as a function of the density of the corrosion current, $R_{rb}(t)$ is the reduced radius of the reinforcing steel at time t, and $r_{inner}-R_{rb}(t)$ is the corrosion penetration into the reinforcing steel.

For an explicit solution of $u(r,t)$, Li et al. (2006) proposed a formulation to compute the stiffness degradation factor, $\eta(t)$

$$\eta(t) = \frac{\phi\left[\overline{\varepsilon}_\theta(t)\right]}{E_r \overline{\varepsilon}_\theta(t)} \tag{25}$$

for the governing equation for the cracked cylinder, where $\overline{\varepsilon}_\theta(t)$ is the averaged tangential strain over the cracked surface at time t.

Although the mathematical formulations in Pantazopoulou and Papoulia (2001) and Li et al. (2006) are simple, the underlining assumptions of smeared-crack propagation in the concrete cylinder is not appropriate since in most engineering structures the corrosion-induced cracks seldom propagate in an axis-symmetric way. Secondly, the governing PDE does not necessarily capture the fundamental behavior of a fractured structure, e.g., the change of energy in a fracturing structure. Finally, Eq. (25) does not provide accurate estimates. In fact, in the model proposed by Li et al. (2006), the average strain across the cracked and intact cylinders were used to define the stiffness degradation factor, $\eta(t)$. However, the stiffness degradation of cracked concrete is more closely correlated to the maximum strain.

PROPOSED MODEL BASED ON THE ENERGY PRINCIPLE

In this section, we propose a new approach to estimate the secant stiffness of a cracked concrete cover subject to corrosion pressure and the time to cracking. The cracks in the concrete cover are assumed to be cohesive cracks. The cohesive crack model (e.g., Barenblatt 1962; Hillerborg et al. 1976) lumps the fracture process zone around the crack front onto the crack line and uses the softening law of cracked concrete to characterize the stress-strain relationship on the crack surface (Bažant and Planas 1998).

In the following, we compute the stiffness degradation factor based on the variation principle applied to the complementary energy of the cracked RC structure.

The total complementary energy of the cracked structure consists of the complementary strain energy, U^*, of the cracked RC structure and the complementary surface energy, Π_c^*, of the crack surfaces in the RC structure. Thus, the total complementary energy, Π^*, for a cracked structure is

$$\Pi^* = U^* + \Pi_c^* \tag{26}$$

To apply the energy principle to the fracturing RC structure, we consider a portion of the concrete cover with unit thickness and initial notch with normalized depth α_0, subject to a given load-point deformation, $u(r_{inner}, t)$, caused by the corrosion pressure, $P(t)$ applied on the inner surface specified by r_{inner}, as shown in Fig. 18. In this figure, the solid lines represent the concrete cover at the beginning of the corrosion initiation with initial notch of normalized depth α_0, while the dash lines denote the cracked concrete cover at time t since corrosion initiation with normalized crack depth, $\alpha(t)$. Parameter D is the characteristic size of the cracked concrete cover, e.g., the cover thickness. The parameters, α_0, $\alpha(t)$, and ξ, have been normalized with respect to D. Here ξ $(\alpha_0 \le \xi \le \alpha(t))$ is the normalized distance of any location on the crack surface formed at time t to the inner surface of the cracked concrete cover. In addition, $w(\xi, t)$ is the crack opening displacement of the crack surfaces at ξ. According to the cohesive crack model, the cohesive stress, $\sigma(\xi)$, has the potential to close the crack

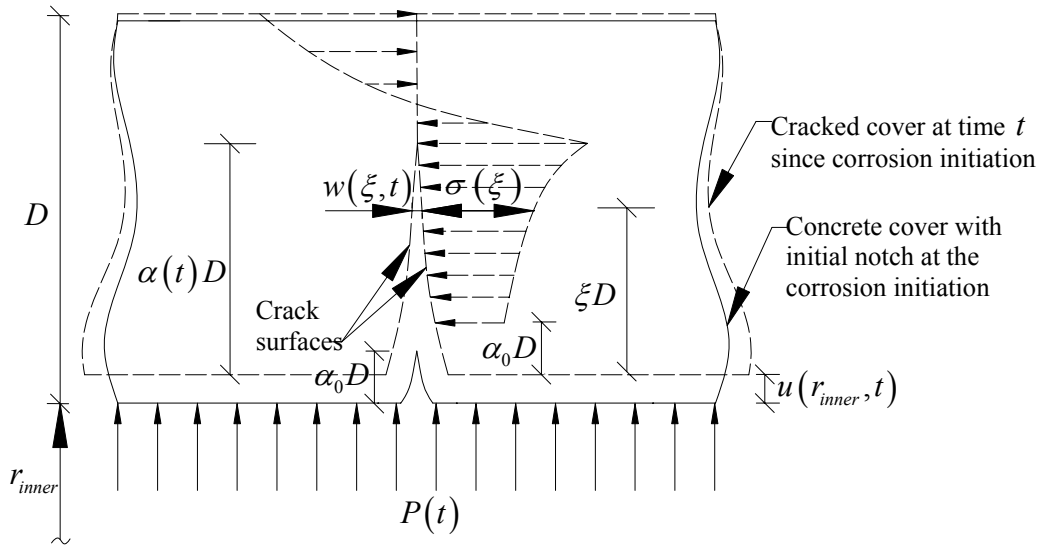

Fig. 18. Typical ligament for cracked concrete cover with cohesive crack

This effect counterbalances the crack opening effect resulted from $P(t)$. In the equilibrium condition of the cracked concrete cover at time t, the unknowns are $\alpha(t)$, $\sigma(\xi)$, and $P(t)$.

Following Bažant and Li (1995), the variations of Π^* with respect to $P(t)$, $\sigma(\xi)$, and $\alpha(t)$ are

$$\frac{\partial \Pi^*}{\partial P(t)} = -D\int_{\alpha_0}^{\alpha(t)} C^{P\sigma}(\xi)\cdot\sigma(\xi)\,d\xi + P(t)\cdot C^{PP} - u(r_{inner},t) = 0 \tag{27}$$

$$\frac{\partial \Pi^*}{\partial \sigma(\xi)} = D\int_{\alpha_0}^{\alpha(t)} C^{\sigma\sigma}(\xi,\xi')\cdot\sigma(\xi')\,d\xi' - P(t)\cdot C^{\sigma P}(\xi) + w(\xi,t) = 0 \tag{28}$$

$$E_r \cdot \frac{\partial \Pi^*}{\partial \alpha(t)} = \left\{ P(t) \cdot k_P\left[\alpha(t)\right] + D\int_{\alpha_0}^{\alpha(t)} k_G\left[\alpha(t), \xi\right] \cdot \sigma(\xi) d\xi \right\}^2 = 0 \qquad (29)$$

where, in Eq. (27), $C^{P\sigma}(\xi) = C^{\sigma P}(\xi)$ is the compliance function representing the crack opening displacement at location ξ cause by a unit corrosion pressure, $P(t) = 1$, applied on the inner surface of the concrete cover, C^{PP} is the compliance function representing the displacement in the same direction of $P(t)$ at r_{inner} due to $P(t) = 1$, $u(r_{inner}, t)$ is the given load-point deformation at r_{inner} and can be obtained by using Eq. (23) or (24). In Eq. (28), $C^{\sigma\sigma}(\xi, \xi')$ is the compliance function representing the crack opening displacement at location ξ due to two unit forces applied at ξ' $(\alpha_0 \le \xi' \le \alpha(t))$ on both crack surfaces. In Eq. (29), $k_P[\alpha(t)]$ is the dimensionless SIF at the crack front caused by the unit corrosion pressure, i.e., $P(t) = 1$, on the cracked cover with normalized crack depth $\alpha(t)$, $k_G[\alpha(t), \xi]$ is the dimensionless SIF at the crack front due to two unit forces applied at ξ on both crack surfaces with normalized depth $\alpha(t)$, and the subscript *G* denotes the Green function defined as in Bažant and Planas (1998). Eqs. (27) and (28) are the compatibility equations and Eq. (29) is the equilibrium equation.

According to the above definitions, the compliance functions, $C^{P\sigma}(\xi)$, C^{PP}, and $C^{\sigma\sigma}(\xi, \xi')$ can be computed as

$$C^{P\sigma}\left(\xi\right) = \frac{2}{E_r}\int_{\xi}^{\alpha(t)} k_P\left(\alpha'\right) \cdot k_G\left(\alpha', \xi\right) d\alpha' \qquad (30)$$

$$C^{PP} = \frac{2}{E_r}\int_{\alpha_0}^{\alpha(t)} k_P\left(\alpha'\right) \cdot k_P\left(\alpha'\right) d\alpha' \qquad (31)$$

$$C^{\sigma\sigma}(\xi,\xi') = \frac{2}{E_r}\int_{\max(\xi,\xi')}^{\alpha(t)} k_G(\alpha',\xi')\cdot k_G(\alpha',\xi)\,d\alpha' \tag{32}$$

By substituting Eqs. (30) to (32) into Eqs. (27) and (28), we can solve for the unknowns $\alpha(t)$, $\sigma(\xi)$, and $P(t)$ at time t for a given value of $u(r_{inner},t)$ and the provided $k_P[\alpha(t)]$ and $k_G[\alpha(t),\xi]$.

In general, $k_P[\alpha(t)]$ and $k_G[\alpha(t),\xi]$, can be obtained via series elastic analyses using BEM or FEM for a cracked RC structure for a given geometry of the crack. The efficiency of the proposed method depends on the availability of the dimensionless SIFs. Finding the dimensionless SIFs has been the focus of several studies (e.g., Fett and Munz 1997; Tada et al. 2000). In particular, Wu and Carlsson (1991) provide the dimensionless SIFs for some structures of various shapes with different crack configurations based on experiments and numerical computations.

Knowing $\sigma(\xi)$ and $P(t)$ at time t, we can solve for $w(\xi,t)$ using Eq. (28) as follows

$$w(\xi,t) = P(t)\cdot C^{\sigma P}(\xi) - D\int_{\alpha_0}^{\alpha(t)} C^{\sigma\sigma}(\xi,\xi')\cdot\sigma(\xi')\,d\xi' \tag{33}$$

where the first term on the right-hand side of the equation is the displacement of the crack opening at ξ caused by $P(t)$, and the second term is the displacement of the crack opening at the same location caused by the cohesive stress $\sigma(\xi')$. Since $P(t)$ and $\sigma(\xi')$ have opposite effects on the crack opening, the difference represents the actual crack opening displacement at ξ on the crack surfaces, as also shown in Fig. 18. In

general, since the maximum value of $w(\xi,t)$ occurs at the crack mouth, the CMOD can be computed as $w(\alpha_0,t)$.

Next we compute the maximum crack opening strain, $\tilde{\varepsilon}^f_{\max}(t)$, as the value of $\varepsilon^f_{\max}$ at $\xi=\alpha_0$ and time t, as $\tilde{\varepsilon}^f_{\max}(t)=\varepsilon^f_{\max}(\xi=\alpha_0,t)=w(\alpha_0,t)/h_c$ (Bažant and Planas 1998). Here, h_c is the width of the crack band (usually $h_c=3d_a$, where d_a is the maximum aggregate size). After solving for $\tilde{\varepsilon}^f_{\max}(t)$, we compute the stiffness degradation factor $\tilde{\eta}(t)$ as

$$\tilde{\eta}(t)=\frac{\phi\left[\tilde{\varepsilon}^f_{\max}(t)\right]}{E_r\tilde{\varepsilon}^f_{\max}(t)+\phi\left[\tilde{\varepsilon}^f_{\max}(t)\right]} \tag{34}$$

Appendix A shows the derivation of Eq. (34) based on the definition of the stiffness degradation factor.

Finally, the time to cracking of the concrete cover is found by determining the time needed by the crack front to reach the surface of the concrete cover starting from the time of corrosion initiation. This can be computed as the time at which $\alpha(t)=1$.

NUMERICAL EXAMPLES

In this section, we select two numerical examples to illustrate and validate the proposed method. The stiffness degradation factor is computed for each example as a function of time elapsed from corrosion initiation. In the computations, $u(r_{inner},t)$ in Eq. (27) is computed using Eq. (23) or (24), where the rust thickness, $d(t)$, is computed as (Pantazopoulou and Papoulia 2001)

$$d(t) = \sqrt{\left[R_{rb}(t)\right]^2 + \frac{\Delta V_r(t)}{\pi}} - R_{rb}(t) \tag{35}$$

where $\Delta V_r(t)$ is the volume of the rust product generated at time t and computed as

$$\Delta V_r(t) = \frac{m_r(t)}{\rho_r} \tag{36}$$

where ρ_r is the density of the rust product assumed to be 3600 kg/m^3 (224.7 lbs/ft^3) and $m_r(t)$ is the mass of the rust product at time t computed as (Liu and Weyers 1998)

$$m_r(t) = \left[2\int_0^t \frac{0.098}{\mu} \cdot \pi \cdot (2r_{inner}) \cdot i_{corr}(t')\,dt'\right]^{1/2} \tag{37}$$

where $\mu = 0.523$ is the molecular weight ratio between the steel and the rust (Liu and Weyers 1998), and the corrosion current density function, $i_{corr}(t)$ is defined as (Vu and Steward 2000)

$$i_{corr}(t) = 0.85 \cdot i_{corr,0} \cdot t^{-0.29} \tag{38}$$

where $i_{corr,0}$ is the corrosion current density at the corrosion initiation and is defined as

$$i_{corr,0} = \frac{37.5 \cdot (1 - w/c)^{-1.64}}{D} \tag{39}$$

here *w*/*c* is the water-to-cement ratio, and D is the cover thickness.

The reduced radius, $R_{rb}(t)$, for the corroded rebar is computed as

$$R_{rb}(t) = \sqrt{r_{inner}^2 - \Delta V_s(t)/\pi} \tag{40}$$

where $\Delta V_s(t)$ is the volume depleted from the reinforcing steel computed as

$$\Delta V_s(t) = \frac{\Delta V_r(t)\rho_r}{\rho_s}\mu \tag{41}$$

where ρ_s is the density of steel assumed to be 7800 kg/m^3 (487.0 lbs/ft^3).

The typical layout of the tested specimens in Liu and Weyers (1998) is shown in Fig. 19. The basic dimensions of the specimen tested in the laboratory (outdoor exposure) are 1180×1067×216 mm. Four layers of reinforcement are placed in the slabs. The top layer of reinforcement consists of reinforcing steel, each bar with 16-mm (0.63 in.) diameter. The remaining three layers beneath the corroding reinforcing steel consist of composite reinforcing bars, which are not subject to corrosion. Two specimens with clear covers of 48 mm (1.89 in.) (Series OA2859.6) and 27 mm (1.06 in.) (Series OE18512.0) are selected for the numerical examples here. Since the admixed chloride concrete in these two specimens are 5.69 kg/m^3 and 7.2 kg/m^3 respectively, which are higher than the normal values 0.60-0.83 kg/m^3 suggested by Liu (1996), the time to corrosion is negligibly small in the experiments conducted in Liu and Weyers (1998). Table 11 lists the parameters used in the numerical computations.

Instead of using BEM or FEM to find the SIF for a general cracked cross-section with corroded reinforcing steel, we use a simplified solution for the cracked concrete cover in these two examples. The simplification is made by modeling the concrete cover as a concrete cylinder concentric to the corroding reinforcing steel in each specimen.

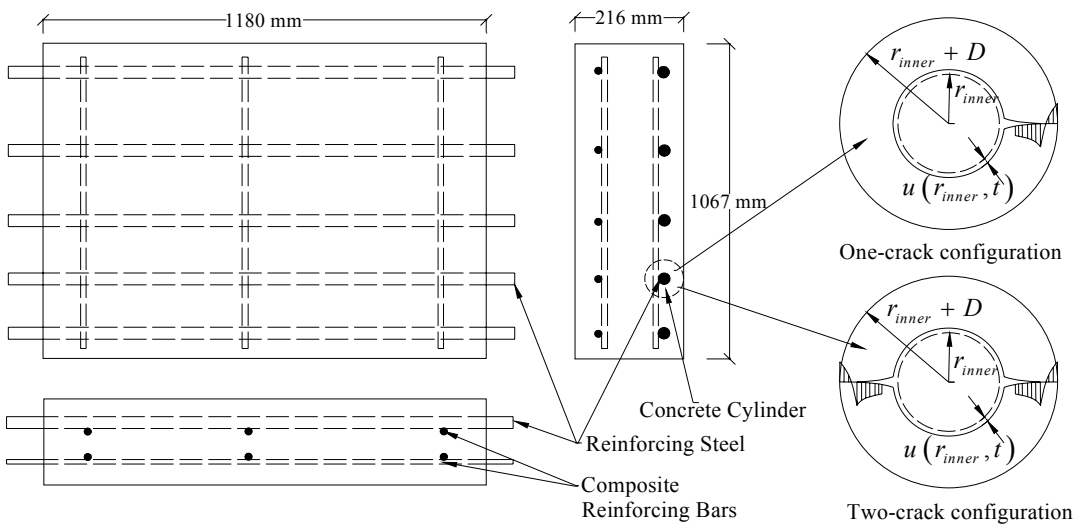

Fig. 19. Configuration of the specimens tested in Liu and Weyers (1998)

Table 11. Parameters used in the numerical examples

	Symbol	Specimen 1	Specimen 2
Cover, (mm)	D	48	27
Reinforcing steel diameter, (mm)	r_{inner}	16	16
Water to cement ratio	w/c	0.50	0.50
Max aggregate size, (mm)	d_a	16	16
Concrete strength (Mpa)	f_c'	31.5	31.5
Elastic modulus, (Gpa)	E_r	27	27
Creep coefficient	φ_r	2.0	2.0
Poisson ratio	v	0.18	0.18
Molecular weight ratio between steel and rust	μ	0.523	0.523

Fig. 19 also shows the concrete cylinders of one- and two-crack configurations with radii r_{inner} and $r_{inner} + D$ for the inner and outer walls, respectively. Here, the characteristic size for the cylinder cover is D. Two load-point deformations are chosen for $u(r_{inner}, t)$ in Eq. (27): 1) the effective rust expansion, i.e., boundary condition defined in Eq. (23); and 2) the rust thickness, i.e., boundary condition defined in Eq. (24). Note that $P(t)$ is applied on the inner surface of the cylinder. In the computations, the linear softening law is applied for the cracked cover concrete subject to tensile stress.

Fig. 20 shows the results for Specimen 1 with cover thickness of 48 mm. The top chart shows the location of crack front, $R_r(t) = \alpha(t) \cdot D + r_{inner}$, measured from the center of the cylinder to the crack front as a function of time. The solid-line denotes the results for the crack front computed by Li et al. (2006) using a smeared crack model with the load-point deformation of rust thickness. The dash-dotted line denotes the results computed by Li et al. (2006) for the load-point deformation of effective rust expansion. The bold solid-line shows the results computed using the proposed model with one-crack configuration in the concrete cylinder subject to rust thickness. The bold dash-line shows the results computed using the proposed model with one-crack configuration in the concrete cylinder subject to effective rust expansion. The dash- and dotted- lines show the corresponding results for the same concrete cylinder with two-crack configuration applied with different load-point deformations. The crack front reaches the cover surface when $R_r(t)$ reaches the value of 56 mm (2.20 in.), i.e., $\alpha(t) = 1$. The time to cracking predicted using the proposed method on the concrete cylinder with one-

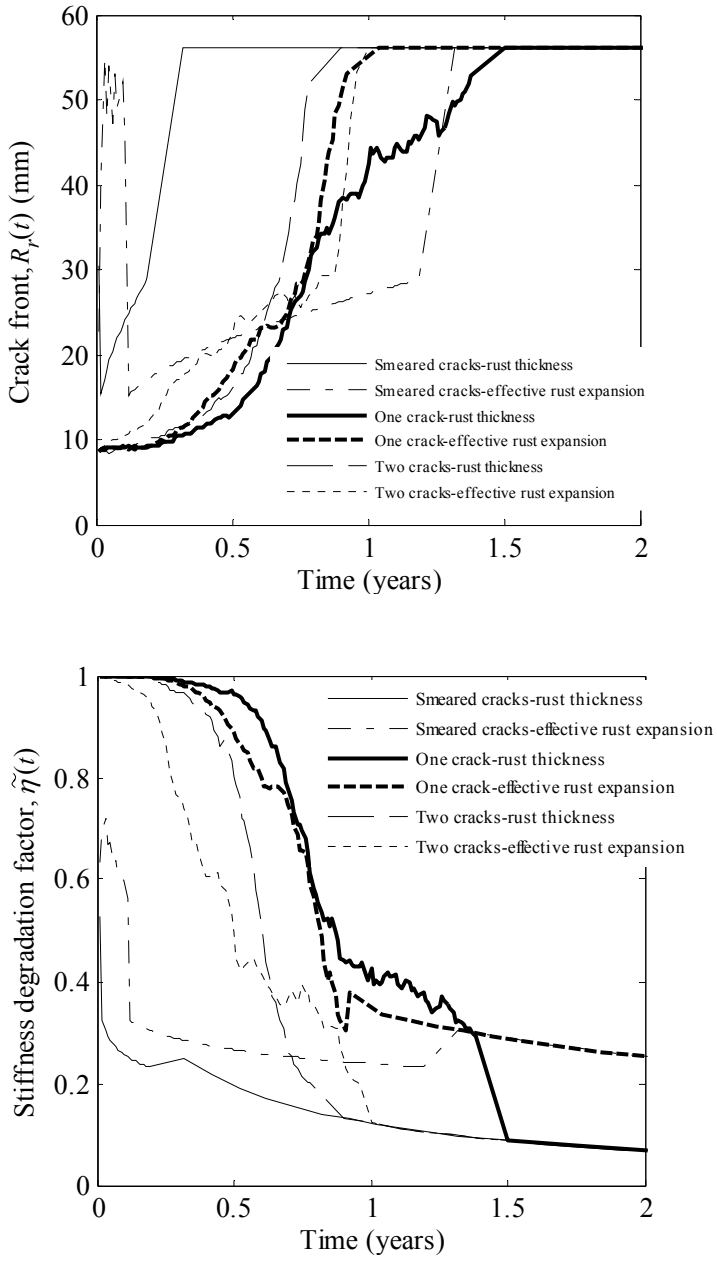

Fig. 20. Crack front and stiffness degradation factor as functions of time after corrosion initiation for specimen with 48-mm cover

crack configuration in the concrete cylinder subject to effective rust expansion. The dash- and dotted- lines show the corresponding results for the same concrete cylinder

with two-crack configuration applied with different load-point deformations. The crack front reaches the cover surface when $R_r(t)$ reaches the value of 56 mm (2.20 in.), i.e., $\alpha(t) = 1$. The time to cracking predicted using the proposed method on the concrete cylinder with one-crack configuration subject to the rust thickness (bold-solid line) is 1.50 years, which is in agreement with the 1.84 years measured in Liu and Weyers (1998) for this specimen. It is noted that, when two-crack configuration subject to effective rust expansion is used, the predicted time to cracking (1.04 years) is smaller than the time computed using the rust thickness. This is because rust thickness is generally greater than effective rust expansion (see Eqs. (23) and (24)). The computations show steady growth of the crack front during the cracking. In contrast, the crack front computed from smeared crack model bounces up and down before increasing to the value of 56 mm. It is also notice that the smeared crack models underestimate the time to cracking (predicted at 0.32 years for the applied rust thickness and 1.32 years for the applied effective rust expansion respectively). Furthermore, the prediction from the applied rust thickness is smaller than the one from the applied effective rust expansion.

The bottom chart shows the stiffness degradation factors as a function of time. Using the proposed method, the stiffness degradation factors decrease from the value of 1.0 at the beginning of the cracking propagation. The results from the smeared crack model in Li et al. (2006) start from values lower than 1.0 and decay faster than the results from other models. After the crack front reaches the cover surface, the stiffness degradation factor is estimated using the model in Li et al. (2006) since the proposed method is no longer applicable.

The bottom chart shows the stiffness degradation factors as a function of time. Using the proposed method, the stiffness degradation factors decrease from the value of 1.0 at the beginning of the cracking propagation. The results from the smeared crack model in Li et al. (2006) start from values lower than 1.0 and decay faster than the results from other models. After the crack front reaches the cover surface, the stiffness degradation factor is estimated using the model in Li et al. (2006) since the proposed method is no longer applicable.

Fig. 21 shows similar results for Specimen 2 which has cover thickness of 27 mm (1.06 in.). The times to cracking computed using the smeared crack model are significantly smaller (0.16 and 0.36 years respectively) than the times to cracking measured (0.72 years) in Liu and Weyers (1998). In contrast, the time to cracking predicted using the proposed model using the one-crack configuration is 0.69 years, which is in agreement the experimental value. The results from the two-crack configuration are not shown due to convergence problems. For the bottom chart in Fig. 21, similar observations can be made to those already made for the bottom chart in Fig. 20.

Table 12 lists the predicted values for the time to cracking for both examples investigated using different crack models with different load-point deformations. As already observed in Fig. 20, there is agreement between the measured values and the values predicted using the proposed model with one-crack configuration applied with the rust thickness. Results computed for a concrete cylinder with two-crack configuration for one-crack configuration represents more realistically the actual cracking in the slab

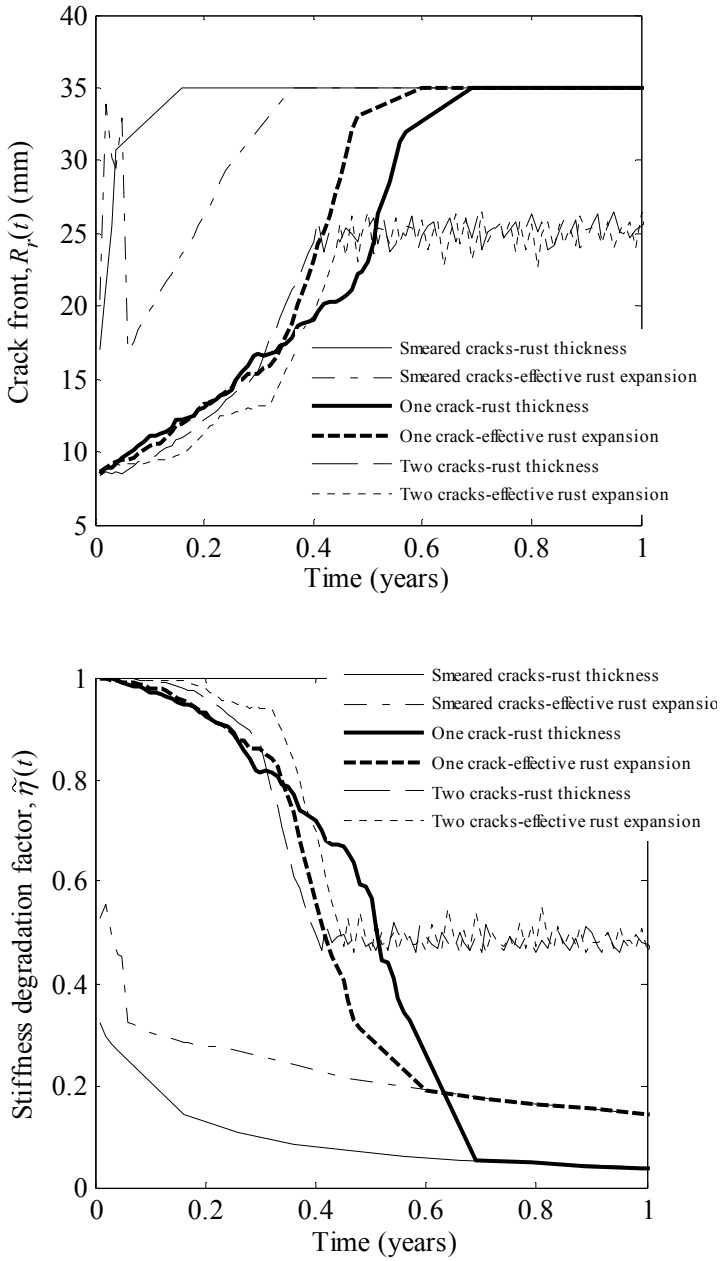

Fig. 21. Crack front and stiffness degradation factor as functions of time after corrosion initiation for specimen with 27-mm cover

specimen shown in Fig. 19 than the two-crack configuration because of the confining effects of the concrete and bars underneath the corroding reinforcing steel in the slab.

Table 12. Predicted and measured time to crack for the two numerical examples

Time to cracking (year)	Specimen 1		Specimen 2	
	Simulated	Measured	Simulated	Measured
Smeared crack model-rust thickness	0.32	1.84	0.16	0.72
Smeared crack model-effective rust expansion	1.32		0.36	
One-crack configuration-rust thickness	1.50		0.69	
One-crack configuration-effective rust expansion	1.04		0.60	
Two-crack configuration-rust thickness	0.90		N/A	
Two-crack configuration-effective rust expansion	1.00		N/A	

To investigate the relationship between the stiffness degradation and the location of the crack front, Fig. 22 shows $\tilde{\eta}(t)$ as a function of $R_r(t)$ for each case in the numerical computations. The bold-solid line illustrates the relationship between $\tilde{\eta}(t)$ and $R_r(t)$ for the first specimen using load-point displacement of rust thickness. The bold-dashed line illustrates the same relationship from effective rust expansion applied for this specimen. Overall, $\tilde{\eta}(t)$ decreases with an increase in $R_r(t)$. This means the secant stiffness of cracked concrete decreases as the crack front propagates. This is because the maximum strain, $\tilde{\varepsilon}^f_{\max}(t)$, increases due to the increasing CMOD during the cracking. The corresponding results for the second specimen are denoted by the dashed-dotted and the dotted lines, respectively. We can see that the proposed models work

well for the second specimen in correlating $\tilde{\eta}(t)$ with $R_r(t)$ using either kind of load-point displacements. For these two examples, the stiffness degradation factor decreases with the increase of the location of crack front. The difference in the applied load-point deformations has marginal effect in correlating $\tilde{\eta}(t)$ with $R_r(t)$.

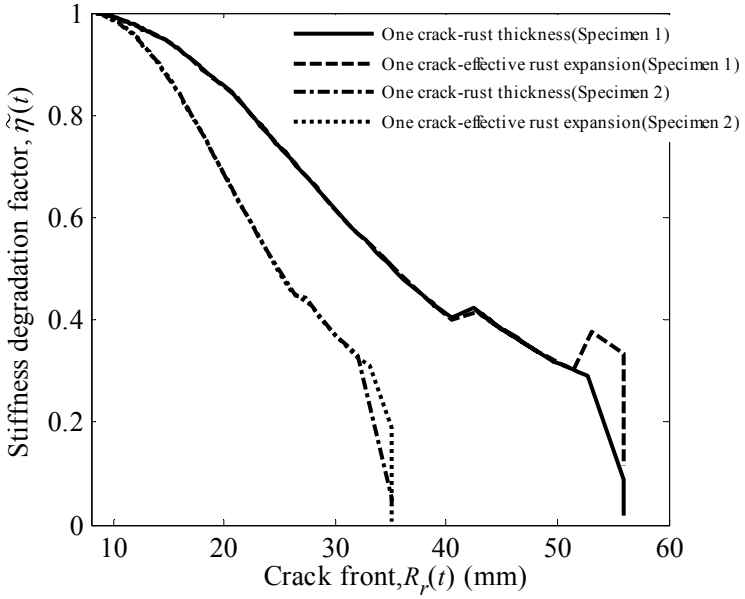

Fig. 22. Stiffness degradation factor as a function of the crack front for both specimens

SUMMARY

Due to corrosion in reinforcing steel, corrosion pressure builds up between the concrete cover and the reinforcing steel and results in the cracking of the concrete cover. The stiffness of cracked cover is subject to degradation process. Based on the energy principle of the fractured structures with cohesive cracks, a stiffness degradation factor is

proposed to represent the stiffness degradation in corroded RC structure. By solving the compatibility and equilibrium equations from the energy principle applied to the cracked RC structure, the crack depth, cohesive stress, and corrosive pressure can be determined at each moment of the cracking process. The stiffness degradation factor is then computed in terms of the maximum crack opening strain during the cracking progress. The cracking progress weakens the stiffness of cracked concrete as the crack front approaches the surface of the RC structure. The time to cracking of a concrete cover is determined as the time from the corrosion initiation needed by the crack front to reach the surface of the concrete cover. The proposed stiffness degradation factor provides an effective means to model the stiffness degradation and to estimate the time to cracking of cracked concrete based on the change of energy in a fracturing RC structure.

Two numerical examples illustrate the application of the proposed models. The effects of using one- and two-crack configurations are also investigated. The predicted times to cracking of concrete cover are in good agreement with the measured values from experimental results.

CHAPTER V

SEISMIC FRAGILITY ESTIMATES FOR CORRODED RC BRIDGES WITH TWO-COLUMN BENTS

The effects of corrosion in reinforcing steel have two folds: the loss of reinforcing steel and the cracking of concrete cover. While the loss of the reinforcing steel weakens the capacity of the RC bridges, the cracking of concrete cover reduces the stiffness of the RC bridges. This Chapter proposed a methodology to incorporate these corrosion effects into the fragility estimates of the corroded RC bridges with two-column bents.

INTRODUCTION

Due to the onset of corrosion, the capacity reduction in RC columns has become a major concern in estimating the seismic fragility of corroded RC bridges. Although significant efforts have been made to model the corrosion effects on the design, assessment, and maintenance of RC bridges (e.g., Steward and Rosowsky 1998; Liu and Weyers 1998; Enright and Frangopol 1998a,b; Vu and Stewart 2000; Melchers 2003; Stewart 2004), limited work has been done for the estimation of seismic fragility of corroded RC bridges. In the recent studies, Choe et al. (2008a, b) presented a merged formulation to estimate the seismic fragility of corroded RC bridges with single-column bents. To quantify the corrosion effects on the seismic fragility, the probabilistic models for the chloride-induced corrosion and the time-dependent corrosion rate are combined with the

probabilistic capacity and demand models developed in Gardoni et al. (2002), Gardoni et al. (2003), and Choe et al. (2008a).

This chapter extends the study on seismic fragility for the corroded RC bridges with two-column bents (Zhong et al. 2008e). Structural capacities are defined based on the probabilistic models for the deformation and shear capacities of RC bridges with two-column bents. Probabilistic demand models are also used to estimate the corresponding demands on the RC columns for given seismic intensities. The probabilistic capacity and demand models are then combined with the probabilistic models for chloride-induced corrosion and the time-dependent corrosion rate to account for the variation of capacity and demand over time. In particular, the loss of reinforcing steel is estimated for individual reinforcing bars. The probability distributions of the loss of reinforcing steel are incorporated into the probabilistic capacity and demand models. The stiffness degradation of cracked cover is also considered in terms of the secant stiffness of the cover. Seismic fragility functions are then formulated on the column, bent, and bridge levels. The fragility formulations incorporate the uncertainties in the parameters of capacity and demand models, and the inexactness (or model error) in modeling the material deterioration, structural capacity, and seismic demands. As an application, seismic fragility is estimated on the column, bent, and bridge levels for a corroded RC bridge with 11 two-column bents in a 100-year period.

This chapter includes four sections. In the next, we include a brief description on the corrosion process in RC structures and introduce the procedures to incorporate the corrosion effects into the probabilistic capacity and demand models for RC bridges with

two-column bents. This is followed by the formulations for the seismic fragility functions on the column, bent, and bridge levels for corroded RC bridges. Finally, we provide a numerical illustration for the proposed methodology by estimating the seismic fragilities for the corroded modified I-880.

PROBABILISTIC CAPACITY AND DEMAND MODELS FOR CORRODED RC BRIDGES WITH TWO-COLUMN BENTS

In this section, we first briefly describe the corrosion process in the reinforcing steel and the effects on the concrete cover. Then, we present the probabilistic models to include corrosion effects from the loss of reinforcing steel and to consider the stiffness degradation in the concrete cover subject to corrosion-induced cracking. Finally, we propose a method to incorporate these corrosion effects into the probabilistic capacity and demand models for RC bridges with two-column bents.

Corrosion effects on the reinforcement and on the cover concrete of RC structures

The concrete cover provides the protection for reinforcing steel against the corrosive agents, such as chlorides, moisture, seawater, deicing salts, oxygen, carbon dioxide, sulfates, and acids. With the highly alkaline pore solution existing in the cover concrete, a layer of passive film is formed on the surface of the reinforcing steel as the initial corrosion product (Liu 1996). However, due to the capillary of concrete and the diffusion process, the corrosive agents can breach onto the surface of reinforcing steel through the concrete cover in the aggressive environments. With sufficient amount of corrosive agent, the passive film can be broken and the corrosion process will be initiated.

Because of the density difference between the depleted steel and the rust product, the concrete cover is subject to cumulative corrosion pressure exerted on the inner surface of the cover. The corrosion pressure will crack the concrete cover shortly after the corrosion initiation. The cracking process causes the stiffness degradation in the concrete cover.

Probabilistic models for corrosion on RC columns

During the corrosion process, two main stages can be mathematically described: the time to corrosion initiation and the time to cracking of concrete cover. The first stage defines the moment for the corrosion onset in the reinforcing steel. The second stage defines the time elapsed from the corrosion initiation to the complete cracking of concrete cover.

The time to corrosion initiation, $T_{corr,i}^{j}$, for rebar j in Column i subject to chloride-induced corrosion is a random variable and can be modeled using the probabilistic model proposed in DuraCrete (2000) as

$$T_{corr,i}^{j} = X_I \left\{ \frac{\left(d_i^j\right)^2}{4k_e k_t k_c D_0 \left(t_0\right)^n} \left[erf^{-1}\left(1 - \frac{C_{cr}}{C_s}\right)\right]\right\}^{1/(1-n)} \tag{42}$$

where X_I is defined as the model uncertainty coefficient to account for the idealization by applying the Fick's second law in the diffusion process, d_i^j is the cover thickness for rebar j in Column i, k_e is an environment factor, k_t includes the influence of the test methods to determine the empirical diffusion coefficient D_0, k_c is a parameter that accounts for the influence of curing, t_0 is the reference period for D_0, n is the age

factor, $erf(\cdot)$ is the error function, C_{cr} is the critical chloride concentration on the reinforcing steel, and C_s is the chloride concentration on the concrete surface. In general, the probability density function (PDF) for $T^j_{corr,i}$, $f_{\boldsymbol{T}^j_{corr,i}}(t^j_{corr,i})$, can be estimated by using the corresponding probabilistic models (DuraCrete 2000) for all the parameters on the right side of Eq. (42). The function $f_{\boldsymbol{T}^j_{corr,i}}(t^j_{corr,i})$ is particularly useful when individual reinforcing bars have different thickness for the concrete cover since the mean and standard deviation of $T^j_{corr,i}$ for rebar j are different from the others. Further, we define a random vector $\boldsymbol{T}_{corr,i} = (T^1_{corr,i}, T^2_{corr,i}, ..., T^{n_i}_{corr,i})$ consisting of $T^j_{corr,i}$ ($j = 1, 2, ..., n_i$) and the corresponding joint PDF $f_{\boldsymbol{T}_{corr,i}}(\boldsymbol{t}_{corr,i})$ for $\boldsymbol{T}_{corr,i}$. Here, n_i is the total number of reinforcing bars in Column i.

After the corrosion initiates in rebar j at time $T^j_{corr,i}$ predicted by Eq. (42), the built-up corrosion pressure on the inner surface of the cover will crack the concrete cover. The corrosion-induced cracks grow radially toward the outer surface of the cover. As the cracks propagate, the stiffness of the cracked cover concrete will decrease correspondingly. This stiffness degradation can be estimated in terms of the strain corresponding to the maximum opening of the concrete cracks based on energy principles applied to a fractured RC structure (Zhong et al. 2008c). The time to cracking of concrete cover can be estimated by computing the time needed for the crack front to reach the cover surface (Zhong et al. 2008c). In general, the degrees of stiffness degradation in concrete cover for individual reinforcing bars are different because of the

differences among the corroding process in the reinforcing steel. The secant stiffness of cracked cover for rebar j in Column i at time t, $E_{\theta,i}^{j}(t)$, can be estimated as $E_{\theta,i}^{j}(t) = \eta_i^j(t) \cdot E_r$. Here, $\eta_i^j(t)$ is a stiffness degradation factor, defined as the ratio between the secant stiffness and initial stiffness in Zhong et al. (2008c) as

$$\eta_i^j(t) = \frac{\phi\left[\tilde{\varepsilon}_{j,i}^{f}(t)\right]}{E_r \tilde{\varepsilon}_{j,i}^{f}(t) + \phi\left[\tilde{\varepsilon}_{j,i}^{f}(t)\right]} \quad 0 < \eta_i^j(t) \le 1 \tag{43}$$

and E_r is the initial stiffness of pristine concrete, $\tilde{\varepsilon}_{j,i}^{f}(t)$ is the maximum crack opening strain in the cover concrete for rebar j in Column i before the unloading (Bažant and Planas 1998) at time t, $\phi(\cdot)$ is the softening stress-strain curve of concrete subject to tensile stress. Here, $\eta_i^j(t)$ is also random in nature and the corresponding probabilistic distribution of $\eta_i^j(t)$ can be estimated by considering the probabilistic models for $\phi(\cdot)$, $\tilde{\varepsilon}_{j,i}^{f}(t)$, and E_r. Similarly, we define a random vector $\boldsymbol{\eta}_i(t) = \{\eta_i^1(t), \eta_i^2(t), ..., \eta_i^{n_i}(t)\}$, to estimate the stiffness degradation of the concrete covers for all n_i bars in Column i, and the corresponding joint PDF, $f_{\boldsymbol{\eta}_i(t)}[\eta_i(t)]$, for $\boldsymbol{\eta}_i(t)$ at time t.

Incorporating the probabilistic corrosion models into the capacity and demand models

By partitioning the vector of random variables in $\mathbf{x}$ for a bridge into a vector of material and geometric variables, $\mathbf{r}$, and a vector of seismic intensities, $\mathbf{s}$, we can define the probabilistic capacity models, $C_{ki}(t, \mathbf{r}, \boldsymbol{\Theta}_{Ck}, \varepsilon_{Cki})$, for deformation $(k = \delta)$ and shear $(k = v)$, for corroded Column *i* at time *t* as (Choe et al. 2008a)

$$C_{ki}\left(t,\mathbf{r},\boldsymbol{\Theta}_{Ck},\varepsilon_{Cki}\right)=\int_0^{\infty}C_{ki}\left(t,\mathbf{r},\boldsymbol{\Theta}_{Ck},\varepsilon_{Cki}\middle|\boldsymbol{t}_{corr,i}\right)\cdot f_{\boldsymbol{T}_{corr,i}}\left(\boldsymbol{t}_{corr,i}\right)d\boldsymbol{t}_{corr,i} \tag{44}$$

here $\boldsymbol{\Theta}_{Ck}=\{\boldsymbol{\Theta}_{C\delta},\boldsymbol{\Theta}_{Cv}\}$ denotes the parameters in the probabilistic capacity models in Gardoni et al. (2002) and Choe et al. (2008a). Appendix A includes further details for $\boldsymbol{\Theta}_{Ck}$ for completeness. Here, ε_{Cki} is the standard normal random variable. Considering the joint PDF, $f_{\boldsymbol{T}_{corr,i},\boldsymbol{\eta}_i(t)}[\boldsymbol{t}_{corr,i},\boldsymbol{\eta}_i(t)]$, for random vectors $\boldsymbol{T}_{corr,i}$ and $\boldsymbol{\eta}_i(t)$, the capacity k for Column i in Eq. (44) can be further written as

$$\begin{aligned}C_{ki}\left(t,\mathbf{r},\boldsymbol{\Theta}_{Ck},\varepsilon_{Cki}\right)=\int_0^{\infty}\int_0^{1}&C_{ki}\left[t,\mathbf{r},\boldsymbol{\Theta}_{Ck},\varepsilon_{Cki}\middle|\boldsymbol{t}_{corr,i},\boldsymbol{\eta}_i\left(t\right)\right]\\&\cdot f_{\boldsymbol{T}_{corr,i},\boldsymbol{\eta}_i(t)}\left[\boldsymbol{t}_{corr,i},\boldsymbol{\eta}_i\left(t\right)\right]d\boldsymbol{\eta}_i\,d\,\boldsymbol{t}_{corr,i}\end{aligned} \tag{45}$$

In general, $\boldsymbol{T}_{corr,i}$ and $\boldsymbol{\eta}_i(t)$ are not independent since the secant stiffness of the cracked concrete at time t is closely related to the times to corrosion initiation for all reinforcing bars. And $C_{ki}\left[t,\mathbf{r},\boldsymbol{\Theta}_{Ck},\varepsilon_{Cki}\middle|\boldsymbol{t}_{corr,i},\boldsymbol{\eta}_i\left(t\right)\right]$ is defined as

$$\begin{aligned}C_{ki}\left[t,\mathbf{r},\boldsymbol{\Theta}_{Ck},\varepsilon_{Cki}\middle|\boldsymbol{t}_{corr,i},\boldsymbol{\eta}_i\left(t\right)\right]=&\,\hat{c}_{ki}\left[t,\mathbf{r},\boldsymbol{\Theta}_{Ck}\middle|\boldsymbol{t}_{corr,i},\boldsymbol{\eta}_i\left(t\right)\right]\\&+\gamma_{Ck}\left[t,\mathbf{r},\boldsymbol{\Theta}_{Ck}\middle|\boldsymbol{t}_{corr,i},\boldsymbol{\eta}_i\left(t\right)\right]+\sigma_{Ck}\varepsilon_{Cki}\end{aligned} \tag{46}$$

where $\hat{c}_{ki}[t,\mathbf{r},\boldsymbol{\Theta}_{Ck}\middle|\boldsymbol{t}_{corr,i},\boldsymbol{\eta}_i(t)]$ is the deterministic prediction for capacity k considering the corrosion effects from the loss of reinforcing steel and the cracked concrete cover, $\gamma_{Ck}[t,\mathbf{r},\boldsymbol{\Theta}_{Ck}\middle|\boldsymbol{t}_{corr,i},\boldsymbol{\eta}_i(t)]$ is the correction term for $\hat{c}_{ki}[t,\mathbf{r},\boldsymbol{\Theta}_{Ck}\middle|\boldsymbol{t}_{corr,i},\boldsymbol{\eta}_i(t)]$, $\sigma_{Ck}\varepsilon_{Cki}$ is the model error for the capacity model, and σ_{Ck} is the mean of the model error for the probabilistic model. Appendix A includes further details for $\gamma_{Ck}[t,\mathbf{r},\boldsymbol{\Theta}_{Ck}\middle|\boldsymbol{t}_{corr,i},\boldsymbol{\eta}_i(t)]$.

To compute $\hat{c}_{\delta i}[t,\mathbf{r},\boldsymbol{\Theta}_{C\delta}|\boldsymbol{t}_{corr,i},\boldsymbol{\eta}_i(t)]$, three different components are considered (Gardoni et al. 2002): (1) the flexural component due to the linear curvature of the column; (2) the shear component due to the shear deformation; and (3) the slipping component from the slippage of reinforcing steel. These three components are closely related to the section properties of the RC column. Thus, the loss of reinforcing steel affects the deterministic predictions of deformation capacity. For $\hat{c}_{vi}[t,\mathbf{r},\boldsymbol{\Theta}_{Cv}|\boldsymbol{t}_{corr,i},\boldsymbol{\eta}_i(t)]$, however, only the loss of reinforcing steel affects the capacity prediction for shear.

Similarly, given the seismic intensities, $\mathbf{s}$, we can define the probabilistic demand models, $D_{ki}(t,\mathbf{r},\boldsymbol{\Theta}_{Dk},\varepsilon_{Dki})$ $(k=\delta,v)$, for Column i at time t as

$$D_{ki}\left(t,\mathbf{r},\boldsymbol{\Theta}_{Dk},\varepsilon_{Dki}\right)=\int_0^\infty\int_0^1 D_{ki}\left[t,\mathbf{r},\boldsymbol{\Theta}_{Dk},\varepsilon_{Dki}|\boldsymbol{t}_{corr,i},\boldsymbol{\eta}_i\left(t\right),\mathbf{s}\right] \cdot f_{\boldsymbol{T}_{corr,i},\boldsymbol{\eta}_i(t)}\left[\boldsymbol{t}_{corr,i},\boldsymbol{\eta}_i\left(t\right)\right]d\boldsymbol{\eta}_i\, d\,\boldsymbol{t}_{corr,i} \tag{47}$$

and

$$D_{ki}\left[t,\mathbf{r},\boldsymbol{\Theta}_{Dk},\varepsilon_{Dki}|\boldsymbol{t}_{corr,i},\boldsymbol{\eta}_i\left(t\right),\mathbf{s}\right]=\hat{d}_{ki}\left[t,\mathbf{r},\boldsymbol{\Theta}_{Dk}|\boldsymbol{t}_{corr,i},\boldsymbol{\eta}_i\left(t\right),\mathbf{s}\right] +\gamma_{Dk}\left[t,\mathbf{r},\boldsymbol{\Theta}_{Dk}|\boldsymbol{t}_{corr,i},\boldsymbol{\eta}_i\left(t\right),\mathbf{s}\right]+\sigma_{Dk}\varepsilon_{Dki} \tag{48}$$

The definitions of the symbols are analogous to the ones in Eq. (46). In addition, $\mathbf{s}=(S_a,\text{PGV/PGA})$, where S_a is the spectral acceleration, PGV/PGA is the ratio between the peak ground velocity (PGV) and the peak ground acceleration (PGA). At the right side of the equation, $\hat{d}_{ki}[t,\mathbf{r},\boldsymbol{\Theta}_{Dk}|\boldsymbol{t}_{corr,i},\boldsymbol{\eta}_i(t),\mathbf{s}]$ is the deterministic prediction for demand k, and $\gamma_{Dk}[t,\mathbf{r},\boldsymbol{\Theta}_{Dk}|\boldsymbol{t}_{corr,i},\boldsymbol{\eta}_i(t),\mathbf{s}]$ is the corresponding correction term. These

two terms are closely related to the pushover analysis of the RC columns and the entire bridge. Appendix A includes further details for the probabilistic demand models.

FRAGILITY ESTIMATES FOR CORRODED RC BRIDGES WITH TWO-COLUMN BENTS

The fragility of a bridge consisting of s structural components at time t for given seismic intensity $\mathbf{s}$ is written as

$$F\left(t,\mathbf{s},\boldsymbol{\Theta}\right)=P\left[\bigcup_{i=1,..,s}\bigcup_{k=\delta,v}\left\{g_{ki}\left(t,\mathbf{r},\boldsymbol{\Theta}_{k},\boldsymbol{\varepsilon}_{ki}\middle|\mathbf{s}\right)\le 0\right\}\right] \tag{49}$$

where $\boldsymbol{\varepsilon}_{ki}=(\varepsilon_{Cki},\varepsilon_{Dki})$ and $g_{ki}(t,\mathbf{r},\boldsymbol{\Theta},\boldsymbol{\varepsilon}_{ki}\,|\,\mathbf{s})$ is the limit state function, for corroded Column i at time t, expressed as

$$g_{ki}\left(t,\mathbf{r},\boldsymbol{\Theta}_{k},\boldsymbol{\varepsilon}_{ki}\middle|\mathbf{s}\right)=C_{ki}\left(t,\mathbf{r},\boldsymbol{\Theta}_{Ck},\varepsilon_{Cki}\right)-D_{ki}\left(t,\mathbf{r},\boldsymbol{\Theta}_{Dk},\varepsilon_{Dki}\middle|\mathbf{s}\right)\le 0,\quad i=1,..,s;\quad k=\delta,v \tag{50}$$

A predictive estimate of Eq. (8) at time t is obtained as the mean of $F(t,\mathbf{s},\boldsymbol{\Theta})$ by integrating over the distribution of $\boldsymbol{\Theta}$ as

$$\tilde{F}\left(t,\mathbf{s}\right)=\int_{\boldsymbol{\Theta}}F\left(t,\mathbf{s},\boldsymbol{\Theta}\right)f_{\boldsymbol{\Theta}}\left(\boldsymbol{\theta}\right)d\boldsymbol{\theta} \tag{51}$$

A point estimate of Eq. (8) at time t is obtained by ignoring the epistemic uncertainties in the model parameters, $\boldsymbol{\Theta}$, and using a point estimate, $\hat{\boldsymbol{\Theta}}$ (e.g., the mean of $\boldsymbol{\Theta}$), instead of $\boldsymbol{\Theta}$. Then the point estimate of seismic fragility for the bridge at time t can be written as

$$\hat{F}\left(t,\mathbf{s}\right)=F\left(t,\mathbf{s},\hat{\boldsymbol{\Theta}}\right) \tag{52}$$

Similar to the formulations in Chapter I, in the special cases where vector $\mathbf{r}$ are known for a given bridge, $\hat{F}(t,\mathbf{s})$ can be also computed in terms of multinormal probability distribution function of $\boldsymbol{\varepsilon}_{ki} = (\varepsilon_{Cki}, \varepsilon_{Dki})$ depending on the number of limit state functions under consideration.

When only one limit state is considered, we have the following approximated closed-form solution for the fragility of Column i in mode k of failure

$$\begin{aligned} \hat{F}(t,\mathbf{s}) &= P\left[g_{ki}\left(t,\hat{\mathbf{r}},\hat{\boldsymbol{\Theta}}_k,\boldsymbol{\varepsilon}_{ki}\middle|\mathbf{s}\right) \le 0 \right] \\ &= P\left[C_{ki}\left(t,\mathbf{r},\boldsymbol{\Theta}_{Ck},\varepsilon_{Cki}\right) - D_{ki}\left(t,\mathbf{r},\boldsymbol{\Theta}_{Dk},\varepsilon_{Dki}\middle|\mathbf{s}\right) \le 0 \right] \\ &= 1-\Phi\left(u_{ki}\right) \end{aligned} \tag{53}$$

When two limit state functions are considered for the fragility of a single RC column in either deformation or shear mode of failure, we have the fragility function, expressed as

$$\begin{aligned} P\left[\bigcup_{k=\delta,v} g_{ki}\left(t,\mathbf{r},\boldsymbol{\Theta}_k,\boldsymbol{\varepsilon}_{ki}\middle|\mathbf{s}\right) \le 0 \right] &= 1-P\left[\bigcap_{k=\delta,v} g_{ki}\left(t,\mathbf{r},\boldsymbol{\Theta}_k,\boldsymbol{\varepsilon}_{ki}\middle|\mathbf{s}\right) > 0 \right] \\ &= 1-P\left[\bigcap_{k=\delta,v} \left\{ D_{ki}\left(t,\mathbf{r},\hat{\boldsymbol{\Theta}}_{Dk},\varepsilon_{Dki}\middle|\mathbf{s}\right) - C_{ki}\left(t,\mathbf{r},\hat{\boldsymbol{\Theta}}_{Ck},\varepsilon_{Cki}\right) < 0 \right\} \right] \\ &= 1-\Phi_2\left(-u_{\delta i},-u_{vi};\hat{\rho}_{\delta_i,v_i}\right) \end{aligned} \tag{54}$$

For the second and third cases, similar formulations are applicable.

Further, when more than two limit states are considered in fragility estimation, the point estimate for Eq. (8) can be formulated as

$$\begin{aligned}\hat{F}(t,\mathbf{s}) &= P\left[\bigcup_{i=1,..,s}\bigcup_{k=\delta,v}\left\{g_{ki}\left(t,\mathbf{r},\hat{\boldsymbol{\Theta}}_k,\boldsymbol{\varepsilon}_{ki}\middle|\mathbf{s}\right)\le 0\right\}\right] \\ &= 1-P\left[\bigcap_{i=1,..,s}\bigcap_{k=\delta,v}\left\{g_{ki}\left(t,\mathbf{r},\hat{\boldsymbol{\Theta}}_k,\boldsymbol{\varepsilon}_{ki}\middle|\mathbf{s}\right)>0\right\}\right] \\ &= 1-\Phi_{2s}\left(-\mathbf{u};\hat{\boldsymbol{\rho}}\right)\end{aligned} \tag{55}$$

NUMERICAL EXAMPLES

As the application, the modified I-880 is used to illustrate the proposed methodology. The water-to-cement ratio for the concrete in the RC columns is assumed to be 0.5. Tidal situation with constantly humid or many humid-dry cycles is assumed for the residing environment of the modified I-880. The curing time for the column concrete is assumed at 1 day. The distribution parameters for the random variables defined in Eq. (42) are listed in Table 13.

In the next, we will introduce the simplified model of $\boldsymbol{\eta}_i(t)$ for this application first, followed by the model for $\boldsymbol{T}_{corr,i}$. Finally, the numerical results and the discussions are presented.

Consideration of $\boldsymbol{\eta}_i(t)$ for the concrete cover in corroded RC columns

For simplicity, in this application, point estimates of $\boldsymbol{\eta}_i(t)$ for Column i ($i=1,2,...,22$) are used in the fragility estimation. We assume the confined core is not susceptible to corrosion effect. To determine the stiffness degradation factor $\eta_i^j(t)$, one of the challenges is to identify the cover area influenced by corrosion-induced cracking. To simplify the analysis, we approximate the secant stiffness of the cracked cover outside bar j as that of the cracked concrete cylinder concentric to bar j' with the smallest

Table 13. Distribution and Statistics of parameters in considering the corrosion effect

Variables	Distribution	Mean	Standard deviation	A	B
X_1	Lognormal	1.0	0.05		
d_c	Lognormal	0.022, 0.051 and 0.13 (m)	0.0004, 0.0010, and 0.003 (m)		
k_e	Gamma	0.265	0.045		
k_t	Normal	0.832	0.024		
k_c	Beta	1.5	0.3	1.0	4.0
D_0	Normal	473(mm^2/year)	43.2 ($10^{-12}m^2$/s)		
n	Beta	0.362	0.245	0	0.98
C_{cr}	Normal	0.90 (mass-% by binder)	0.15(mass-% by binder)		
C_s	Normal	7.758 (for A_{cs}) 0 (for ε_{cs}) (weight-% by binder)	1.36 (for A_{cs}) 0.405 (for ε_{cs}) (weight-% by binder)		

value of $d_i^{j'}$. Fig. 23 shows the close views for Sections 1-1 (left) and 2-2 (middle), as well as the quarter column section (right) for these two sections. We assume the cracks will propagate radially toward the cover surface from reinforcing bars considering confinement effect of the column section. Three types of concrete cover are subject to corrosion-induced cracking, e.g., Cover 1 (hatched with inclined lines), Cover 2 (hatched with inclined lines and triangles), Cover 3 (hatched densely with inclined lines). The remaining concrete not hatched is not susceptible to corrosion effect. Fig. 23 also shows three types of reinforcing steel: the stirrups, the corner bars located at the four corners of the column section, and the longitudinal bars located within the stirrups, as shown in Section 2-2 in the middle in this figure. In both section types, the minimum values for clear cover thickness are: 25.4 mm (1 in.) for the stirrups, 58.2 mm (2.3 in.) for the corner bars, 50.8 cm (2 in.) for the longitudinal bars located under Cover 2, and

127.0 mm (5.0 in.) for the longitudinal bars located under Cover 3, as shown in the quarter column section at the right in this figure. Thus, Cover 1 will have the same se cant stiffness since all corner bars have the same clear cover thickness of 58.2 mm. The secant stiffness of Cover 2 is determined by cracking induced by the corrosion in the bar with clear cover of 50.8 mm at the bottom. The secant stiffness of Cover 3 is determined by cracking induced by the corrosion in the bar with clear cover thickness of 127 mm on the top. After the cover completely cracks, the secant stiffness of the cracked concrete is assumed to be constant.

Consideration of $T_{corr,i}$ for the reinforcing steel in corroded RC columns

For the reinforcing bars in different sections of the same column, we assume that general corrosion is initiated at the same time in every section of the column. To reduce the number of random variables, we further assume that, for any rebar j with the same d_i^j in Column i, the probability distributions for $T_{corr,1}^j$, $T_{corr,2}^j$, …, $T_{corr,22}^j$ are identical. To estimate the PDF of $T_{corr,i}^j$, Monte Carlo simulations are used to generate random variables to simulate $T_{corr,i}^j$ using Eq. (42) for rebar j in Column i.

The left chart in Fig. 24 shows an example histogram for $T_{corr,1}^j$ less than 100 years of interest for longitudinal bar j. The fitting of CDF are shown in the right chart, where the empirical probabilities (denoted along the abscissa) are compared with the fitted CDF's (denoted along the ordinate). The solid line denotes the 1:1 line for a perfect fitting of CDF. Four probability distribution models are selected as candidates:

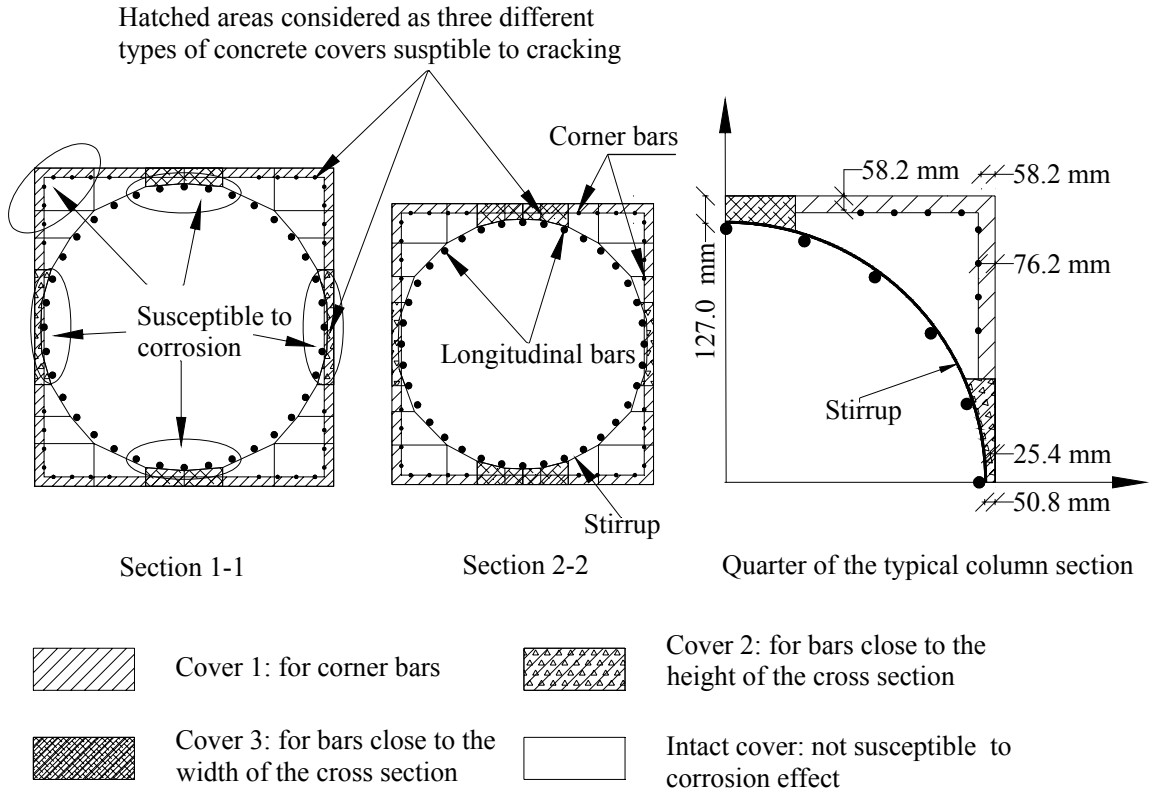

Fig. 23. Reinforcing bars and the corresponding concrete cover for the typical column cross-sections used in the modified I-880

Weibull (dash line), Gamma (dash-dotted line), Lognormal (LN) with 2 parameters (mean $\mu_{T^j_{corr,1}}$ and standard deviation $\sigma_{T^j_{corr,1}}$ for $T^j_{corr,1}$) (LN2) (dotted line), and LN with 3 parameters ($\mu_{T^j_{corr,1}}, \sigma_{T^j_{corr,1}}$, and threshold value, $T^{j,0}_{corr,1}$, for $T^j_{corr,1}$) (LN3) (bold-solid line), i.e., $(T^j_{corr,1} - T^{j,0}_{corr,1})$ is a Lognormal random variable with mean $\mu_{T^j_{corr,1}}$ and standard

deviation $\sigma_{T^j_{corr,1}}$. From the right chart, we can see LN3 has the best potential to represent the probability distribution of $T^j_{corr,1}$.

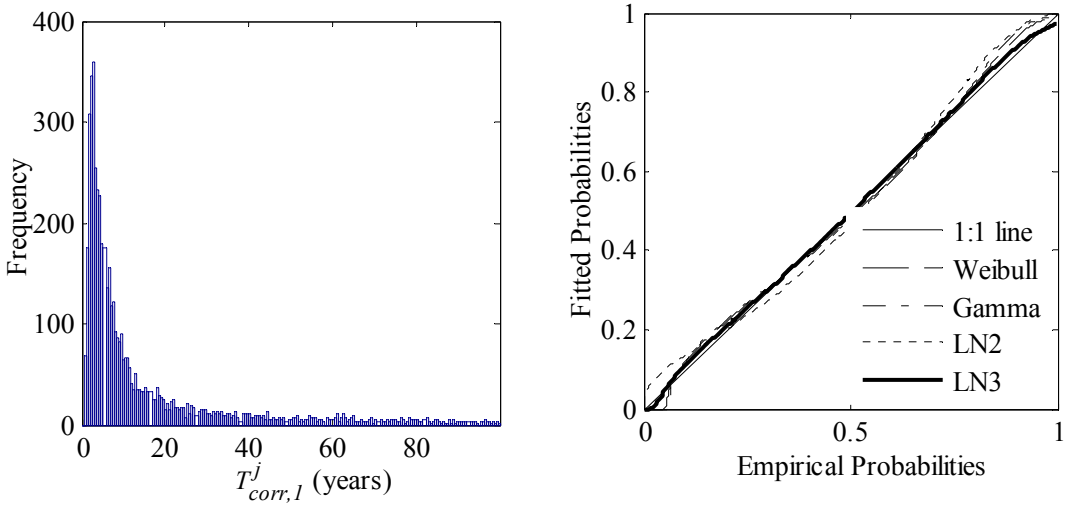

Fig. 24. Histogram (left chart) and fitted CDF (right chart) of $T^j_{corr,1}$

Table 14 lists the values of $\hat{T}^j_{corr,1}$, $\mu_{T^j_{corr,1}}$, $\sigma_{T^j_{corr,1}}$, and $T^{j,0}_{corr,1}$ for Lognormal random variable $(T^j_{corr,1} - T^{j,0}_{corr,1})$ on the left columns for the corner bars, longitudinal bars, and stirrup, shown in Fig. 25. Note two bars are bundled together in the actual column section. Here, $\hat{T}^j_{corr,1}$ is the point estimate computed using the mean values of all related random variables. Ten thousand random samples are generated to estimate parameters $\mu_{T^j_{corr,1}}$, $\sigma_{T^j_{corr,1}}$, and $T^{j,0}_{corr,1}$, respectively, in Monte Carlo simulations. We can see that the mean of $T^j_{corr,1}$ increases with the increasing minimum value of d^j_1. The point estimates,

however, are different from $\mu_{T^j_{corr,1}}$. The values of $\mu_{T^j_{corr,1}}$, $\sigma_{T^j_{corr,1}}$, and $T^{j,0}_{corr,1}$ are not shown for the cases where $\hat{T}^j_{corr,1} > 100$ since we only consider a 100-year period.

Table 14. Statistics for $T^j_{corr,1}$ of reinforcing bars in quarter section of Column 1

Cover types	Rebar j	Min. d_1^j (mm)	$T^j_{corr,1}$ (years)			
			$\hat{T}^j_{corr,1}$	$\mu_{T^j_{corr,1}}$	$\sigma_{T^j_{corr,1}}$	$T^{j,0}_{corr,1}$
--	Stirrup	25.4	0.8	2.3	8.1	0.2
1	Corner bar	58.2	16.7	17.4	42.9	1.3
2	1	50.8	6.6	11.9	42.4	0.9
	2	106.9	68.3	25.1	39.6	2.4
3	6	127.0	117.0	--	--	--
Intact cover	3	269.8	1242.6	--	--	--
	4	346.0	2709.8	--	--	--
	5	183.1	368.7	--	--	--

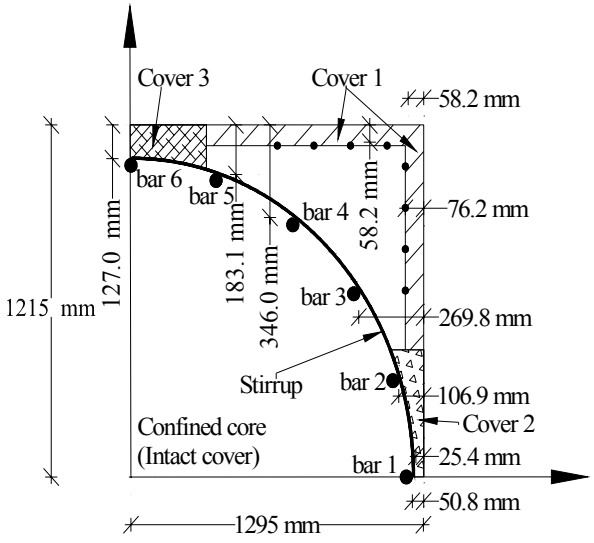

Fig. 25. Quarter section of Section 1-1 for Column 1

Fragility estimates for the modified I-880

Fragility estimates for column and bent

Fig. 26 shows the median predictions for the normalized capacities for Columns 1 and 21 (in the top charts) and the normalized demands for Column 1 (in the bottom charts) within 100 years. In the top charts, the solid lines indicate the column capacities with pristine (undamaged) cover, while the dash lines denote the column capacities with cracked concrete cover. The first change in the deformation capacities for both columns is due to the cracking of Cover 2, while the second change is initiated by the cracking of Cover 1. The bars under Cover 3 are not subject to corrosion within 100 years under consideration since $\hat{T}^{j}_{corr,1} > 100$ years for bars 3 and 6 as listed in Table 14. The top charts show the decreasing deformation and shear capacities with the corrosion process. Particularly, in the top-left chart, one can see that the median predictions for deformation capacity change only marginally for pristine and cracked covers. For the median predictions of deformation capacity, up to 0.6% of deformation capacity for Column 1 and 0.5% for Column 21, respectively, are overestimated when pristine concrete cover is used. In the top-right chart, the shear capacity is not affected by the type of cover considered. The bottom charts show the demand values predicted with PGV/PGA=0.19 sec. and S_a =2.04 g and 3.99 g (with bridge fundamental period of 1.21 sec.), respectively, for Column 1. In particular, the close views in the bottom-left chart shows the increased demand indicating the cracking in Cover 2 at year 7.0. The second increase shows the cracking in Cover 1 at year 18.2. It is noted that there is a marginal increase (up to 0.01% for both S_a =2.04 g and S_a =3.99 g) in the deformation

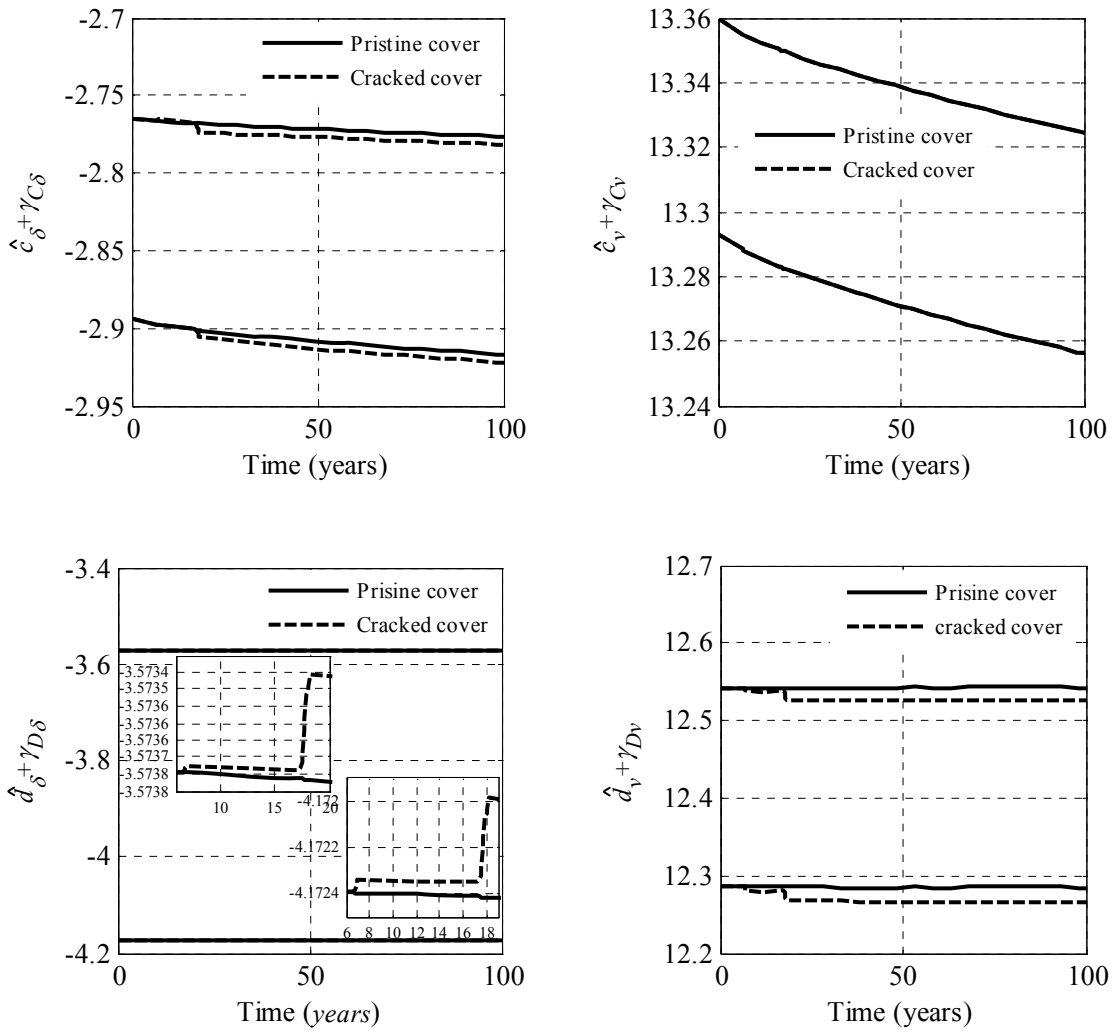

Fig. 26. Median predictions for capacities (top charts) and demands (with PGV/PGA=0.19 sec. and S_a =2.04 g and 3.99 g (bottom charts) for column with pristine and cracked concrete covers

demands when Covers 1 and 2 completely cracked in Column 1. In the bottom-right chart, the decreases in shear demand are more appreciable (up to 0.13% for S_a =2.04 g and 0.14% for S_a =3.99 g) when Covers 1 and 2 cracked. From the left charts, we can see the deformation capacity is overestimated while the deformation demand is

underestimated for the pristine cover used. From the right charts, we can see that only the shear demand is overestimated when the pristine cover is used. Similar observations can be made for other columns.

Fig. 27 shows the contour plots for the fragility surface estimates in column and bent levels at year 25 using pristine and cracked covers. The top-left chart shows the contour plots for the fragility surface estimates for deformation mode of failure in Column 1. The solid lines show the fragility estimates for Column 1 with pristine cover, while the dash lines show the fragility estimates with cracked cover. The seismic fragility is slightly underestimated for deformation when the pristine cover is used for Column 1. The top-right chart shows the corresponding contour plots for the shear fragility surface. Consistent with what we have observed in Fig. 26, the deformation fragility is now underestimated, while the shear fragility is overestimated using the pristine cover. From the top charts, it is seen that the deformation mode dominates the failure of this column. The bottom-left chart shows the fragility for the deformation or shear mode of failure of Column 1. The column fragility is slightly overestimated when the pristine cover is used. The bottom-right chart shows the fragility estimates for the deformation mode of Bent 1. Comparing these two bottom charts, it is interesting to observe that the fragility of this column in either deformation or shear mode is more predominant in high failure probabilities than that of the bent in the failure mode of deformation. This is because of the similarity between the deformation modes of two

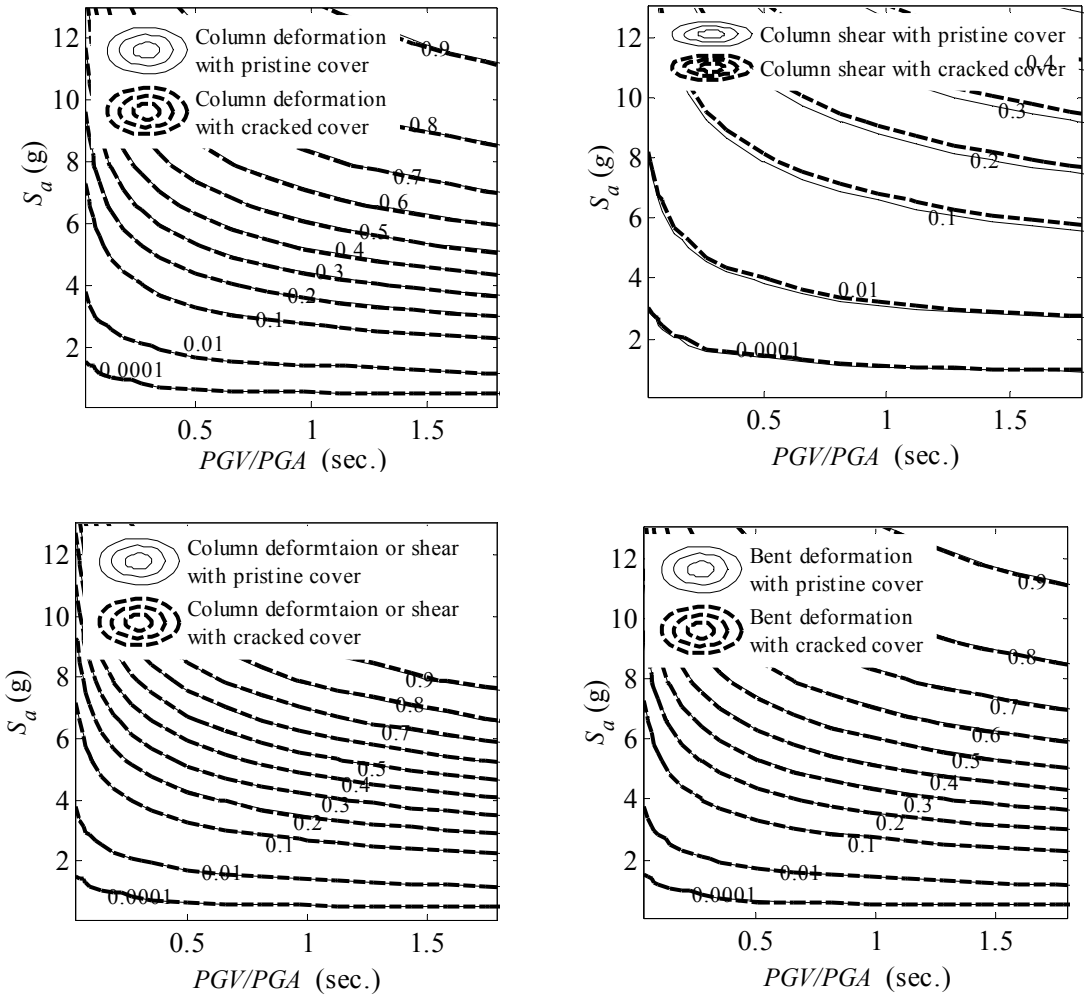

Fig. 27. Seismic fragility estimates for the deformation (top-left chart), shear (top -right chart), and deformation and shear (bottom-left chart) for Column 1 in Bent 1 and deformation fragility estimates for Bent 1 (bottom-right chart) considering pristine and cracked cover concrete at year 25

columns in the same bent (Zhong et al. 2008a). The shear fragility for Bent 1 in is similar to the column shear fragility and thus not presented here. Similar observations

can be also made for other columns. In the next, we consider the cracked cover for all corroded RC columns in the application.

Fig. 28 shows the contour plots for predictive and point estimates of fragility surface for the corroded Column 1 at 25 years. In particular, the mean estimates of $\boldsymbol{T}_{corr,1}$ are used in the point estimates. The left chart shows the contour plots for the fragility surface estimates for deformation mode of failure. The bold dash-dotted lines denote the point estimates of fragility. The dotted lines denote the predictive estimates of fragility. The right chart shows the corresponding fragility estimates for the shear mode of failure for the same column. In both charts, the surfaces from predictive estimates are flatter than the ones from point estimates because of more uncertainty incorporated in the predictive estimates. However, these differences are only marginal. Similar observations are valid for other columns. In the next, we use point estimates for the seismic fragility of the bridge.

Fragility estimates for modified I-880

Fig. 29 shows the fragility curves for the failure mode of deformation (dotted lines), shear (dash lines), and deformation or shear (solid lines) when PGV/PGA=0.19 sec. at years 0 and 100. The thin lines are used to denote the fragility at year 0, while the bold lines are used for the fragility at year 100. As seen from this figure, the fragility estimates are higher in year 100 than the ones in year 0 in all modes of failure. In particular, as we can see from the close view, the deformation and shear fragility curves intersect with each other at failure probability of 0.54 for year 0 and 0.59 for year 100, respectively. The shear mode of failure dominates the bridge failure below

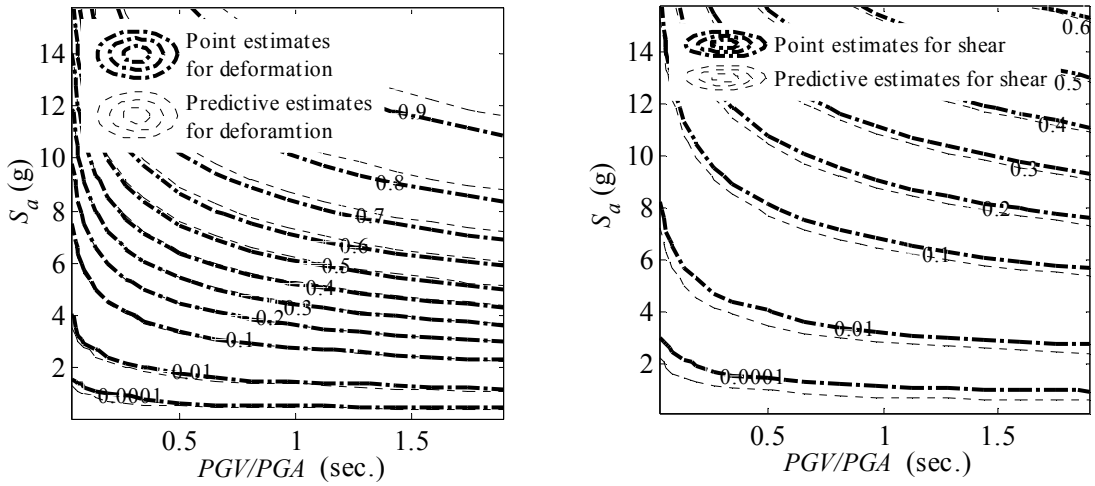

Fig. 28. Predictive and point fragility estimates for deformation (left chart) and shear (right chart) for Column 1 with cracked concrete cover at year 25

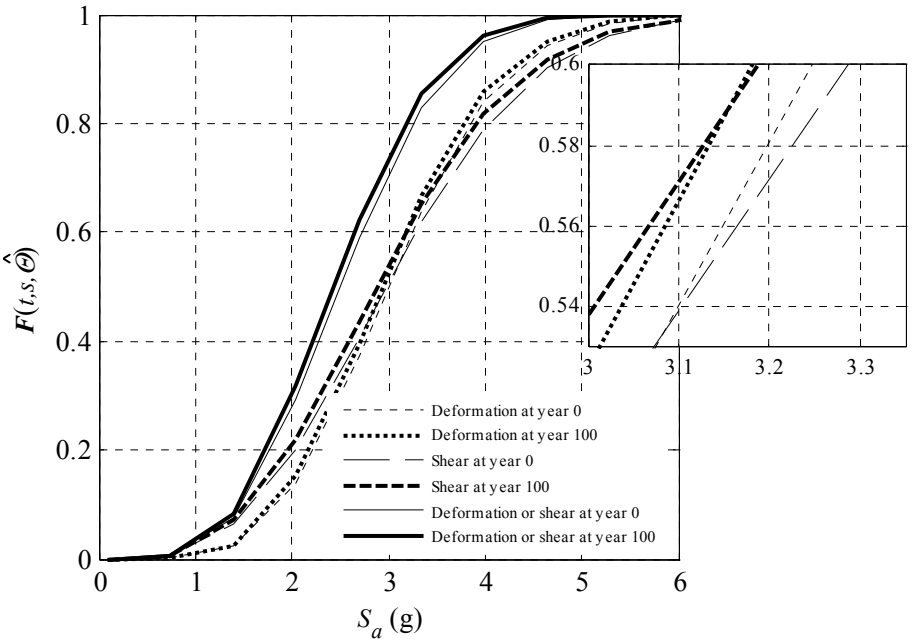

Fig. 29. Seismic fragility estimates for the entire corroded RC bridge at 0 and 100 years with PGV/PGA=0.19 sec. for failure mode of in deformation, shear, and deformation or shear

the intersecting points, while the fragilities of deformation mode of failure become comparable to the shear mode of failure above the intersecting points.

The contours for the fragility surface estimates for the entire RC bridge with corroded RC columns at years 0 and 100 are shown in Fig. 30. Monte Carlo simulations are used to evaluate Eq. (15). The stopping criterion is set at 0.2% of coefficient of variation of the failure probability. The top charts show the contours of the fragility surfaces for the deformation (thin-dotted lines) and shear (bold-dash lines) mode of failure for the bridge at years 0 and 100, respectively. From both charts, one can see that the shear mode of failure dominates the failure of the corroded bridge in low failure probability. However, in high failure probability, the deformation mode of failure and the shear mode of failure are comparable. In the bottom charts, we can see that the fragility estimates of bridge in failure mode of deformation or shear only change marginally comparing to the shear fragility estimates of the bridge in low failure probability at both 0 and 100 years. Fig. 31 shows the seismic fragility curves estimated for deformation (top-left), shear (top-right), deformation or shear (bottom-left), and three modes of failure (bottom-right) at 0, 25, 50, 75, and 100 years with PGV/PGA=0.19 sec. The top-left chart shows the deformation fragility using dotted lines at year 0, dash lines at year 25, dash-dotted lines at year 50, thin-solid lines at year 75, and bold-solid lines at year 100. The deformation fragility increases with time, shown in the close-view in the top-left chart. This is mainly because the loss of reinforcing steel continuously reduces the capacity and the minor increase in the deformation demands. The top-right chart shows the corresponding plots for shear

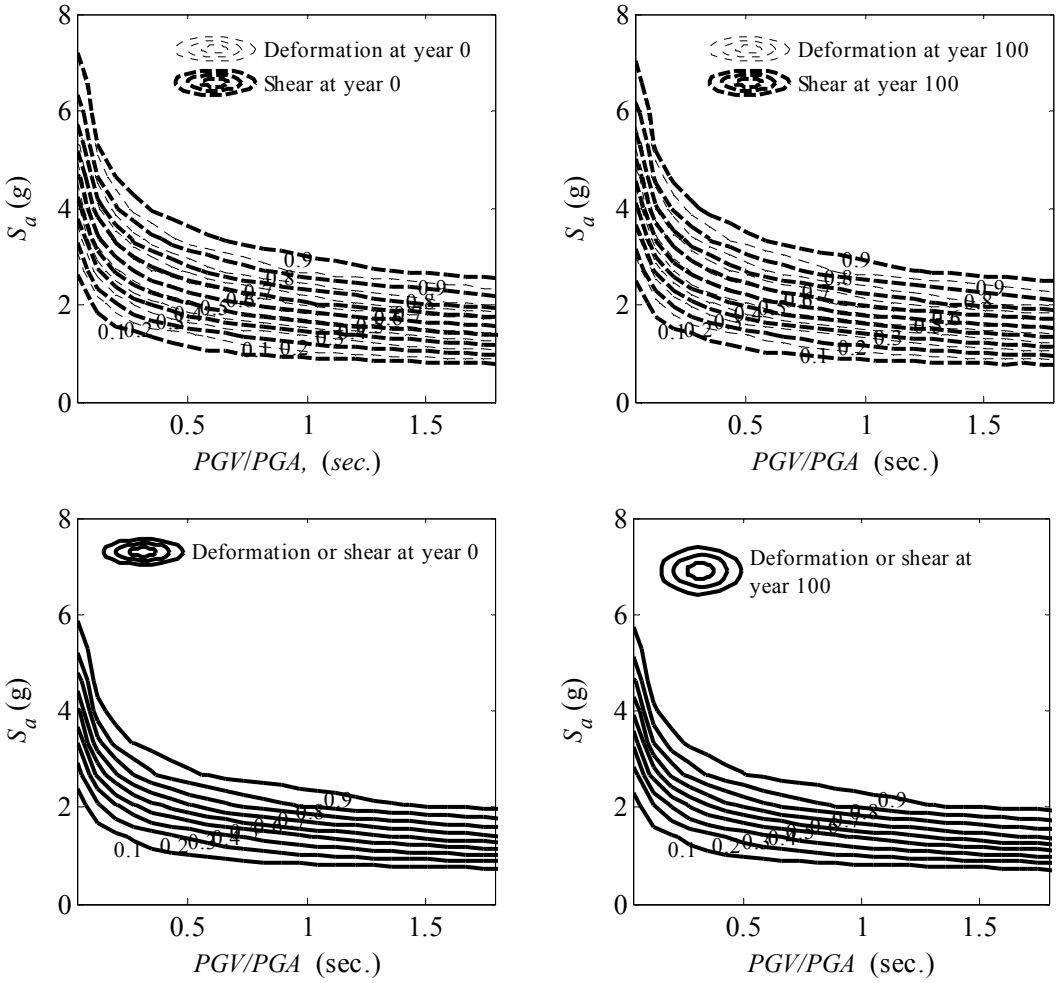

Fig. 30. Seismic fragility estimates for the entire corroded RC bridge: deformation and shear respectively (top chart); deformation or shear (bottom chart) with cracked cover concrete at years 0 and 100

fragility. Shear mode becomes less vulnerable at years 25 and 50 than at year 0. This is because the shear demands decrease faster caused by the cracking in covers than the decrease of the shear capacity caused by the loss of reinforcing steel in years 25 and 50. Then shear fragility increases from years 50 to 100. The same line types are also applied to the fragility estimates for deformation or shear mode of failure shown in the bottom-

left chart, where the legends are not shown. Two close views for low (<0.18, close view at the bottom-right) and high (>0.49, close view on the top-left) failure probabilities are also shown for this chart. The fragility estimates at year 25 are still the smallest. This means the cracking in concrete cover has reduced

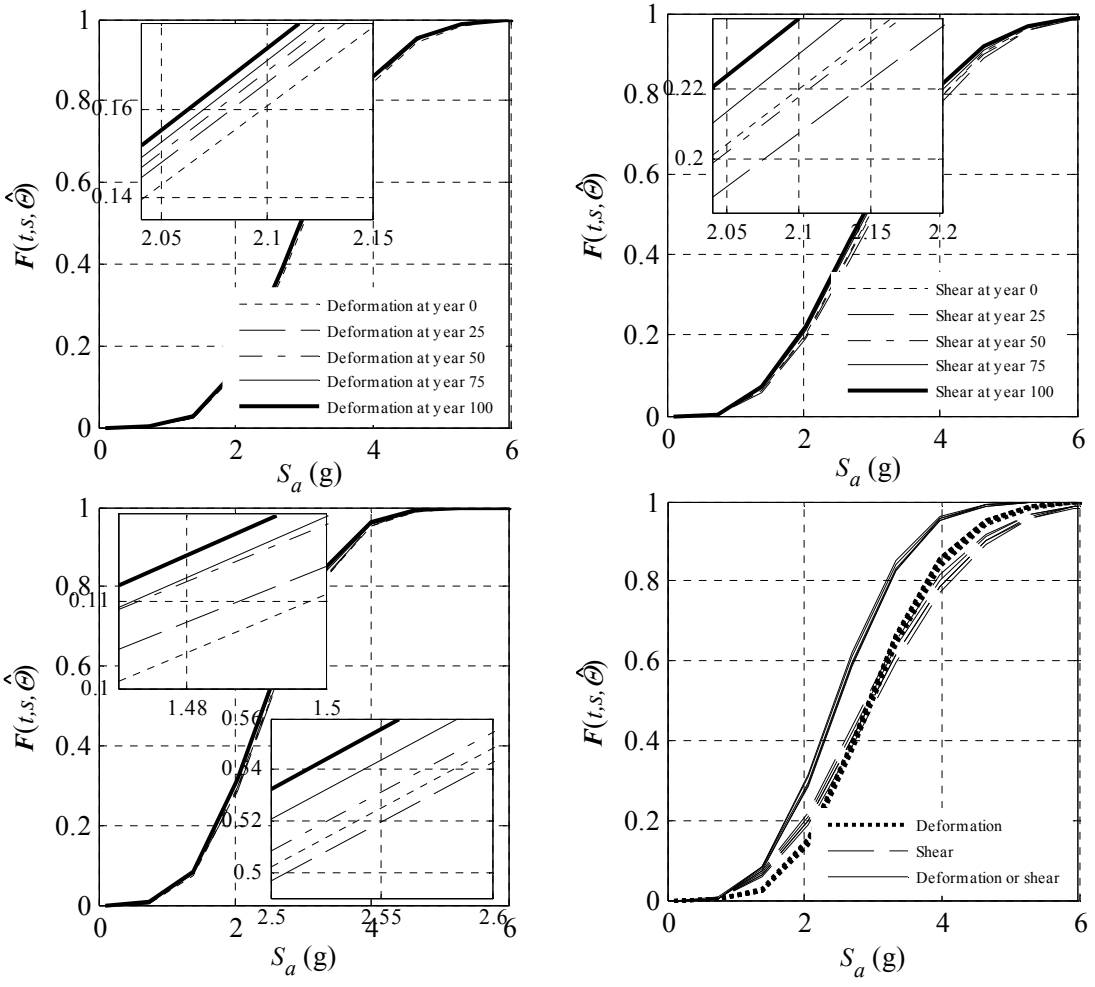

Fig. 31. Seismic fragility estimates for the entire corroded RC bridge over 100 years with PGV/PGA=0.19 sec. for the failure modes in deformation, shear, and deformation or shear

the seismic demands at the early age of this corroded bridge. As the loss of reinforcing steel increases, the fragility of the bridge increases with time. In the bottom-right chart, the bold dotted-, dashed-, and solid- lines are used to represent the fragility estimates for deformation, shear and either of them, respectively. The shear mode of failure dominates the failure of the bridge in low failure probabilities (below about 0.43), while the deformation mode of failure are comparable to the shear mode of failure of the bridge in high (above about 0.53) failure probabilities.

Fig. 32 shows the change of fragility estimates for the corroding RC bridge for every 5-year interval within 100 years with seismic intensities of PGV/PGA=0.19 sec. and S_a =2.04 g in the left chart, and S_a =3.99 g and in the right chart. In the left chart, the dotted line denotes the deformation fragility, which increases monotonically as a function of time because of capacity reduction and marginal increase in demands. The dash line denotes the shear fragility with a different pattern. The shear fragility increases at the beginning since the corrosion has been initiated in the stirrup at the very beginning (0.8 years as listed in Table 14). Then this fragility curve is reshaped by two time periods at which the Covers 1 and 2 completely crack at years 7.0 and 18.2, respectively. At each of these time periods, there is a decrease of the shear fragility caused by the stiffness reduction in corroded RC columns. After these two time periods, the shear fragility increases with time because of the loss of shear capacity. The fragility estimate for deformation or shear mode of failure is similar to the shear fragility estimates since the shear mode dominates the failure of bridge in low failure probabilities. The right chart shows similar results with higher seismic intensities. Similar observations still

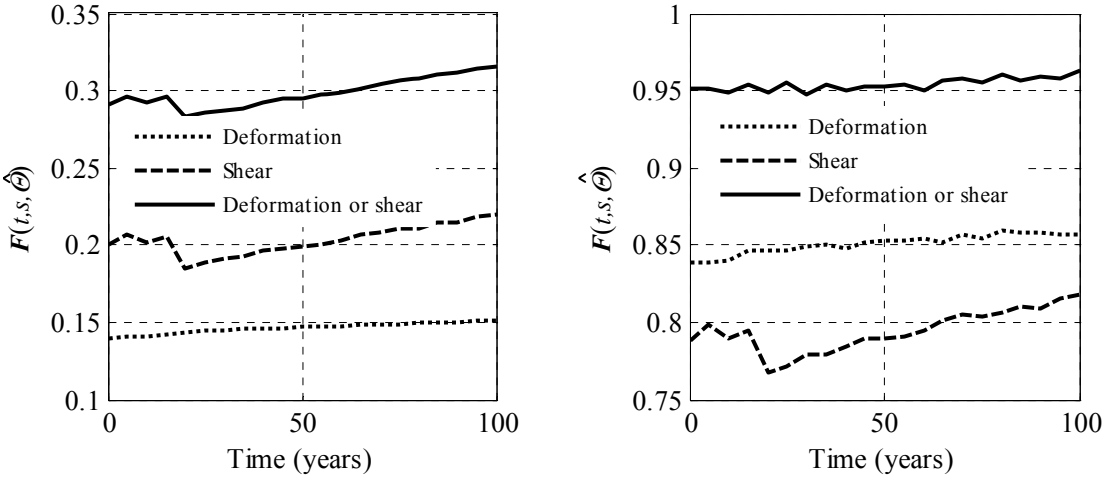

Fig. 32. Seismic fragility estimates for the corroded RC bridge over 100 years with PGV/PGA =0.19 sec. (S_a =2.04 g in the top chart and S_a =3.99 g in the bottom chart) for the failure modes in deformation, shear, and deformation or shear

apply to the fragility estimates for deformation and shear modes of failure. In this chart, however, the decrease of fragility estimates for failure mode of deformation or shear is less sensitive to the cracking of concrete covers since the deformation mode now has higher influence on the failure of the bridge.

SUMMARY

This chapter proposed a method to estimate the seismic fragility for corroded RC bridges with two-column bents. Deformation and shear capacities of columns are estimated using the probabilistic models. The corresponding probabilistic demand models are used to estimate the seismic demands on the RC columns in terms of seismic intensities spectral acceleration (S_a) and the ratio between the peak ground velocity (PGV) and the

peak ground acceleration (*PGA*), *PGV*/*PGA*. The unbiased capacity and demand models are then combined with the probabilistic models for chloride-induced corrosion and a time-dependent corrosion rate to account for the variation of capacity and demand over time. Comparing to the existing studies, the loss of reinforcing steel is particularly estimated for individual reinforcing bars. The degraded stiffness of concrete cover is properly considered in the capacity and demand models. Fragility functions are formulated in the column, bent, and bridge levels. The fragility formulation incorporates the uncertainties in the parameters of capacity and demand models, and the inexactness (or model error) in modeling the material deterioration, structural capacity, and seismic demands.

This proposed method is illustrated by the numerical computations on an example corroded RC bridge with 11 two-column bents. The time to corrosion initiation for reinforcing bars can be modeled as the lognormal random variables within 100 *years* of interest. On the column level, the uncertainty of time to corrosion initiation for reinforcing steel only has marginal effects on the seismic fragility of corroded RC columns. The differences between predictive and point fragility estimates are also marginal. The effect of cover cracking has minor effect on the median predictions of column capacity and demand. On the bent level, the deformation or shear seismic fragility is similar to the deformation or shear fragility of the column in the same bent. On the bridge level, the shear mode dominates the failure of the bridge in low failure probabilities, while the deformation mode of failure becomes comparable to shear mode of failure in high failure probabilities.

CHAPTER VI

CONCLUSIONS AND FUTURE RESEARCH

CONCLUSIONS

This research proposed a methodology to estimate the seismic fragility of corroded RC bridges with two-column bents. Probabilistic seismic models are first developed for RC bridges with two-column bents. All available information from science/engineering laws, numerical analysis, laboratory experiments, and field measurements has been used to construct the proper forms of the probabilistic demand models and the fragility functions. The probabilistic capacity and demand models are then combined with the probabilistic models for chloride-induced corrosion and the time-dependent corrosion rate. Seismic fragility functions are expressed in terms of variation models over time for capacity and demand that engineers can evaluate using available tools. The fragility estimation incorporates the uncertainties in the parameters of capacity and demand models, and the inexactness (or model error) in modeling the material deterioration, structural capacity, and seismic demands. Although the seismic demand models are developed only for RC bridges with two-column bents, however, for other multicolumn bent configurations, such as three-column bents, the develop demand models can be used for the preliminary estimation. This is because of the similarity of the capacity and demand in the RC columns in multicolumn bent configurations.

The following conclusions are made with regard to the probabilistic demand models for RC bridges with two-column bents:

- The spectral acceleration at the natural period of the structure and ratio between the peak ground velocity and the peak ground acceleration are selected as the most relevant ground motion parameters for seismic demands;
- The fragility estimates of a bent are similar to the fragility estimates of an individual column in that bent since the deformation and shear demands in both columns of the same bent are highly correlated.

The following conclusions are made with regard to the fragility estimates for RC bridges with two-column bents:

- For practical purposes, point estimates provide accurate estimates of the fragility surfaces. Neglecting the epistemic uncertainty in the model parameters leads only to a marginal difference in the tails of the fragility surfaces.
- The fragility estimates are more sensitive to changes in S_a than in PGV / PGA.

The following conclusions are made with regard to the time to cracking of concrete cover and stiffness degradation of cracked concrete:

- The cracking progress weakens the stiffness of cracked concrete as the crack front approaches the surface of the RC structure;
- The proposed stiffness degradation factor provides an effective means to model the stiffness degradation and to estimate the time to cracking of cracked concrete based on the change of energy in a fracturing RC structure.

The following conclusions are made with regard to seismic fragility estimates of corroded RC bridges with two-column bents:

- On the column level, the uncertainty of time to corrosion initiation for reinforcing steel only has marginal effects on the seismic fragility of corroded RC columns;
- The cracking of concrete cover has marginal effect on the fragility estimation of corroded RC bridges;
- The corrosion in reinforcing steel continues weakening the capacity of RC bridges with two-column bents. The seismic fragility of corroded RC bridges increases with corrosion in reinforcing steel.

LIMITATIONS OF CURRENT WORK

The probabilistic demand models of deformation and shear developed in this study are only applicable for the seismic fragility estimation for RC bridges with two-columns subject to seismic excitation. The near-field effects of ground motions are not considered in the model development. Thus the above conclusions are only applicable for the RC bridges with two-column bents subject to far-field ground shaking.

To estimate the RC bridges with other multicolumn bent configurations, the developed demand models should be applied with caution. Due to the lack of experiment data on the seismic demands for RC bridges with multicolumn bents, the preliminary estimation of seismic demands should be verified with the experimental data, either from the laboratory or from numerical simulations.

FUTURE RESEARCH

When structures are built in certain region subject to seismic hazards from multiple seismic sources, it is important to incorporate all potential hazards into the fragility estimation based on appropriate seismic intensities. Two of the most effective candidates for the seismic intensities are the moment magnitudes, **M**, and the epicenter-to-site distances, **R**, of the earthquakes. In the future, the followings two topics shall have broader potentials:

- Promote more effective seismic descriptors, **M** and **R,** to characterize the seismic hazard in the seismic region subject to multiple seismic sources;
- Develop a new methodology to incorporate the effects from near-field ground motions for the seismic fragility estimation.

REFERENCES

Ahmed, S.F.U., Maalej, M., and Mihashi, H. (2007). "Cover cracking of reinforced concrete beams due to corrosion of steel." *ACI Materials Journal,* 104(2), 153–161.

Aliabadi, M.H. (1997). "Boundary element formulations in fracture mechanics." *Applied Mechanics Reviews*, 50 (2), 83–96.

Aliabadi, M.H., and Saleh, A.L. (2002). "Fracture mechanics analysis of cracking in plain and reinforced concrete using the boundary element method." *Engineering Fracture Mechanics*, 69, 267-280.

Applied Technology Council (1996). "Improved seismic design criteria for California bridges." *Applied Technology Council Report ATC-32*, Palo Alto, CA.

Banerjee, M., and Shinozuka, M. (2007). "Nonlinear static procedure for seismic vulnerability assessment of bridges." *Computer-Aided Civil and Infrastructure Engineering*, 22(4), 293–305

Barenblatt, G.I. (1962). "The mathematical theory of equilibrium cracks formed in brittle fracture." *Advanced Applied Mechanics*, 7, 55–129.

Basöz, N., and Kiremidjian, A.S. (1996). "Risk assessment for highway transportation systems." *Technical Report No. 118*, John A. Blume Earthquake Engineering Center, Civil Engineering Department, Stanford University, Stanford, CA.

Basöz, N., and Kiremidjian, A.S. (1997a). "Evaluation of bridge damage data from the Loma Prieta and Northridge, CA earthquakes." *Technical Report No. 127*, John A. Blume

Earthquake Engineering Center, Civil Engineering Department, Stanford University, Stanford.

Basöz, N., and Kiremidjian, A.S. (1997b). "Risk assessment of bridges and highway systems from the Northridge earthquake." *Proceedings of the National Seismic Conference on Bridges and Highways: Progress in Research and Practice* Sacramento, CA, pp. 65–79.

Basöz, N., and Mander, J. (1999). "Enhancement of the highway transportation lifeline module in HAZUS." Final Pre-publication Draft (#7) prepared for the National Institute of Building Science, March 1, 1999: http://www.nibs.org/hazusweb/overview/pubs.php, accessed March 23, 2008.

Bažant, Z.P. (1979a). "Physical model for steel corrosion in concrete sea structures–theory." *Journal Structural Division*, ASCE, (June), 1137–1153.

Bažant, Z.P. (1979b). "Physical model for steel corrosion in concrete sea structures–applications." *Journal Structural Division*, ASCE, (June), 1155–1165.

Bažant, Z.P., and Li. Y.-N. (1995). "Stability of cohesive crack model: part I-Energy Principles." *Journal of Applied Mechanics*, 62, 959-964.

Bažant, Z. P., and Oh, B.H. (1984). ''Deformation of progressively cracking reinforced concrete beams." *ACI Journal Proceedings*, 81(3), 268–278.

Bažant, Z.P., and Planas. J. (1998). *Fracture and size effect in concrete and other quasibrittle materials*. CRC Press, Boca Raton, FL.

Bhargava, K., Ghosh, A.K., Mori, Y., and Ramanujam, S (2006). "Model for cover cracking due to rebar corrosion in RC structures." *Engineering Structures*, 28(8), 1093–1109.

Box, G.E.P. and Tiao, G.C. (1992). *Bayesian inference in statistical analysis*. Wiley, New York.

Cady, P.D., and Weyers, R.E. (1983). "Chloride penetration and the deterioration of concrete bridge decks." *Cement, Concrete & Aggregate*, 5(2), 81-87.

Cairns, J., Du, Y., and Law, D. (2008). "Structural performance of corrosion-damaged concrete beams." *Magazine of Concrete Research*, 60(5), 359-370.

California Department of Transportation (Caltrans) (1999). *Seismic design criteria*. *California Department of Transportation*, 1.1 Edition, Sacramento, CA

California Department of Transportation (Caltrans) (2006). *Seismic design criteria*. *California Department of Transportation*, 1.4 Edition, Sacramento, CA.

Capozucca, R. (2008). "Detection of damage due to corrosion in prestressed RC beams by static and dynamic tests." *Construction and Building Materials*, 22(5), 738-746.

Choe, D.E., Gardoni, P., and Rosowsky, D. (2007). "Closed-form fragility estimates, parameter sensitivity and Bayesian updating for RC columns." *Journal Engineering Mechanics*, ASCE, 133(7), 833-843

Choe, D., Gardoni, P., Rosowsky, D., and Haukaas, T. (2008a). "Seismic fragility estimates for reinforced concrete bridges subject to corrosion." *Structural Safety*, (Submitted)

Choe, D., Gardoni, P., Rosowsky, D., and Haukaas, T. (2008b). "Probabilistic capacity models and fragility estimates for corroding reinforced concrete columns." *Reliability Engineering and System Safety*, 93, 383-393.

Choi, E., DesRoches, R., and Nielson, B. (2004). "Seismic fragility of typical bridges in moderate seismic zones." *Engineering Structures*, 26(2):187-199.

Chopra, A. K., and Goel, R.K. (1999). "Capacity-demand-diagram methods for estimating seismic deformation of inelastic structures: SDF systems." *Report Number PEER-1999/02*, Pacific Earthquake Engineering Research Center, University of California, Berkeley.

Chopra, A. K., and Goel, R.K. (2002). "A model pushover analysis procedure for estimating seismic demands for buildings." *Earthquake Engineering and Structural Dynamics*, 31, 561–582.

Der Kiureghian, A., and Ke, J.-B., (1995). "Finite-element based reliability analysis of frame structures." *Proceedings of ICOSSAR '85, 4th International Conference on Structural Safety and Reliability*, Kobe, Japan, 1, 395-404.

DuraCrete (2000). "Statistical quantification of the variables in the limit state functions." *Report no. BE95-1347/R9*, The European Union-Brite EuRam III Document, Gouda, Brussels, Belgium

Enright, M.P., and Frangopol, D.M. (1998a). "Probabilistic analysis of resistance degradation of reinforced concrete bridge beams under corrosion." *Engineering Structures*, 20(11), 960–71.

Enright, M.P., and Frangopol, D.M. (1998b). "Service-life prediction of deteriorating concrete bridges." *Journal of Structural Engineering*, ASCE, 124(3), 309–17.

Fajfar, P. (2000). "A nonlinear analysis method for performance-based seismic design." *Earthquake Spectra*, 16(3), 573-592.

Fajfar, P., and Fischinger, M. (1987). "Non-linear seismic analysis of RC buildings: implications of a case study." *European Earthquake Engineering*, 1, 31-43.

Fajfar, P., and Fischinger, M. (1988). "N2 – a method for non-linear seismic analysis of regular buildings." *Proceedings of the 9th World Conference on Earthquake Engineering*, August, Tokyo-Kyoto, Japan, V: 111-116.

Fajfar, P., Gašperšič, P., and Drobnič, D. (1997). "A simplified nonlinear method for seismic damage analysis of structures." *Seismic design methodologies for the next generation of codes*, Fajfar, P. and Krawinkler, H. (Eds), Balkema, Rotterdam, The Netherlands, pp. 183-194.

Federal Emergency Management Agency (FEMA), NEHRP (1997). "Commentary on the guidelines for the seismic rehabilitation of buildings." *FEMA 274*, Washington, DC.

Fett, T., and Munz, D. (1997). *Stress intensity factors and weight functions*. CMP, Southampton, U.K.

Floegl, H., and Mang, M. (1982). "Tension stiffening concept based on bond slip." *Journal of Structural Division*, ASCE, 108(12), 2681–2701.

Hwang, H., and Jaw, J. W., (1990). "Probabilistic damage analysis of structures." *Journal of Structural Engineering*, ASCE, 116(7), 1992-2007.

Gardoni, P., Der Kiureghian, A., and Mosalam, K.M. (2002). "Probabilistic capacity models and fragility estimates for RC columns based on experimental observations." *Journal of Engineering Mechanics*, ASCE, 128(10), 1024-1038.

Gardoni, P., Khalid, M.M., and Der Kiureghian, A. (2003). "Probabilistic seismic demand models and fragility estimates for RC bridges." *Journal of Earthquake Engineering*, 7 (Sp. Issue 1), 79-106.

Gulkan, P., and Sozen, M., (1971). "Response and energy dissipation of reinforced concrete frames subject to strong base motions." *Report UILU-ENG-71-2013*, University of Illinois, Urbana.

Guo, Y.H., and Padovan, J. (1994). "Moving template analysis of crack growth—II. multiple crack extension and benchmarking." *Engineering Fracture Mechanics*, 48 (3), 427–444.

Hachem, M., and Mahin, S., (1999). "Bidirectional seismic response of reinforced concrete bridges." *PEER center news*, Pacific Earthquake Engineering Research Center, 2(3), 1-5.

Haukaas, T., and Der Kiureghian, A. (2004). "Finite element reliability and sensitivity methods for performance-based earthquake engineering." *Report No. PEER 2003/14, Pacific Earthquake Engineering Research Center*, University of California, Berkeley.

Hillerborg, A., Modeer, M., and Petersson, P.E. (1976). "Analysis of crack formation and crack growth in concrete by means of fracture mechanics and finite elements." *Cement Concrete Research*, 6, 773-782.

Hohenbichler, M., and Rackwitz, R. (1986). "Sensitivity and importance measures in structural reliability." *Civil Engineering Systems*, 3, 203-209.

Ingraffea, A.R., Gerstle, W.H., Gergely, P., and Saouma, V. (1984). "Fracture mechanics of bond in reinforced concrete." *Journal of Structural Engineering*, ASCE, 110(4), 871-890.

Jeong, S.-H., and Elnashai, A.-S. (2007). "Probabilistic fragility analysis parameterized by fundamental response quantities." *Engineering Structures*, 29, 1238–1251.

Johnson, N. (2006). "Large-scale experimental and analytical seismic studies of a two-span reinforced concrete bridge system." *Ph.D. Dissertation*, University of Nevada, Reno.

Karim, K.R., and Yamazaki, F. (2001). "Effect of earthquake ground motions on fragility curves of highway bridge piers based on numerical simulation." *Earthquake Engineering and Structural Dynamics*, 30, 1839–1856.

Karim, K.R., and Yamazaki, F. (2003). "A simplified method of constructing fragility curves for highway bridges." *Earthquake Engineering and Structural Dynamics*, 32, 1603–1626.

Kim, S.-H., and Feng, M.Q. (2003). "Fragility analysis of bridges under ground motion with spatial variation." *International Journal of Non-Linear Mechanics*, 38, 705–721.

Kim, S.-H., and Shinozuka, M. (2004). "Development of fragility curves of bridges retrofitted by column jacketing." *Probabilistic Engineering Mechanics*, 19, 105–112.

Klisinski, M., Runesson, K., and Sture, S. (1991). "Finite element with inner softening band." *Journal of Engineering Mechanics*, ASCE, 117(3), 575-587.

Kunnath, S.K. (2007). "Application of the PEER PBEE Methodology to the I-880 Viaduct." *Report No PEER 2006/10*, Pacific Earthquake Engineering Research Center, University of California, Berkeley.

Kunnath, S.K., El-Bhy, A., Taylor, A.W., and Stone, W.C. (1997). "Cumulative seismic damage of reinforced concrete bridge piers." *Technical report NISTIR 6075*, Building and Fire Research Laboratory, National Institute of Standards and Technology, Gaithersburg, MD.

Kunnath, S.K., Larson, L., and Miranda, E. (2006). "Modeling considerations in probabilistic performance-based seismic evaluation: case study of the I-880 viaduct." *Earthquake Engineering and Structural Dynamics*, 35, 57–75.

Laplace, P.N., Sanders, D.H., Saiidi, M.S., and Douglas, B. (1999). "Shake table testing of flexure dominated reinforced concrete bridge columns." *Report No. CCEER-99-13*, Department of Civil and Environmental Engineering, University of Nevada, Reno.

Leung, C.K.Y. (2001). "Modeling of concrete cracking induced by steel expansion." *Journal of Materials in Civil Engineering*, ASCE, 13(3), 169-175.

Li, C.Q., Melchers, R.E., and Zheng, J.J. (2006). "Analytical model for corrosion-induced crack width in reinforced concrete structures." *ACI Structural Journal*, 103(4), 479-487

Liu, Y. (1996). "Modeling the time-to-corrosion cracking of the cover concrete in chloride contaminated reinforced concrete structures." *Ph.D. Dissertation*, Virginia Tech, Blacksburg.

Liu, Y., and Weyers, R.E. (1998). "Modeling the time-to-corrosion cracking in chloride contaminated reinforced concrete structures." *ACI Materials Journal*, 95(6), 675–81.

Lu, Y., Gu, X., and Guan, J. (2005). "Probabilistic drift limits and performance evaluation of reinforced concrete columns." *Journal of Structural Engineering*, ASCE, 131(6), 966-978.

Lupoi, G., Franchin, P., Lupoi, A., and Pinto, P.E. (2006). "Seismic fragility analysis of structural systems." *Journal of Engineering Mechanics*, ASCE, 132(4), 385-395.

Maaddawy, T.E., and Soudki, K. (2007). "A model for prediction of time from corrosion initiation to corrosion cracking." *Cement and Concrete Composites*, 29, 168–75.

MacRae, G., Priestley, N., and Seible, F. (1994). "Shake table testing of flexural dominated reinforced concrete bridge columns." *Report No. SSRP-94/18*, Structural systems research project, University of California, San Diego.

Madsen, H.O., Krenk S., and Lind, N.C. (1986). *Methods of structural safety*. Prentice Hall, Englewood Cliffs, NJ.

Mander, J.B., and Basöz, N. (1999) "Seismic fragility curve theory for highway bridges." *Proceedings of the 5th U.S. Conference on Lifeline Earthquake Engineering*, Reston, VA, 31–40.

McKenna, F., Fenves, G.L., and Scott, M.H. (2002). "Open system for earthquake engineering simulation." Pacific Earthquake Engineering Research Center, University of California, Berkeley, http://opensees.berkeley.edu/, accessed October 1, 2005.

Mckie, K., and Stojadinovic, B. (2001) "Probabilistic seismic demand model for California highway bridges." *Journal of Bridge Engineering*, ASCE, 6(6), 468-481.

Melchers, R.E. (2003). "Mathematical modeling of the diffusion controlled phase in marine immersion corrosion of mild steel." *Corrosion Science*, 45(5), 923-940.

Molina, F.J., Alonso, C., and Andrade, C. (1993). "Cover cracking as a function of rebar corrosion: part 2—numerical model." *Materials and Structures*, 26, 532-548.

Monti, G., and Nistico, N. (2002). "Simple probability-based assessment of bridges under scenario earthquakes." *Journal of Bridge Engineering*, ASCE, 7(2), 104-114.

Moore, J.M. (2000). "Shake table testing of two-column bent with hinged bases." *M.S. Thesis*, Department of Civil and Environment Engineering, University of Nevada, Reno.

Morinaga, S. (1988). "Prediction of service lives of reinforced concrete buildings based on rate of corrosion of reinforcing steel." *Report No. 23*, Shimizu Corp, Tokyo, Japan, 82p.

Moustafa, K. (2004). "Impact of aspect ratio on two-column bent seismic performance." *Ph.D. Dissertation*, Department of Civil and Environment Engineering, University of Nevada, Reno.

Nada, H.M. (2003). "Seismic performance of RC bridge frames with architectural-flared columns." *Ph.D. Dissertation*, Department of Civil and Environment Engineering, University of Nevada, Reno.

Nelson, J.M., (2000). "Damage model calibration for reinforced concrete bridge columns." *M.S. Thesis*, Department of Civil and Environment Engineering, University of Washington, Seattle.

Noghabai, K. (1999). "Discrete versus smeared versus element-embedded crack models on ring problem." *Journal of Engineering Mechanics*, ASCE, 125(3), 307-315.

Ohtsu, M., and Yosimura, S. (1997). "Analysis of crack propagation and crack initiation due to corrosion of reinforcement." *Construction and Building Materials*, 11(7-8), 437-442.

Oller, S., and Barbat, A.H. (2006). "Moment-curvature damage model for bridges subjected to seismic loads." *Computational Methods and Applied Mechanics Engineering*, 195, 4490–4511.

Padgett, J. E., and DesRoches, R. (2007). "Sensitivity of response and fragility to parameter uncertainty." *Journal of Structural Engineering*, ASCE, 133(12), 1710-1718.

Padovan, J., and Guo, Y.H. (1994). "Moving template analysis of crack growth—I. procedure development." *Engineering Fracture Mechanics*, 48 (3), 405–425

Padovan, J., and Jae, J. (1997). "FE modeling of expansive oxide induced fracture of rebar reinforced concrete." *Engineering Fracture Mechanics*, 56, 797–812.

Pantazopoulou, S.J., and Papouli, K.D. (2001). "Modeling cover-cracking due to reinforcement corrosion in RC structures." *Journal of Engineering Mechanics*, ASCE, 127(4), 342-351.

Pantelides, C., Gergely, J., Reaveley, L., and Volyy, V. (1999). "Retrofit of reinforced concrete bridge piers with CFRP advanced composites." *Journal of Structural Engineering*, ASCE, 125(10), 1094-1099.

Rots, J. G. (1988). ''Computational modeling of concrete fracture." *Ph.D. Dissertation*, Delft University of Technology, Delft, The Netherlands.

Saiidi, M., Sanders, D., Gordaninejad, F., and Martinovic, F. (2000). "Seismic retrofit of non prismatic bridge columns with fibrous composites." *Proceedings of 12th World Conference on Earthquake Engineering*, February, Auckland, New Zealand.

Scanlon, A. (1975). "Time dependent deflections of reinforced concrete slabs." *Ph.D. Dissertation*, University of Alberta, Edmonton, Canada.

Sexsmith, R., Anderson, D., and English, D. (1997). "Cyclic behavior of concrete bridge bents." *ACI Structural Journal*, 94(2), 103-113.

Shinozuka, M., Feng,. M.Q., Kim, H.-K., and Kim, S.-H. (2000). "Nonlinear static procedure for fragility curve development." *Journal of Engineering Mechanics*, ASCE, 126(12), 1287-1295.

Somerville, P. and Collins, N. (2002). "Ground motion time histories for the I880 bridge, Oakland, prepared for the PEER methodology tested project." Pacific Earthquake Engineering Research Center, University of California, Berkeley, http://www.peertestbeds.net/i-880.htm, accessed October 15, 2005

Sritheran, S., Priestley, M.J.N., and Seible, F. (2001). "Seismic design and experimental verification of concrete multiple column bridge bents." *ACI Structural Journal*, 98(3), 335-346.

Stapleton, S.E., McDaniel, C.C., Cofer, W.F., and Mclean, D.I. (2005). "Performance of lightly confined reinforced concrete columns in long-duration subduction zone earthquakes." *Journal of the Transportation Research Board*, Washington, DC, 1928, 185-192.

Stewart, M.G. (2004). "Spatial variability of pitting corrosion and its influence on structural fragility and reliability of RC beams in flexure." *Structural Safety*, 26(4), 453–470.

Stewart, M.G., and Al-Harthyb, A. (2008). "Pitting corrosion and structural reliability of corroding RC structures: experimental data and probabilistic analysis." *Reliability Engineering and System Safety*, 93, 373–382.

Steward, M., and Rosowsky, D. (1998). "Structural safety and serviceability of concrete bridges subject to corrosion." *Journal of Infrastructure Systems*, ACSE, 4(4), 146-155.

Sureshkumar, K. (2004). "Seismic retrofit of two-column bents with diamond shape of columns." *M.S. Thesis*, Department of Civil and Environment Engineering, University of Nevada, Reno.

Tada, H., Paris, P.C., and Irwin, G.R. (2000). *The stress analysis of cracks handbook*. ASME International, New York.

Tastani, S., and Pantazopoulou, S.J. (2005). "Recovery of seismic resistance in corrosion-damaged reinforced concrete through FRP jacketing." *International Journal of Materials and Product Technology*, 23(3-4), 389-415.

Terayama, T., and Otsuka, H. (1996). "Seismic evaluation and retrofit of existing muti-column bents." *The Third US-Japan Workshop on Seismic Retrofit of Bridges*, December, Osaka, Japan, pp. 87-101.

Torres, L., Lopez-Almansa, F., and Bozzo, L.M. (2004). "Tension-stiffening model for cracked flexural concrete members." *Journal of Structural Engineering*, ASCE, 130(8), 1242-1251

Torres-Acosta, A.A. (1999). "Cracking induced by localized corrosion of reinforcement in chloride contaminated concrete." *Ph.D. Dissertation*, Department of Civil and Environmental Engineering, University of South Florida, Tampa.

Torres-Acosta, A.A., Fabela-Gallegos, M.J., Munoz-Noval, A., Vazquez-Vega, D., Hernandez-Jimenez, J.R., and Martinez-Madrid, M. (2004). "Influence of corrosion on the structural stiffness of reinforced concrete beams." *Corrosion*, 60(9), 962-872.

Trifunac, M. D., and Brady, A. G. (1975). "On the correlation of seismic intensity with peaks of recorded strong ground motion." *Bulletin of Seismology Society of America*, 65(1), 139-162.

Uddin, F.A.K.M., Shigeishi, M., and Ohtsu, M. (2004). "Fracture mechanics of corrosion cracking in concrete by acoustic emission." *Meccanica*, 41, 425–442.

Vidal, T., Castel, A., and François, R. (2007). "Corrosion process and structural performance of a 17 year old reinforced concrete beam stored in chloride environment." *Cement and Concrete Research*, 37(11), 1551-1561.

Vu, K.A.T., and Stewart, M.G. (2000). "Structural reliability of concrete bridges including improved chloride-induced corrosion models." *Structural Safety*, 22(4), 313–33.

Vu, K.A.T., Stewart, M.G., and Mullard, J. (2005). "Corrosion-induced cracking: experimental data and predictive models." *ACI Structural Journal*, 102(5), 719–26.

Wu, Z., Yoshikawa, H., and Tanabe, T. (1991). ''Tension-stiffness model for cracked reinforced concrete." *Journal of Structural Engineering*, ASCE, 117(3), 715–732.

Zhong, J., Gardoni, P., Rosowsky, D., and Haukaas, T. (2008a). "Probabilistic seismic demand models and fragility estimates for reinforced concrete bridges with two-column bents." *Journal Engineering Mechanics*, ASCE, 134(6), 495-504.

Zhong, J., Gardoni, P., and Rosowsky, D. (2008b). "Bayesian updating of seismic demand models and fragility estimates for reinforced concrete bridges with two-column bents." *Journal of Earthquake Engineering*, Accepted.

Zhong, J., Gardoni, P., and Rosowsky, D. (2008c). "Closed-form seismic fragility estimates, sensitivity analysis and importance measures for reinforced concrete two-column bents." *Structural Safety*, (Submitted).

Zhong, J., Gardoni, P., and Rosowsky, D. (2008d). "Stiffness degradation and time to cracking of cover concrete in reinforced concrete structures subject to corrosion effect." *Journal of Engineering Mechanics*, ASCE (Submitted).

Zhong, J., Gardoni, P., and Rosowsky, D. (2008e). "Seismic fragility estimates for corroded reinforced concrete bridges with two-column bents." *Journal of Structural Engineering*, ASCE (In preparation).

Zhao, Y.X., and Jin W.L. (2006). “Modeling the amount of steel corrosion at the cracking of concrete cover.” *Advance in Structural Engineering*, 9(5), 687–696.

APPENDIX A

Following Bažant and Planas (1998), the total strain, $\varepsilon(\xi,t)$, at time t and location ξ on a surface of the cohesive crack consists of an elastic component, $\varepsilon^{el}(\xi,t)$, and an actual cracking component, $\varepsilon^{f}(\xi,t)$, i.e.

$$\varepsilon\left(\xi,t\right)=\varepsilon^{el}\left(\xi,t\right)+\varepsilon^{f}\left(\xi,t\right)=\frac{\sigma\left(\xi\right)}{E_r}+\varepsilon^{f}\left(\xi,t\right) \tag{56}$$

Here the cohesive stress $\sigma(\xi)$ at location ξ is the stress on the unloading curve of the cracked concrete corresponding to $\varepsilon(\xi,t)$, as shown in the left chart in Fig. 17. Assuming there is no residual strain after complete unloading, we have

$$\varepsilon^{f}\left(\xi,t\right)=\frac{\varepsilon^{f}_{\max}\left(\xi,t\right)}{\phi\left[\varepsilon^{f}_{\max}\left(\xi,t\right)\right]}\sigma\left(\xi\right),\quad 0<\sigma\left(\xi\right)<\phi\left[\varepsilon^{f}_{\max}\left(\xi,t\right)\right] \tag{57}$$

then

$$\varepsilon\left(\xi,t\right)=\frac{\sigma\left(\xi\right)}{E_r}+\frac{\varepsilon^{f}_{\max}\left(\xi,t\right)}{\phi\left[\varepsilon^{f}_{\max}\left(\xi,t\right)\right]}\sigma\left(\xi\right) \tag{58}$$

On the other hand, the secant stiffness of the cracked concrete at location ξ and time t is defined using the stress and strain as

$$E_{\theta}\left(\xi,t\right)=\frac{\sigma\left(\xi\right)}{\varepsilon\left(\xi,t\right)} \tag{59}$$

and using the stiffness degradation factor as

$$E_\theta(\xi,t)=\eta(\xi,t)\cdot E_r \tag{60}$$

Therefore, we have

$$\varepsilon(\xi,t)=\frac{\sigma(\xi)}{\eta(\xi,t)E_r}=\frac{\sigma(\xi)}{E_r}+\frac{1}{E_r}\cdot\frac{1-\eta(\xi,t)}{\eta(\xi,t)}\sigma(\xi) \tag{61}$$

Comparing Eqs. (58) and (61), and recalling $\tilde{\varepsilon}^f_{\max}(t)=\varepsilon^f_{\max}(\xi=\alpha_0,t)$, we can write

$$\frac{\tilde{\varepsilon}^f_{\max}(t)}{\phi\left[\tilde{\varepsilon}^f_{\max}(t)\right]}=\frac{1}{E_r}\cdot\frac{1-\eta(\alpha_0,t)}{\eta(\alpha_0,t)} \tag{62}$$

Defining $\tilde{\eta}(t)=\eta(\alpha_0,t)$, we have

$$\frac{\tilde{\varepsilon}^f_{\max}(t)}{\phi\left[\tilde{\varepsilon}^f_{\max}(t)\right]}=\frac{1}{E_r}\cdot\frac{1-\tilde{\eta}(t)}{\tilde{\eta}(t)} \tag{63}$$

That is

$$\tilde{\eta}(t)=\frac{\phi\left[\tilde{\varepsilon}^f_{\max}(t)\right]}{E_r\tilde{\varepsilon}^f_{\max}(t)+\phi\left[\tilde{\varepsilon}^f_{\max}(t)\right]} \tag{64}$$

This is also equivalent to the damage viable defined in Bažant and Planas (1998).

VITA

Jinquan Zhong received his Bachelor of Engineering degree in engineering mechanics from Tongji University, Shanghai, China in 1996. He then worked for the Nanning Pinzheng Construction Consulting Co., Ltd, Nanning, China before he entered graduate study in the field of bridge engineering at Tongji University. He received a degree of Master of Science in bridge and tunnel engineering in June 2002. He was enrolled as a graduate student in the Department of Civil and Environmental Engineering at the University of Delaware, Newark, DE. He received a degree of Master in Civil Engineering in May 2005. His Ph.D. study started in August 2005 at Texas A&M University. His research interests include probabilistic and stochastic methods in civil engineering, structural reliability, reliability and performance-based design, earthquake engineering, engineering seismology, seismic hazard and risk assessment, structural deterioration, and loss estimation.

Mr. Zhong might be reached at email: jinquan.zhong@gmail.com. His permanent address is: Mapo Central Hospital, Lu-Chuan, Guang-xi, 537712, China.